The Dissertation Committee for Christian Wayne Green
certifies that this is the approved version of the following dissertation:

HYDRAULIC CHARACTERIZATION OF STRUCTURED PACKING VIA X-RAY COMPUTED TOMOGRAPHY

Committee:

R. Bruce Eldridge, Co-Supervisor

David T. Allen, Co-Supervisor

Roger T. Bonnecaze

Richard A. Ketcham

Gary T. Rochelle

HYDRAULIC CHARACTERIZATION OF STRUCTURED PACKING VIA X-RAY COMPUTED TOMOGRAPHY

by

Christian Wayne Green, B.S.

Dissertation

Presented to the Faculty of the Graduate School of

The University of Texas at Austin

in Partial Fulfillment

of the Requirements

for the Degree of

Doctor of Philosophy

The University of Texas at Austin

May 2006

For my father.

Save us a tee time, Dad.

ACKNOWLEDGEMENTS

First and foremost, I would like to thank my research advisor, Dr. Bruce Eldridge. Without his support and guidance during my tenure as a graduate student, this work would not have been possible. He always encouraged me to keep the big picture in mind and provided countless tidbits of knowledge and advice, both serious and not so serious. He has truly been a mentor to me in every sense of the word, and for that I am extremely grateful.

I also express my gratitude to the members of my dissertation committee. The challenges posed by Dr. David Allen, Dr. Roger Bonnecaze, and Dr. Gary Rochelle pushed me to explore the limits of experiment and theory. Furthermore, my understanding of X-ray computed tomography and image processing would not be what it is without the benefit of many technical discussions with Dr. Rich Ketcham.

As with any project, the success of my research depended on several people behind the scenes. Members of the Separations Research Program technical staff including Steve Briggs, Robert Montgomery, and Steve Orwick assisted with equipment selection, design, and assembly. Frank Seibert and Chris Lewis were responsible for executing the SRP pilot plant studies. The imaging experiments would not have been possible without the support of the technical staffs at both 3DID and General Electric. Thanks go out to Rodney Warner, Chris McKim, Glenn Meyer, Ed Strickland, and Dee Summers at 3DID in Austin and to Ben Nightingale, John Janning, Dave Anson, Al Berger, and Dan Williams at GE in Cincinnati.

I was fortunate enough to work with a superior group of individuals from the chemical processing industry as part of my project's advisory team. John Farone

contributed significantly to my education in distillation operations, and his interest in the project even after retirement provided much-needed encouragement during the last few months. In addition to supplying a variety of technical knowledge, Mitch Loescher was able to enlighten me about being a young engineer in the real world. I also found the imaging experiments to be much easier when John and Mitch came along to assist. I also appreciate the assistance of Mark Pilling and Randy Hardy, who taught me all I ever care to know (and more) about structured packing. Funding provided by the U.S. Department of Energy, the UT College of Engineering, and the Separations Research Program was greatly appreciated.

I benefited from the hard work and dedication of two spectacular researchers who assisted me, Marcus Lechner and Julie Briley. Marcus' work ethic led to an excellent-performing experimental setup, and Julie's ability to quickly comprehend code writing for image processing significantly improved data analysis. This dissertation would not have come together without many discussions with graduate student colleagues Travis Reine and Scott Stanley. Even after moving on to bigger and better things, the insight and collaboration provided by Carolyn Schmit at the beginning of the project was invaluable.

Finally, I cannot thank my family members enough for their steadfast love and unwavering support. Dad, although you're not here with us anymore, I hope that I continue to make you proud. Every day I feel that I become even more like you. Mom and Jonathan, you have always been there for me, and I only hope I can be as good a son and brother to you as you both have been to me. Thanks are also due to my grandparents for shaping the person I have become. Nicole, I cannot begin to express what it has meant to have you in my life this past year, so I will simply say thank you for everything you have done. Your love and encouragement helped make this possible.

HYDRAULIC CHARACTERIZATION OF STRUCTURED PACKING VIA X-RAY COMPUTED TOMOGRAPHY

Publication No._____

Christian Wayne Green, Ph.D.

The University of Texas at Austin, 2006

Supervisors: R. Bruce Eldridge, David T. Allen

Unit operations such as distillation, absorption, and stripping rely on the contacting of vapor and liquid phases to achieve a desired chemical separation. Existing models used to predict the performance of packed columns are primarily empirical. Such models were developed using measurements of column bulk properties, such as overall liquid holdup, pressure drop, and inlet and outlet stream compositions. Variations in column behavior on a local scale are not captured by existing models, and constitute an area in which model improvement has a potentially large impact. Development of improved models will require non-traditional data for validation. X-ray computed tomography (CT) has been evaluated as one possible technique for measuring local flow behavior in packed columns.

X-ray CT was used in this work to obtain images of an operating air-water contactor containing Mellapak 250Y stainless-steel structured packing. The image quality of two different X-ray scanner geometries, each with distinct temporal and spatial resolutions, was investigated. The void fraction and liquid holdup was calculated from

CT images for a variety of liquid and vapor flow rates below the flood point. In general, average liquid holdup calculated from CT images was within 10 to 15% of holdup measured using traditional techniques. The axial variation in liquid holdup, particularly near packing element joints, was explored. Holdup was shown to vary throughout the column, and was greatest near the joint of adjacent packing elements. The region 0.25 to 0.4 inches above the interface exhibited holdup two to five times higher than the holdup measured in the packing element bulk.

Three-dimensional images of the packed bed were acquired for static and dynamic conditions. The packing surface area, interfacial area between vapor and liquid, and the effective fractional area of a packed bed were calculated using three-dimensional reconstruction of two-dimensional CT images. Packing surface area was in good agreement with vendor-supplied values. Interfacial area measurements were compared with experimental data for vapor-liquid reactive area. Finally, both time variation of liquid flow and measurement noise during the course of data acquisition were quantified by analyzing the variation of X-ray transmission data.

TABLE OF CONTENTS

LIST OF TABLES

LIST OF FIGURES

NOMENCLATURE

Chapter 2

a, a_p	Packing specific surface area [m^{-1}]
a_e	Effective interfacial area [m^{-1}]
a_h	Specific hydraulic surface area of packing [m^{-1}]
a_t	Total surface area of packing [m^{-1}]
a_w	Wetted surface area of packing [m^{-1}]
c	Packing specific exponent
C_{pk}	Packing characteristic
d_p	Particle diameter [m]; $6(1-\varepsilon)/a$
d_p'	Particle diameter including surface liquid [m]
D_L	Diffusion coefficient, liquid phase [m^2/s]
D_v	Diffusion coefficient, vapor phase [m^2/s]
f_o	Friction factor for flow past a single particle
f_o'	Friction factor for flow past a single wetted particle
F_{SE}	Factor for surface enhancement
F_t	Correction factor for total holdup due to effective wetted area
Fr_L, Fr	Liquid Froude number; U_L^2/Sg
g	Gravitational constant; 9.81 m/s^2
g_c	Gravitational conversion factor
g_{eff}	Effective gravity [m/s^2]
h	Liquid holdup
h_o	Liquid holdup below the loading point
h_t	Total liquid holdup

H_{OG}	Height of an overall transfer unit, gas-phase basis [m]
$HETP$	Height equivalent to a theoretical plate [m]
K_2	Correlation constant
k_g	Mass-transfer coefficient, gas phase [m/s]
k_L	Mass-transfer coefficient, liquid phase [m/s]
L	Molar liquid flow [kmol/s]
M_L	Molecular weight of liquid [kg/kmol]
ΔP	Pressure drop [Pa]
ΔP_d	Pressure drop through a dry bed [Pa]
ΔP_{irr}	Pressure drop through an irrigated bed [Pa]
Re_L, Re	Liquid Reynolds number; $(U_L S \rho_L)/\mu_L$
S	Side dimension of corrugation [m]
U_g	Superficial gas velocity through a packed bed [m/s]
U_{gS}	Superficial gas velocity [m/s]
U_{LS}	Superficial liquid velocity
u_L	Liquid velocity with respect to the free column cross section [m/s]
u_v	Vapor velocity [m/s]
V	Molar vapor flow [kmol/s]
We_L, We	Liquid Weber number; $(U_L^2 \rho_L S)/(\sigma g_c)$
Z	Total height of packing [m]
ΔZ	Incremental height [m]

Greek Symbols

ε	Void fraction of packing
ε'	Void fraction of wetted packing
γ	Contact angle between solid and liquid film [degrees]

λ	Ratio of slopes, operating line to equilibrium line
μ	Viscosity ratio of μ_L:$\mu_{water@70^oF}$
μ_L	Liquid viscosity [kg/m-s]
η_L	Dynamic viscosity [kg-m/s]
π	3.14159…
ρ_g	Gas density [kg/m^3]
ρ_L	Liquid density [kg/m^3]
ρ_v	Vapor density [kg/m^3]
σ	Surface tension [dyne/cm]
σ_e	Packing surface energy [dyne/cm]
θ	Angle with horizontal for falling film or corrugation channel [degrees]

Chapter 3

a	Effective packing surface area [m^{-1}]
A_c	Column cross-sectional area in images [pixels]
C_{OH^-}	Concentration of hydroxide ion in solution [kmol/m^3]
D_{CO_2}	Diffusivity of carbon dioxide in solution [m^2/s]
dI	Differential intensity
dt	Differential in the direction perpendicular to X-ray beams in parallel-beam geometry
dL	Differential length
dw	Differential in the w-direction
dx	Differential in the x-direction
dy	Differential in the y-direction

dz	Differential length along the X-ray beam path
e	2.71828…
$f(x,y)$	Generic function of x and y to be determined by image reconstruction
$F(u,v)$	Fourier transform of $f(x,y)$
$F(w,\theta)$	Fourier transform of $f(x,y)$ represented in polar coordinates
H	Henry's law coefficient
h	Liquid holdup determined by traditional experiment
h_L	Local liquid holdup determined by X-ray CT image analysis
i	Index for pixel counting
I	Intensity of the X-ray beam
I_f	Final intensity of the X-ray beam after passing through object
I_o	Initial intensity of the X-ray beam
j	Imaginary number; $\sqrt{-1}$
K_{OG}	Overall mass-transfer coefficient, gas-phase basis [m/s]
k_g	Gas-side mass-transfer coefficient [m/s]
k_r	Reaction rate constant for CO_2 absorption [L/(gmol-s)]
L	Path length
N	Total number of pixels in an X-ray CT image
$P_\theta(t)$	Set of X-ray transmission data for parallel-beam geometry
P_i	Grayscale of pixel being considered in an X-ray CT image
P_w	Characteristic grayscale of a pixel filled with water
$Q_\theta(t)$	Filtered X-ray projection data
$R_\beta(\gamma)$	Set of X-ray transmission data for fan-beam geometry
$S_\theta(w)$	Fourier transform of parallel-beam projection data

t	Perpendicular distance of the ray from the origin for parallel-beam geometry
u	Cartesian coordinate in the frequency domain
v	Cartesian coordinate in the frequency domain
V_W	Volume of water that drains from a packed bed [m^3]
V_D	Holdup volume of the liquid distributor [m^3]
V_{PB}	Total volume of the packed bed [m^3]
w	Polar coordinate in the frequency domain representing the distance from the origin to the point of interest
x	Coordinate in the object space
y	Coordinate in the object space
z	Position along the X-ray beam path
	Greek Symbols
β	Angle that the central X-ray of a fan beam makes with the axes of the object space
γ	Angle between the ray path and the central ray path for fan-beam geometry
θ	Angle the X-rays make with the axes of the object space for parallel-beam geometry; polar coordinate in the frequency domain
$d\theta$	Differential angle
π	3.14159…
μ	Linear attenuation coefficient
$\mu(z)$	Function of linear attenuation coefficient along the X-ray beam path

Appendix A

a	Effective packing surface area [m^{-1}]
C_i	Concentration of species *i* [gmol/L]
C_{OH^-}	Concentration of hydroxide ion, corrected for reaction [gmol/L]
D_w	Diffusivity of carbon dioxide in water [m^2/s]
D_{CO_2}	Diffusivity of carbon dioxide in solution [m^2/s]
H	Henry's law coefficient [$kmol/m^3$-bar]
H_w	Henry's law coefficient for water [$kmol/m^3$-bar]
h_i	Contribution of species *i* to Henry's law coefficient [$m^3/kmol$]
HTU_{OG}	Height of a transfer unit, gas-phase basis [m]
I	Ionic strength of solution [$kmol/m^3$]
I_i	Contribution of species *i* to ionic strength [$kmol/m^3$]
K_{OG}	Overall mass-transfer coefficient, gas-phase basis [m/s]
k_{OH^-}	Rate constant for reaction of carbon dioxide with hydroxide ion in aqueous solution [L/(gmol-s)]
$k^{\infty}_{OH^-}$	Rate constant for reaction of carbon dioxide with hydroxide ion in aqueous solution at infinite dilution [L/(gmol-s)]
NTU_{OG}	Number of transfer units, gas-phase basis
T	Absolute temperature [K]
U_S	Superficial vapor velocity [m/s]
$Y_{CO_2,in}$	Ambient carbon dioxide concentration, inlet stream [ppm]
$Y_{CO_2,out}$	Carbon dioxide concentration, outlet stream [ppm]
Z_p	Height of packed bed [m]
z_i	Number of positive or negative charges on ion *I*

Greek Symbols

μ_{H_2O} Viscosity of water [mPa-s]

μ_{OH^-} Viscosity of solution [mPa-s]

CHAPTER 1: INTRODUCTION

1.1 Overview of Vapor-Liquid Contacting

Unit operations in the chemical processing industry predominantly consist of vapor-liquid contacting applications. Although classified by some as mature technologies, traditional operations such as distillation continue to attract attention from researchers who seek to improve on basic designs that have existed for decades. With the implementation of advanced column internals, including high capacity structured packings, becoming more widespread, the need for improved methodologies for column design also becomes an issue.

One area of packed column research that receives a great deal of consideration is predictive model development. Existing models for the prediction of packed column performance are typically semi-empirical. Amounting to large data fits, the models do not take into account the underlying momentum, heat, and mass transfer processes that govern the behavior and performance of these devices. A more detailed understanding of these phenomena is imperative before models can become truly predictive. As computing technology becomes more affordable the technical capabilities available for modeling on small scales will also improve. However, just as existing models were validated with experimental data, new models, such as those developed with computational fluid dynamics (CFD) simulations, will necessitate validation experiments.

The type of data traditionally used for validation represents the column bulk performance. Parameters such as overall pressure drop, feed and product compositions, and average liquid holdup suffer from the same shortcomings as traditional models; they do not represent the local behavior within the column. Advanced modeling of packed

columns presents a need for experimental validation data that can capture local scale behavior within the device.

One technique that has shown promise and gained acceptance as a validation tool is process tomography. By allowing non-invasive and non-intrusive evaluation of a test system, tomographic imaging techniques can provide qualitative and quantitative results that can be used to benchmark newly developed models or define boundary conditions for simulations. Process tomography is also viewed as an enabling technology that will contribute to further development of equipment associated with distillation applications, such as advanced structured packing design as suggested by Spiegel and Meier [69].

In summary, a fundamental understanding of the behavior of the vapor-liquid contacting process is critical for determining the degree of separation that may be achieved in an absorber, stripper, or distillation unit. The ability to accurately predict the performance of these devices has implications in both the design of future equipment and improvement of existing equipment operation. The purpose of this study is to investigate the vapor-liquid contacting phenomenon on a local scale and gain insight into the flow patterns observed in an operating contactor using X-ray computed tomography (CT). This information, when combined with advanced modeling efforts, has the potential to radically alter the design and operation of separations equipment.

1.1.1 Vapor-Liquid Contacting

Several common unit operations employed in the chemical processing industry rely on the contacting of vapor and liquid streams and the associated mass transfer between the two phases to separate a mixed feed stream into two or more enriched product streams. These operations include absorption, stripping, and distillation, with the

latter being the most common. Approximately 40,000 distillation columns are in operation in the United States alone [23].

Absorption processes involve selective mass transfer from the gas phase to the liquid phase. The process is a popular choice to remove contaminants, pollutants, or impurities from a gas stream. Stripping is the complimentary process where material is transferred from the liquid phase to the gas phase.

In a traditional distillation system as shown in Figure 1-1, a multi-component feed is separated into two or more product streams due to differences in the boiling point of each component. Energy input comes from a reboiler, which generates vapor that flows up through the column. A condenser is located at the top of the column to reform the liquid phase and send it back down through the column.

Distillation operations are highly energy-intensive and typically possess a low thermal efficiency, thus they require large inputs of energy to achieve the desired separation. The majority of this energy is supplied to the reboiler. Studies have shown that approximately 40% of the overall energy used by the chemical processing industry is related to distillation units [41]. With the large number of columns operating in the United States, it is estimated that distillation accounts for almost 2% of the nation's energy usage [2]. The ability to accurately design and model vapor-liquid contactors will significantly impact current patterns of energy use in the chemical processing industry. Even small improvements in design and operations practices that save energy or capital expenditure can have a large global impact.

The hydraulic behavior and associated flow patterns within an operating contactor are critical to the performance of the device. The primary limitation on hydraulic capacity is a phenomenon known as flooding. Flooding occurs when a large accumulation of liquid forms in the contactor. The column pressure drop increases

dramatically, operation becomes unstable, and performance is reduced. Factors that affect the point at which a column floods include the internal type, liquid and vapor flow rates, and the column design. Mass transfer efficiency is reduced as the vapor-liquid contacting pattern deviates from a more-ideal state. The "flood point" of a column is a flow rate at which mass transfer efficiency decreases dramatically. Ideally, the column should be operated on the verge of the flood point to maximize efficiency and capacity. However, due to poor understanding of how a column behaves, actual operating flow rates are typically lower. This conservatism aids in avoiding flood conditions that upset the performance of the device, yet it limits capacity and mass-transfer and energy efficiency.

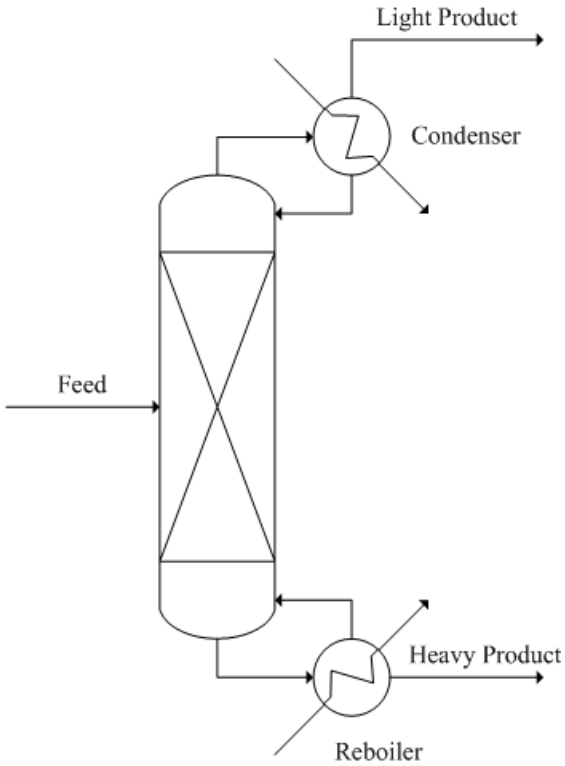

Figure 1-1. Typical process flow diagram for distillation service.

Another phenomenon that reduces the performance of packed columns is poor liquid distribution. This can occur as a result of poor initial distribution, in which case modifications to the liquid distributor will typically alleviate the problems. However, if distribution within the packed bed itself is poor, there are fewer options for improving the contacting pattern. Installation of devices that collect and redistribute the liquid between packed sections is possible, but at the price of increased capital and installation costs. An improved understanding of the liquid distribution within a packed section will aid in understanding the cause of poor flow patterns. Additionally, new column packings that take advantage of this knowledge to improve distribution will help reduce the overall costs associated with packed columns.

Measurement of the process conditions necessary to fully understand phenomena such as flooding and maldistribution has been limited to single locations, providing only a bulk, column-average value for critical parameters such as liquid holdup. The ability to non-intrusively gather information throughout a packed column operating at a variety of conditions has the potential to quickly advance the understanding of the physical processes that underlie the contact of vapor and liquid. Process tomography is one such technique.

1.1.2 Contactor Internals

Vapor-liquid contactors can typically be divided into two categories based on the type of internal used to enhance mass transfer between the liquid and vapor phases. Trayed columns consist of a series of metal plates, or trays, spaced throughout the height of the column. In contrast, packed columns contain one or more sections of packing material over whose surface liquid flows downward by gravity. The liquid flows either as films on the surface of the packing or as droplets and rivulets in the void spaces.

Packings may be of the random or structured variety. Random packings are geometrically shaped objects constructed of metal, ceramic, or plastic that are dumped into the column. Some examples of random packing are shown in Figure 1-2. Structured packings, as the name implies, are more organized materials that consist of corrugated sheets of metal, plastic, ceramic, or wire gauze bound together into bundles sometimes referred to as elements. The sheets may be perforated to equalize pressures across the column, as well as embossed with a surface treatment, which aids in the wetting and spreading of liquid across the sheets. A thin film of liquid that flows down the surfaces of the packing sheets is ideal for optimal mass transfer. The elements usually contain a wiper band, which is bent to provide a seal between the element and the column wall. The band serves to direct any liquid flow down the wall of the column back into the packing and also prevents vapor channeling around the element.

Figure 1-2. Examples of random packing. From left, 2” plastic Pall ring, 1” metal Pall ring, 2” metal Pall ring, metal #2P Cascade Mini-Ring (CMR) and plastic #3A CMR.

Structured packing is currently the state-of-the-art column internal. Although significantly more expensive on a per-volume basis than random packings, structured packings typically exhibit much lower pressure drop along with superior efficiency and capacity. Metal structured packings in particular have become popular due for their excellent structural integrity, good wettability, and the variety of corrosion-resistant materials available. Modifications to basic structured packing designs have addressed issues ranging from increased capacity to simultaneous catalyzed chemical reaction and separation. Figure 1-3 shows a structured packing element.

Figure 1-3. Mellapak 500Y structured packing with element height of 8” and diameter of 6”.

1.1.3 Current Modeling and Design Methodologies for Packed Columns

Predictive models for column performance have traditionally relied on semi-empirical approaches. This method involves fitting the model to performance data obtained on the column scale. However, this process does not capture the details of critical variations within the column. The models are also limited in application, as they do not extrapolate very well outside the range of flow characteristics and system physical properties on which they were correlated.

The traditional procedure has been to first represent mass transfer behavior, and then to apply a correction to the hydraulic modeling which forces the model to fit experimental data. One example of this approach is the Rocha-Bravo-Fair model [49, 50] developed for structured packing. Models for random packing usually require a statistical component to account for the variability in packing orientation when installed in the column.

In the Rocha-Bravo-Fair model hydraulic and mass-transfer behavior are treated separately. However, the development of the mass-transfer portion of the model relies heavily on the hydraulic model. Based on the geometry of the packing, a force balance is performed to determine the effective gravity acting on the liquid. Film flow is assumed over the entire surface of the packing in order to calculate the liquid holdup, which is correlated using existing experimental data. The interfacial area between the vapor and liquid phases is then calculated using another empirical expression. This provides a link to mass-transfer efficiency.

Using empirical correlations developed with wetted-wall column mass-transfer data, an expression for the gas phase mass-transfer coefficient was obtained. The liquid phase coefficient is calculated from penetration theory. Using the expression for interfacial area and the mass-transfer coefficients, the overall efficiency in terms of

height equivalent to a theoretical plate (HETP) can be calculated. A correction is applied to the liquid holdup to match the expected mass transfer performance. Thus, the interfacial area term is also affected, as area and holdup are related.

Figure 1-4 shows the Rocha-Bravo-Fair model along with two additional models considered to be the current state-of-the-art predictions for packed column performance. Shown is the prediction of fractional wetted area as a function of liquid rate, along with two sets of experimental data collected by Seibert et al. [64]. While the models follow the general trends observed in the experimental data, none of the models have a slope that matches the experimental behavior. Purely empirical modeling techniques such as neural networks have been shown to predict performance as well as the semi-empirical models. Towers designed using existing models are typically oversized for a given application to ensure proper operation. A more accurate approach based on a detailed understanding of the hydraulic behavior will allow columns to be designed more accurately and operated more efficiently, thus providing savings in both capital investment and operating costs.

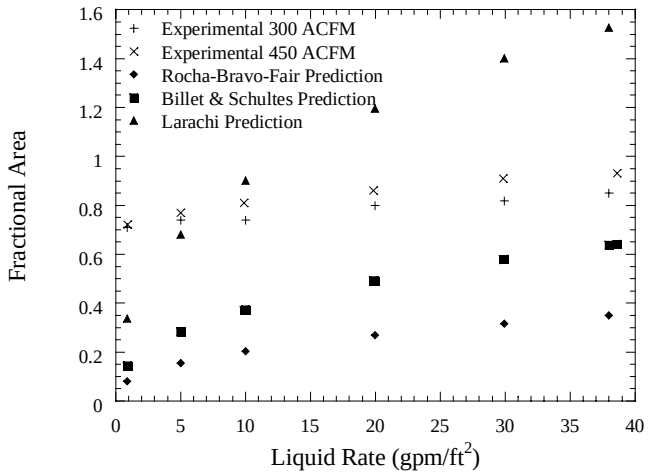

Figure 1-4. Comparison of predictive models with experimental data for fractional area in Montz B1-250 structured packing [9].

1.1.3 Steps to Improve Models

In order to accurately predict the performance of an operating packed column, it is necessary to gain a detailed understanding of the physical processes that drive the system. Advanced computational techniques have become widely used in recent years. With advances in computing power, simulations that were not possible have become feasible. By defining the basic transport equations that govern behavior of the two phases for a specific geometry, a first-principles approach can be applied to model column performance. The column is divided into small cells and the transport equations are applied to each cell. The solution procedure then iterates to find a solution for the cells, including matching the solution at the boundaries of adjacent cells. Convergence is achieved when a continuous solution has been found that fits all of the cells. Computational fluid dynamics (CFD) not only provides the ability to model hydraulic behavior, but also to make quick changes to a system once a robust model has been developed. For example, advanced computational approaches allow new designs for column internals to be produced at reduced cost. Ideas can be quickly tested on a simulation without the need for costly prototyping and pilot-scale studies.

Simulations and advanced models are only as good as the data used to validate them. While the traditional approach has developed a large bank of data for column-bulk properties, the new approach to modeling will require much more detailed information. Experimental data on a local scale will be needed to fully evaluate the capabilities of a given model. New techniques must be developed to explore the behavior of vapor-liquid contactors beyond the overall pressure drop or average holdup. These techniques will focus on parameters such as wetted area and local holdup variations. The application of X-ray computed tomography to an operating packed column is one example of such a technique.

1.2 Process Tomography

The term process tomography is applied to a range of techniques that permit the measurement of various properties inside a vessel. It is an extension of non-destructive testing (NDT), where objects can be imaged in a non-invasive, non-intrusive manner. Tomographic techniques measure the distribution of a given property throughout the area of interest, in either two-dimensional "slices", or three-dimensional volumes. Many of the same techniques used for medical imaging may also be applied to industrial applications. Transmission tomography (either X-ray or gamma-ray), magnetic resonance imaging (MRI), electrical capacitance, resistance, or inductance tomography, and ultrasonic tomography are all examples of experimental methods used for process tomography. As an extension of the work of Cartmel and Schmit, the method used for this study is X-ray computed tomography (CT) [10, 55, 56, 58, 59].

As with other tomography systems, X-ray CT utilizes a set of detectors paired with a computer to obtain an image of the object of interest. With X-ray CT, an X-ray source directs a beam of X-rays at the object. As the X-rays pass through the object, they are attenuated. The detectors measure the intensity of the beams after they have passed through the object. Based on the geometric positioning of the object and the difference in intensity between the initial beam and the attenuated value measured for a large number of projections, a map of the object's density is created. A given material will have a distinct linear attenuation coefficient, which is defined by the mass density of the material multiplied by the mass attenuation coefficient. The reconstructed images are a pictorial distribution of the object's linear attenuation coefficient.

In fan-beam X-ray CT, the X-rays pass through a thin slice of the object. The resultant image represents a cross section of the object at the location in which the slice of X-rays passes through the object. By taking consecutive slices, the series of images

can be combined to represent the object in three dimensions. Alternately, cone-beam X-ray CT directs a conical beam of X-rays through the object and onto a flat panel detector. This method produces all the data necessary to recreate the object in three dimensions with just one scan. Individual slices of interest can then be extracted from the volumetric data set.

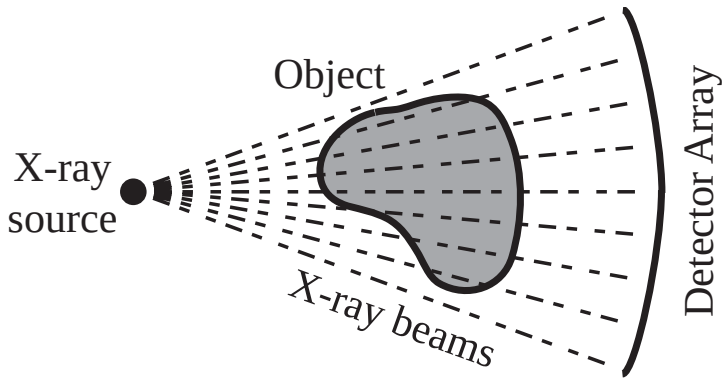

Figure 1-5. Overhead view of typical fan-beam X-ray CT setup.

The high spatial resolution, well understood physics, and overall compatibility with a vapor-liquid contacting device made X-ray CT the most desirable imaging technology for use in this study. Electrical capacitance, resistance, and inductance tomography do not possess the spatial resolution required to discern the properties of interest inside the packed bed. The metal content of the structured and random packings used in this study prevented the use of MRI. Gamma-ray devices have been used to image industrial distillation columns for more than 40 years. However, X-ray CT possesses a superior spatial resolution to that of gamma ray scanning, and does not require the amount of special training necessary when a nuclear-decay gamma-ray source

is used. Although the temporal resolution of X-ray CT is limited, this technique represents the best overall method to image a vapor-liquid contacting system [55].

1.3 Project Scope

The focus of this work is to extend the knowledge of the physical phenomena associated with vapor and liquid flow in packed columns such as those observed in distillation, absorption, and stripping services. The ability of novel technologies and advanced computational techniques to provide insight regarding small-scale local behavior is being investigated. Specifically, X-ray CT is used to investigate the hydraulic parameters necessary for a greater understanding of column behavior. Past work in this area using transmission tomography techniques, as discussed in Chapter 2, has not been able to measure all of the variables required to model column performance.

The objectives at the start of this work involved using X-ray CT to gain insight into flow patterns observed in a packed column as well as obtaining quantitative measurements of hydraulic parameters. The X-ray CT work was also provided experimental validation for computational fluid dynamics (CFD) simulations of vapor-liquid flow in a column containing structured packing. Pairing the two analysis methods together will allow a more rigorous, first-principles model for the prediction of a column's hydraulic performance. It will also provide additional data for incorporation into future semi-empirical models that will apply over a wider range of physical properties and operating conditions. Achieving these goals involves:

1. Evaluating the hydraulic performance of a vapor-liquid contactor, including
    - Calculating packed bed void fraction from X-ray CT images

- Observing flow patterns at relevant flow conditions
- Measuring flow variation over time
- Calculating liquid holdup from X-ray CT images
- Determining wetted area from a series of X-ray CT images

2. Investigating different types of packing, such as
    - Structured packing
    - Structured packing with modifications intended to increase the hydraulic capacity
    - Random packing
    - Catalytic distillation packing
3. Improving X-ray CT image quality, namely by
    - Utilizing state-of-the-art technology
    - Reducing or eliminating image artifacts
    - Developing image processing techniques

CHAPTER 2: LITERATURE REVIEW

2.1 Packed Column Performance Models

The modeling of mass transfer devices containing random and structured packing has been an area of active research for a number of years, with the degree of complexity used in modeling increasing dramatically with recent improvements in technical computing technology. The majority of column models used today are semi-empirical, relying on data-fitting constants determined from experiments. The data acquired from such experiments are primarily output variables that represent the column as a black box, such as feed and product compositions and total pressure drop. These values do not capture the small-scale local behavior that has been shown to have a large effect on the overall performance of the device.

Aside from the semi-empirical models, there have been efforts to either simplify existing models by effectively reducing the number of parameters required, or to follow a more complex approach, such as with experiments using computational fluid dynamics. A modern data fitting approach that has also been used is the application of neural networks, where large banks of data are used to model a system. While each of these approaches has been used with varying degrees of success, there have been few, if any, attempts to rigorously model the underlying physical processes that occur during operation of packed columns, including behavior that appears on a local scale within the packed bed.

The driving force behind the modeling of column performance is two-fold. Models are used for the design of new columns, and also for accurate simulation of existing systems, which is of tremendous value from an operations standpoint. From the

perspective of design, modeling column behavior involves the areas of hydraulics and mass transfer. The hydraulic limitations of a column need to be understood in order to design the device with a proper diameter to accommodate the expected capacity. Parameters that affect the hydraulic performance include the geometry of the packing, flow rates, and physical properties of the fluids. The mass-transfer efficiency of the column will impact the height of bed required to achieve a desired separation. This is typically manifested in terms of the height equivalent to a theoretical plate (HETP) for packed columns. Factors of consideration for mass-transfer performance include mass-transfer coefficients, concentration gradients that serve as the driving force, as well as the effective interfacial area between the liquid and vapor phase. It is this last variable that links hydraulic and mass-transfer performance together, and it is greatly impacted by the design of the packing. Fully understanding the area available for mass-transfer will greatly impact the accuracy of predictive models, as well as foster the development of advanced column internals. A comprehensive overview of many types of mass-transfer correlations for packed columns was reported by Wang et al. [79], identifying the limitations of existing models and areas for potential refinement.

2.1.1 Semi-Empirical Models for Hydraulic Performance

Models used to predict the hydraulic behavior of packed columns can generally be classified to be particle models or channel models. Channel models describe the vapor as flowing upward through a number of channels, with the liquid flowing downward on the inside walls of the channels. As the liquid flow is increased, the area available for vapor flow is reduced, resulting in increased pressure drop. The model of Rocha et al. [49] for structured packing is one example of this theory. Stichlmair et al. [70] developed a model for random packing that was based on a particle approach, where the pressure drop

is attributed to the drag on a packing particle. Liquid adheres to the particle, increasing its characteristic dimension, drag, and thus, pressure drop. The presence of liquid also results in the void fraction of the bed being reduced.

The model of Stichlmair et al. [70] was developed primarily as a general prediction for the pressure drop and hydraulic capacity for randomly packed columns, although the model has been validated for some structured packings. The dry pressure drop of the packed bed is first calculated based on particle theory. The type of packing used in the column will impact the pressure drop. Equation 2-1 defines the dry pressure drop, with values used in calculating the friction factor for different packing types provided by Stichlmair.

[2-1] $$\frac{\Delta P}{Z} = \frac{3}{4} f_o \left(\frac{1-\varepsilon}{\varepsilon^{4.65}} \right) \frac{\rho_g U_g^2}{d_p}$$

When liquid flow is applied to the bed the pressure drop increases as a result of the increased liquid holdup. The presence of liquid effectively increases the characteristic size of the packing particles being considered. In addition, void space in the column is reduced. The friction factor for the wet particle becomes different than that of the dry particle due to the increased size. The expression for irrigated pressure drop is given by Equation 2-2.

[2-2] $$\frac{\Delta P_{irr}}{Z} = \frac{3}{4} f_o' \left(\frac{1-\varepsilon'}{\varepsilon'^{4.65}} \right) \frac{\rho_g U_g^2}{d_p'}$$

Using the empirical relation for liquid holdup given by Equation 2-3, the ratio of dry and irrigated pressure drop can be expressed using terms depending solely on the type of packing. The resultant expression is shown in Equation 2-4. When the column is operated below the loading point, the liquid holdup is independent of vapor rate. At and above the loading point, holdup depends on liquid density and pressure drop according to the Stichlmair model. However, the accuracy of this empirical relationship relies on an accurate determination of holdup below the loading point. Since the definition used for liquid holdup incorporates the irrigated pressure drop, Equation 2-4 is defined implicitly and thus requires iteration.

[2-3] $$h = h_o\left[1 + 20\left(\frac{\Delta P_{irr}}{Z\rho_L g}\right)^2\right]$$

[2-4] $$\frac{\Delta P_{irr}}{\Delta P} = \left(\frac{1-\varepsilon[1-(h/\varepsilon)]}{1-\varepsilon}\right)^{(2+c)/3}\left(\frac{1}{1-(h/\varepsilon)}\right)^{4.65}$$

Developed using a channel modeling approach, the Rocha-Bravo-Fair model [49] for hydraulic performance of corrugated sheet structured packing used a mechanistic approach to predict a column's pressure drop and flood point. The flood point is a measure of the maximum hydraulic capacity for a column and is characterized by a backup of liquid in the packed section. This disturbance in flow is highly non-ideal and severely decreases the mass-transfer efficiency of the device.

The model requires total liquid holdup to be initially determined. The total holdup consists of a static contribution and a dynamic contribution. The static holdup is the volume of liquid that remains in the packed bed after flows to the column cease.

Dynamic, or operating holdup, is the amount of liquid in the column during operation and is comprises the difference between static and total holdups. To simplify the model, static holdup was deemed negligible because the correlation given by Equation 2-5 fit the data well with or without the static term included. A force balance was applied to the liquid film assumed to be flowing on the packing surface to determine the effective gravity. Effective gravity was combined with drag on the liquid by vapor, vapor pressure drop, and liquid buoyancy to describe the forces in the channels. A correction factor, F_t, based on the correlation developed by Shi and Mersmann [68] is added to account for total holdup in terms of interfacial area available for mass transfer.

[2-5] $$h_t = \left(4\frac{F_t}{S}\right)^{2/3}\left(\frac{3\mu_L U_{LS}}{\rho_L(\sin\theta)\varepsilon g_{eff}}\right)^{1/3}$$

Once liquid holdup had been modeled, the column pressure drop was determined for both dry and irrigated conditions. The dry pressure drop is modeled using a friction factor approach. As expected, the dry pressure drop prediction is independent of the liquid. Using experimental data for an air-water system applied to several packings, an expression for irrigated pressure drop was correlated.

[2-6] $$\frac{\Delta P}{\Delta Z} = \frac{\Delta P_d}{\Delta Z}\left(\frac{1}{1-K_2 h_t}\right)^5$$

Shown in Equation 2-6, the irrigated pressure drop depends on the dry pressure drop and the total liquid holdup. Obtaining an expression for liquid holdup prior to modeling pressure drop ensures that the resulting irrigated pressure drop expression will

be applicable in the loading region. The correlation constant, K_2, depends linearly on packing size. Like the Stichlmair model, the pressure drop prediction of Rocha et al. is iterative.

The so-called Delft model presented by Olujic [42] shares the basis of the model of Rocha et al., suggesting that flow in structured packing can be explained using channel theory. However, the channels proposed by Olujic are triangular in shape. The Delft model also involves more explicitly defined macro-geometrical parameters that may impact structured packing performance. The pressure drop of the column does not have as great a dependence on drag at the vapor-liquid interface, as it is modeled to be more a result of the sharp bends in the flow channels. Perhaps the greatest difference in the two models from a hydraulic standpoint is that the Delft model assumes the packing to be completely wetted by liquid; this forces the liquid holdup to be solely based on the packing area and liquid film thickness. The two models were compared to each other and experimental data by Fair et al. [17].

2.1.2 Semi-Empirical Models for Mass-Transfer Performance

One method of describing the physics of mass transfer across the interface between vapor and liquid phases is penetration theory [16, 21]. This behavior is the result of a flow pattern that can be described as laminar flow along a surface where liquid mixing occurs after a certain contact time, or by small elements of liquid contacting the gas phase for a specified average period of time before being replaced by new liquid elements from the bulk. The theory is primarily applied to determine liquid-phase mass-transfer coefficients. The time-averaged coefficient is inversely proportional to the square root of the average contact time and directly proportional to the square root of the liquid diffusion coefficient.

A second theory used to describe mass transfer between vapor and liquid is the two-resistance theory [21, 63]. This theory assumes the liquid and vapor phases to be in equilibrium at the interface. The bulk concentrations are also assumed to be constant, meaning that the concentration gradient between the bulk and interface occur in a thin film on either side of the interface. This approach is represented graphically in Figure 2-1. The flux through each phase must be constant for the mass-transfer process to be viewed as steady state. Various concentration-profile driving forces may be used to define the mass transfer as long as the corresponding mass transfer coefficients are used. This allows the calculations to be simplified for systems where determining specific mass transfer coefficients would otherwise prove difficult.

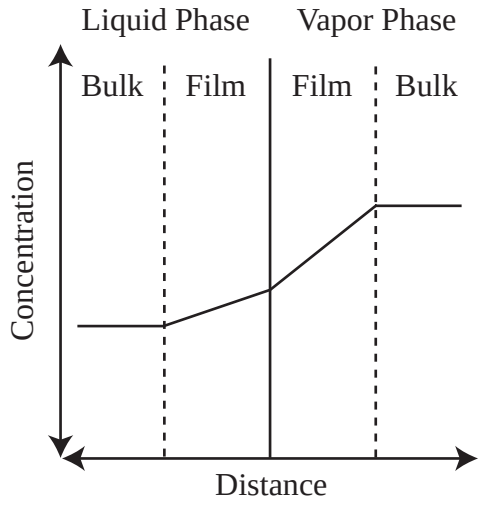

Figure 2-1. Interfacial concentration profile predicted by two-resistance theory.

The second portion of Rocha et al.'s [50] comprehensive model for packed column performance utilized two-resistance theory to predict mass transfer characteristics for structured packing. The primary inputs to the model are mass-transfer coefficients for

both phases and the effective interfacial area. Penetration theory was used to obtain an expression for the liquid phase mass-transfer coefficient. The exposure time used was based on liquid flow across one packing sheet. The gas phase mass-transfer coefficient was correlated from prior studies using a wetted wall column. The expression uses the dimensionless Sherwood, Reynolds, and Schmidt numbers combined with parameters describing the packing geometry. Using the semi-empirical expression developed by Shi and Mersmann [68], Equation 2-7 was formulated to predict the effective interfacial area for structured packing, including a correction factor F_{SE} to account for various surface treatments. A separate correlation was used for determining the interfacial area for wire gauze packings. Equation 2-8 shows the combination of mass-transfer coefficients and effective area into a calculation for HETP.

[2-7] $$\frac{a_e}{a_p} = F_{SE}\frac{29.12(We_L Fr_L)^{0.15} S^{0.359}}{\mathrm{Re}_L^{0.2}\,\varepsilon^{0.6}(1-0.93\cos\gamma)(\sin\theta)^{0.3}}$$

[2-8] $$HETP = H_{OG}\frac{\ln\lambda}{\lambda-1} = \left(\frac{U_{gS}}{k_g a_e} + \lambda\frac{U_{LS}}{k_L a_e}\right)\frac{\ln\lambda}{\lambda-1}$$

A model for mass-transfer coefficients, both liquid and gas phase, in columns with random packing was developed by Onda et al. [44]. The basis of the calculations for mass-transfer coefficients was a semi-empirical equation describing the wetted surface area, shown in Equation 2-9. The equation includes parameters for liquid surface tension and packing surface activity in addition to flow rates. No packing-specific parameters were required. The analysis also assumes that the wetted packing area is equivalent to the effective area available for mass transfer. This assumption breaks down when the

interface becomes unstable at higher gas rates in the loading and flooding regimes or when a more turbulent flow pattern dominates, as for rivulet flow or when droplets are formed. The model was applied to distillation and showed that the mass-transfer resistance in both phases should be taken into account. An expression for packing height in distillation service was provided based on the gas and liquid phase mass-transfer coefficients and wetted area.

[2-9] $$\frac{a_w}{a_t} = 1 - \exp\left[\frac{-1.45\left(\frac{\sigma_e}{\sigma}\right)^{0.75} \mathrm{Re}^{0.1} We^{0.2}}{Fr^{0.05}}\right]$$

Wagner et al. [78] developed a mass transfer model for columns containing random packing. The model of Stichlmair et al. [70] was used to predict hydraulic behavior. Penetration theory was used to define liquid and vapor phase mass-transfer coefficients. The hydraulic model was used to describe the area available for mass transfer in terms of packing area, void fraction, and liquid holdup. A correction factor is included to account for area viewed as ineffective for mass transfer. The prediction of HETP involves a parameter dependent on packing type to determine the characteristic contact length for the two phases. Additionally, evaluating HETP requires flow rates and fluid properties. Equation 2-10 is the final expression for predicting HETP via the Wagner model.

[2-10] $$HETP = \frac{C_{pk}\frac{Z^{0.5}}{a_p}\left(\frac{\pi(\varepsilon - h)u_v}{4D_v}\right)^{0.5}\left[1+\left(\frac{hD_vM_L\rho_v}{(\varepsilon-h)D_LM_v\rho_L}\frac{V}{L}\right)^{0.5}\right]}{\left(\frac{1-\varepsilon+h}{1-\varepsilon}\right)^{2/3}-1}$$

A model for predicting the mass-transfer performance of packed columns was proposed by Billet and Schultes [7]. The authors used a channel modeling approach to define the mass-transfer efficiency in terms of the height and number of liquid-phase and gas-phase transfer units (HTU and NTU). These parameters are viewed as more physically sound than HETP, as they describe a fundamental detailed mechanism to model the mass transfer rate between phases. Packing-specific shape constants were used to express the deviation of real flow from ideal vertical channel flow. Mass-transfer coefficients were also calculated for both phases. The column pressure drop and load limits (flood point) were determined using a general definition for column holdup. Finally, the true column holdup given by Equation 2-11 was calculated as a function of the packing hydraulic surface area, which depends on the Reynolds number. The model was validated using a database that included data for more than 50 test systems and over 70 packing types.

[2-11] $$h_L = \left(12\frac{1}{g}\frac{\eta_L}{\rho_L}u_L a^2\right)^{1/3}\left(\frac{a_h}{a}\right)^{2/3}$$

The semi-empirical mass-transfer correlations that have been presented rely heavily on the ability to predict the hydraulic behavior of the column. Column holdup has been used to predict mass transfer area, yet liquid holdup in many cases has been correlated with experimental data rather than truly modeled. More accurate methods for

determining effective area are necessary for mass-transfer modeling to be improved. The use of non-invasive imaging such as X-ray computed tomography is viewed as one method of accomplishing this task.

2.1.3 Simplified Modeling Approaches

Locket [36] predicted HETP for structured packing via a shortcut method. His model was based on the model of Rocha et al. [50], which he believed to be the most accurate of the existing correlations for predicting mass-transfer behavior in columns containing structured packing. When plotting HETP versus gas flow rate (F-factor), Lockett observed that the data points at 80% of flood to be linear. Equation 2-12 represents the shortcut route to HETP, and it depends only on system physical properties and the packing surface area. Despite being limited to columns of small diameter with short bed lengths, good liquid distribution, and radial mixing, the technique is much simpler than using the full semi-empirical model.

2-12
$$HETP = \frac{1.54 g^{0.5} (\rho_L - \rho_g)^{0.5} \mu^{-0.06}}{a\left[1 + 0.78 \exp(0.00058a)\left(\frac{\rho_g}{\rho_L}\right)^{0.25}\right]^2}$$

A neural network to predict HETP and pressure drop for structured packing was developed by Whaley et al. [81]. The same fifteen inputs used in the models of Rocha et al. [49, 50] were incorporated into a multi-layer perceptron (MLP) model. A data set containing pressure drop and HETP for four different structured packings and four operating pressures was used, resulting in 240 total values. The purely empirical MLP model was more accurate in predicting HETP than the semi-empirical approach of Rocha

et al. The MLP model was then simplified to reduce the number of parameters, eliminating those that did not significantly impact the determination of HETP. The variable with the greatest impact on HETP was determined to be the packing corrugation angle. A separate MLP model was used to predict pressure drop, with the results showing good agreement with the Rocha-Bravo-Fair prediction. While the HETP calculations of Rocha et al. depend on the pressure drop predicted from the hydraulic model, the neural network approach has no link between the MLP models for pressure drop and HETP.

The work of Whaley et al. was extended by Pollock and Eldridge [47] to include a total of nine types of structured packing. In modeling the HETP via a neural network with fifteen inputs taken from the Rocha-Bravo-Fair model [49, 50], a dependence on packing surface treatment was observed. The authors ranked the various input parameters in order of importance. The results of neural network modeling appeared superior to the prediction provided by the Rocha-Bravo-Fair model; however, as with all empirical approaches, the neural network model is only applicable to systems with properties similar to those in the data set used to train the model.

Djebbar and Narbaitz [15] used a neural network approach to model the overall liquid phase mass transfer coefficient in packed columns operated as air strippers. The database used in developing the model contained a variety of pilot-scale experimental data for different size columns, flow rates, chemical systems and packing types; approximately 1,250 data points were available. A total of eight dimensionless variables were used as inputs, with the Sherwood number based on overall mass-transfer coefficient being the output. The results showed a 40% improvement over the Onda model [44] predictions. The neural network model also captured the sharp increase in

overall liquid phase mass-transfer coefficient at high gas rates. However, the effect of packing size was not captured.

2.1.4 Advanced Modeling Approaches

With recent advances in computing technology, computational fluid dynamics (CFD) has emerged as a viable tool for conducting simulation experiments of complex systems, including multiphase flow in packed columns. One of the benefits of CFD is that it provides the ability to model behavior on a local scale and account for variations in flow throughout the column. Transport equations are solved for small finite elements and averaged to depict macro-scale performance. To ensure the phenomena predicted by simulations make physical sense, it is imperative to have supplemental experimental studies for validation, particularly on scales smaller than the column level. X-ray computed tomography is viewed as one such technique that can verify flow patterns predicted by CFD simulations or serve as a source for boundary conditions when developing a simulation.

Yin and coworkers [84] used CFD experiments to predict the mass-transfer performance of distillation columns containing random packing. To form a closed system of equations, empirical correlations for various physical behaviors associated with randomly packed columns were used, such as column pressure drop, interphase mass transfer, and void fraction distribution. For a column containing Pall rings, the CFD model was more accurate in predicting HETP than traditional models where the radial distribution of liquid and vapor are assumed to be uniform. The model also captured variation of HETP within the column, correctly predicting the slight increase in HETP observed at increasing bed depth due to the buildup of wall flow.

Several studies have been recently reported that focus on simulating liquid flow on textured and smooth inclined surfaces, such as those found in structured packing. Szulczewska et al. [72] studied liquid flow on Mellapak 250Y using a CFD model and an experimental technique. The aim of the simulation effort was to obtain liquid and gas interfacial area for countercurrent flow on structured packing. Air was used as the vapor phase, and both toluene and water were studied as the liquid phase. A flat plate geometry and a geometry based on Mellapak 250Y were used. Images of liquid film formation and surface coverage were produced both by simulation and experiment for both liquid materials. The toluene was observed to wet the surfaces better than the water in both techniques. The minimum flow rate to completely wet the surface could be determined from the CFD model, and was higher for the corrugated plate than the flat plate. An interesting result of the simulations was that the interfacial area increased until the entire surface was covered with liquid, and then was observed to further increase slightly due to the formation of waves in the liquid film.

The work of Ataki and Bart [4] focused on simplified laminar rivulet flow on an inclined metal plate. The simulations were verified using an optically assisted mechanical sensor to measure the thickness of rivulets for experimental flow cases that matched the simulated conditions. A multiphase flow model known as the volume of fluid (VOF) model was used. FLUENT, a commercial computational fluid dynamics software package, was selected for the experiments. The VOF model assumes that the fluids or phases are not interpenetrating and that the sum of the volume fractions in each control volume is equal to one. The actual location of the interface is tracked by solving a continuity equation for the volume fraction of any of the phases. The variables and properties in each cell are then weighted according to the volume fractions. Various mixtures of glycerin and water were used as the liquid phase. The simulation results for

rivulet shape compared favorably to two models from the literature and the experimental measurements. The rivulets flowed more slowly on a wavy plate than a flat one. No vapor flow was applied in the study.

The VOF model was also used within FLUENT in the work presented by Gu et al. [19]. A two-phase CFD model predicting the hydrodynamics of film flow on inclined corrugated plates was developed where the influence of surface microstructure, liquid properties, and gas flow rate was investigated. The development of film flow is unsteady, so time steps were incorporated into the solution until a constant liquid film height was obtained on the plates. The solution domain was initially filled with gas, and then liquid flow was introduced at the top of the plate at a constant velocity. A total of five different types of plates were studied, one flat and four with varying degrees of waviness. For the flat plate, liquid accumulated at the leading edge of the developing film, increasing until gravity acts to break the film. Additional liquid is supplied to the front of the film, eventually resulting in a steady film. For the wavy plates with small structure, the liquid film never becomes steady, but breaks up randomly, usually near the transition from crests to troughs on the surface. The liquid residence time on the wavy plates was also longer than that of the flat plate. However, for plates with larger waves, a steady liquid film will form. Unfortunately, the flow pattern for plates with large waves results in numerous eddy currents in the concave portion of the surface. These eddies contain stagnant liquid, which is highly non-ideal for heat- and mass-transfer processes. In light of the dependence of flow pattern on the surface microstructure, the opportunity to optimize the texture of packing surfaces has been presented.

Several different liquids were tested in the simulation by varying the physical properties. Increasing the liquid viscosity was shown to increase the film thickness yet have little effect on other film structures. Surface tension effects were investigated by

either activating or deactivating the surface tension term of the momentum equation in the simulation. When surface tension was considered, the films observed were slightly thicker but exhibited more small-scale variation, or rippling. An obvious phase shift between the solid surface and the free surface was apparent. With the impact that surface tension had on film behavior, it was suggested that applying surfactants or some type of physical or chemical surface treatment to packing could be explored.

Perhaps the most important observations by Gu et al. were for the simulations where a countercurrent gas flow was applied. At only 0.0001 s after airflow was applied to a film of acetone, the free surface of the liquid began to fluctuate, with film breakup occurring 0.0045 s after gas flow was applied. Materials that exhibited thicker films before the application of vapor flow were more difficult to break down, even at higher gas rates. The authors surmised that all effects to increase the liquid film thickness would be advantageous in maintaining a continuous film, reducing the possibility of dry patches that negatively impact column performance.

Crine and coworkers [13] prepared a stochastic model to describe the hydrodynamics of trickle flow columns. The model was separated into a micro-scale component and a macro-scale component. The micro-scale component represents a small volume element that has average geometrical properties that correspond to the whole packing. Constitutive relationships such as the Ergun equation apply at this level. The macro-scale properties can be expressed as a probability distribution that describes the seemingly random liquid flow paths and partial wetting of the packing. Correlations were developed for predicting the wetting efficiency, pressure drop, and dynamic liquid holdup. A minimum and maximum Reynolds number can be calculated from this type of model, with the minimum representing the minimum flow producing a stable liquid film on the packing, and the maximum value representing the local flood point where the only

phases present are liquid and packing. This approach combines fundamental physics along with statistics to provide new insight to the underlying mechanisms and complex properties of random packing that determine liquid flow distribution and hydrodynamics.

A hydrodynamic continuum model was developed by Iliuta et al. [24] for two-phase flow in columns containing structured packing. Based on the volume-average mass and momentum balance equations and the double-slit model approximation, the model predicts irrigated pressure drop and liquid holdup for operation in the pre-loading zone. The double-slit model approximates the packing void area as two geometrically identical inclined slits, one of which is dry (no countercurrent liquid flow), the other wet. The advanced portion of the model used three-dimensional single-phase gas flow CFD simulations to estimate the bed laminar and turbulent Ergun constants required as model input. The model was validated using a database that included a wide variety of experimental data relative to the irrigated pressure drop and liquid holdup for structured packing. Agreement with the experimental data was good.

The wide variety of applications for computational fluid dynamics introduces many new ways to approach existing problems in packed column design. The relative availability of supercomputing resources will continue to make CFD an attractive option when modeling column performance. However, further advances in the development of experimental techniques for simulation validation are necessary, particularly on a small scale.

2.1.5 Limitations on Modeling

The applicability of existing predictive models for column performance is determined primarily by the data on which the column was validated. The majority of these models used data that represents an average behavior of the column. Extending the

models to systems that are very different than those for which they were correlated becomes a highly unreliable venture. One example is the method typically used for experimentally measuring hydraulic parameters such as pressure drop and liquid holdup. Air and water are the most popular materials for measuring these variables. However, water has an extremely high surface tension compared to real-world systems, the majority of which are organic. The effect of surface tension on liquid contact angle and surface wetting has been shown to be of great importance in determining liquid holdup and interfacial area. These variables greatly impact the calculation of mass-transfer coefficients and HETP.

Semi-empirical models and CFD methods attempt to include a more fundamental basis of momentum, heat, and mass transfer, but the data necessary to validate these models are scarce, and still do not represent local variations in behavior. Although better at predicting location-dependent variations, CFD simulations still require correlations to describe transport behavior.

While showing promise in predicting packed column behavior, the neural network approach is, at best, a large data fit. The empirical methodology does not have a fundamental basis to describe the transport phenomena that is occurring. Larger data sets will reduce the potential of attributing certain behaviors to the wrong input variables. However, as with semi-empirical models, neural network models are only applicable to systems similar to the ones used for training. The relative simplicity of these models may allow them to be applied in very specific cases provided there is enough experimental data to train the model.

As mentioned previously, semi-empirical column performance models make the assumption of perfect radial and axial mixing, ignoring the variations in performance associated with maldistribution. Incorporating terms to describe the effects of liquid

distribution would increase the accuracy of these predictions. Poor column performance, exhibited by a reduction in capacity or separation efficiency, is often tied to poor distribution. While the overall effect of poor distribution is apparent on the column-scale, the behavior that initiates such phenomena is many times confined to a specific location in the column. The effects begin locally and eventually affect neighboring regions until the entire column is involved.

The X-ray computed tomography technique used in this study is one example of an experimental tool for investigating the effects of liquid distribution on column performance. It has the desired feature of being able to measure small-scale behavior as well as behavior variations within the column. Whether the visual evidence provided by the images is used to validate simulations or simply to gain a better visual understanding of what happens inside structured packing, the goal remains to reveal the underlying causes for poor performance. Fully understanding hydraulic behavior is the first step in successfully predicting mass transfer performance. X-ray CT has the potential to experimentally determine liquid holdup and wetted area, thus providing a basis for improved attempts at modeling the behavior of packed columns and greater understanding of how effective column internals are at improving flow patterns.

2.2 Process Tomography

The use of process tomography to non-invasively image fluid flow has been well documented within the past 10 years. Applications of many different imaging technologies exist, including electrical capacitance tomography (ECT), electrical resistance tomography (ERT), nuclear magnetic resonance imaging (NMRI), gamma-ray tomography, and X-ray tomography. While many of these methods were initially

developed for medical applications, they have been extended and enhanced for use in the non-destructive testing arena, including the imaging of process vessels. Selection of a specific technique is dependent upon the properties that are desired for extraction from the process. For example, transmission tomography, such as that with an X-ray or gamma ray source allows differentiation between materials of varying density, whereas ECT produces a map of permittivity.

For the purpose of the current work, X-ray computed tomography was chosen for its ability to balance spatial resolution with temporal resolution. The high energy of X-ray sources permits the scanning of dense materials such as metal structured packing, which would be difficult with a lower energy source. Most studies involving gamma ray and medical (<200 kV) X-ray sources have been limited to imaging plastic column internals. Spatial resolution for gamma-ray imaging systems is limited by gamma-ray detection technology. This prohibits the collection of data on the scale necessary for development of a more-rigorous, first-principles model of hydraulic behavior. Magnetic interference with metal objects inhibits the application of NMRI to the current study. X-ray CT scanning facilities are also more numerous and accessible than their NMRI counterparts.

A thorough review of previous work with various scanning technologies other than X-ray and gamma-ray CT was presented in the work of Cartmel [10] and Schmit [56], in addition to a synopsis of non-invasive tomographic techniques for multiphase flows by Chaouki et al [11]. The following discussion serves to provide background covering the history of tomographic imaging applied to multi-phase columns at the laboratory, pilot, and industrial scale.

2.2.1 Gamma-Ray Imaging in Industry

Possible the earliest use of gamma rays to obtain process measurements was exhibited by DuPont in 1962 [65]. A 60-mCi Cesium^{137} source was lowered simultaneously with a scintillation detector down the outside of a 42-inch diameter column. Measurements of radiation intensity were recorded every 2 inches. The resultant plot of intensity produced an axial density profile of the column. As described by Bowman [8], this technique has been refined and is used in industry to evaluate and troubleshoot column performance, as well as being used for preventative maintenance.

The use of dry scans, where no flow is applied to the column, allows for further analysis of scans obtained under flow conditions. By subtracting the dry gamma scans from the flow scans, a map of only the operating flow distribution can be obtained. Severance [66] reported on modifications to the initial scanning system used by DuPont, which included the ability to use differential scanning to improve the visibility of the liquid profile. This permitted identification of column malfunctions including foaming, tray flooding, and tray failure due to mechanical damage.

Modern gamma scans use several scans at a given height, typically obtained in a 2 x 2 parallel and orthogonal grid orientation, with the distance between source and detector identical for each scan. Scanning in this manner provides a more detailed look at the uniformity of column internals and process fluids. The added enhancement of pairing radiation scanning with computer simulation was discussed by Xu and Pless [83]. It was suggested that many engineers do not trust the hydraulic predictions provided by process simulators. Several reasons for this degree of doubt were provided, including the fact that existing hydraulic correlations were validated only for general physical systems and do not contain important geometric parameters for packing and trays. The combination technique was demonstrated on an erratically performing de-ethanizer. Analysis of field

investigations concluded that the column was flooding; however, simulations conducted to match the field variables showed operating points of the trays to be well below the weeping line on the operation-capacity diagrams. The weeping behavior was confirmed by performing gamma scans of the column, where trays with light liquid loads were observed. Stationary gamma scans conducted over a period of time at the heights of interest identified in the first scan showed the behavior on certain trays to follow the erratic cycles observed in the column reboiler control loop. The combination of scanning techniques and process simulation to improve column modeling and performance was encouraged.

2.2.2 Gamma-Ray Imaging of Packed Columns

Gamma-ray computed tomography was used to examine liquid holdup and distribution in an industrial-sized packed column by Xu and Kennedy [82]. The studies were performed in a 3-foot diameter Plexiglas column with 5 feet of random packing. The liquid phase in this case was water; no vapor flow was applied. The scans were taken in the horizontal plane 6 inches above the bottom of the packed section. Scans were conducted at nine different locations around the perimeter of the column, with nine detectors used to measure the intensity of the transmitted gamma rays for each source location. Using the method of Bartholomew and Casagrande [6], density maps were regressed to represent the liquid distribution. The maps matched well with experimental data taken by placing a segmented collector at the bottom of the packed bed. By integrating the difference between density maps under flow conditions and the maps without liquid flow, the liquid volume fraction for a given area was determined. While the image resolution was too low to gain any insight as to the small-scale flow characteristics necessary for rigorous modeling, this technique successfully observed

large-scale phenomena and provided one example of a validation technique for hydraulic models.

Experiments using gamma-ray tomography were carried out by Wang et al. [80] in a 0.6-m diameter column. Three different sizes of metal Pall rings (16, 25, and 38 mm) were used. The objective was to detect the presence of any spatial patterns in bed porosity. The scans, taken at several locations throughout the height of the dry packed section, showed the radial variation of porosity and confirmed that bed porosity is higher near the column wall. Each scan plane was imaged by moving the Cs^{137} source to one of twelve equally spaced locations around the column perimeter. The gamma-ray transmission was measured along seven chords at each source location, resulting in 84 scan lines per plane imaged. The greater understanding of bed porosity gained by this study was used to improve the accuracy of computational fluid dynamics (CFD) simulations based on volume averaged equations.

Using the same scanner and column as Wang and coworkers, Yin et al. [85] measured liquid holdup for 25.4 mm metal Pall rings. Scans were taken at two horizontal planes in the packed section, at bed depths of 200 and 600 mm, and for liquid flow rates of 2.39 and 4.78 kg/m^2-s. The liquid used was water. No gas flow was applied. Three different liquid distributor designs were used to investigate the effect of initial liquid distribution on liquid holdup distribution within the packed column, and a strong correlation between the two was observed. Based on the tomographic data, liquid holdup was modeled using the volume averaged Navier-Stokes equations in a CFD simulation. Holdup was shown to vary radially and axially in much the same manner as Wang et al. [80] showed porosity to vary in a dry bed of random packing. Successfully matching simulation to experimental data is a basic step in designing for scaled-up applications using models.

2.2.3 Gamma-Ray Imaging at Washington University

Gamma-ray CT was used to obtain void fraction distribution in bubble columns of varying diameter by Kumar and Dudukovic [33]. Five different column diameters were imaged: 0.10, 0.14, 0.19, 0.26, and 0.30 m. Water was used as the stationary liquid phase, with air being bubbled up through the column via a perforated plate distributor. A bubble cap riser distributor and cone distributor were also used. The liquid level in the column was maintained so as to produce a minimum height to diameter ratio of five. A variety of flow regimes were studied by varying the superficial gas velocity between 0.02 and 0.12 m/s. The scanner consisted of a 100 mCi Cs^{137} source paired with an array of eleven 2" x 2" NaI scintillation detectors in a third-generation configuration, i.e., the source and detectors were rotated around the column. The scanning assembly could be moved up and down with respect to the object being imaged. Scan speed was limited by the scanning assembly being able to be rotated at a maximum of one revolution per minute. Also, the increased spatial resolution achieved by collimating the 40^{o} fan beam added to the required scan time.

Further studies of bubble columns using gamma-ray CT were performed in the work of Kumar et al. [32]. The goal of the work was to investigate the effect of gas maldistribution at the inlet. Again, air and water were used as the process fluids. The column had a diameter of 26 cm. A perforated plate distributor was used for the vapor, with half of the holes plugged to simulate the initial maldistribution. The superficial vapor velocity for the study was 5 cm/s. The effect of column height on improving poor distribution was studied by scanning at elevations 17, 27, 83, and 121 cm above the vapor distributor. As expected, at the lowest elevation, the gas distribution was poor. A more uniform density distribution was observed at the higher elevations, indicating that the distribution of phases had improved. A smaller column of diameter 13.9 cm was used to

compare the results observed with the larger column. While in good agreement at low and high gas velocities, the void fraction calculated from CT deviated from the expected values at intermediate gas rates.

Additional investigation of gas holdup in bubble columns by Kumar et al. [34] focused on altering column diameter, distributor type, scan plane location, gas velocity, and liquid phase physical properties. The consistency of the experiments was verified by performing identical experiments on successive days. Experimental values for gas holdup obtained from the CT images were compared with the values calculated from pressure-drop and bed-expansion methods. The holdup observed in the middle of the column varied from experiment to experiment under the same operating conditions. The physical properties of the liquid phase were manipulated by adding isopropanol to water. In a 50-50 mixture, the bubbles observed were smaller than those in only water, which was expected with the decreased surface tension. The gas holdup for that system was also significantly higher.

The scanning system used by Kumar was utilized by Chen et al. [12] to investigate the behavior of an air-drakeoil system in two different bubble columns. The first column had a diameter of 44 cm, a height of 240 cm, and was constructed of Plexiglas. A perforated plate distributor was used, with 0.076% open area and holes of 0.77 mm diameter. The static liquid level was held at 160 cm. The superficial gas velocities used were 2, 5, and 10 cm/s. Four heights were imaged: 51, 89, 132, and 170 cm. The second bubble column had a diameter of 10 cm and also used a perforated plate distributor. The holes on the second column's distributor were of 0.5 mm diameter, and the open area was equal to 0.23%. The vapor velocities used were identical to those in the first column, but the static liquid height was 120 cm in the second case. At a superficial gas velocity of 10 cm/s, the gas holdup profiles were nearly symmetric, yet

they became asymmetric as the gas rate decreased. As in previous studies, the gas holdup was observed to be higher in the center of the column. At different axial locations, similar radial holdup distribution profiles were observed. The holdup measurements indicated that the holdup was lower in the column with larger diameter. This behavior was attributed to the larger diameter holes and lower open area used in the vapor distributor on the larger column.

Further work on gamma-ray CT of bubble columns was reported by Kemoun et al. [31]. The stainless steel column used was of diameter 0.162 m, height 2.5 m, and was pressurized from 0.1 to 0.7 MPa. Air and water were selected as the process fluids. A perforated plate distributor was used to introduce the gas into the column. It had 61 holes, each 0.4 mm in diameter, yielding a total open area of 0.04%. The superficial gas velocities used for the experiments were 0.02, 0.05, 0.12, and 0.18 m/s. The process was operated batchwise with respect to the liquid. Only one scan height was studied, and it was located 0.92 m above the distributor. The gas holdup was shown to increase with system pressure, with the degree of increase being correlated to the superficial gas velocity. At low gas rates up to approximately 0.05 m/s, the holdup increased only slightly with system pressure, while the holdup increases more dramatically with pressure at higher superficial velocities. Additionally, the radial gas holdup profile was shown to become flatter as pressure increased, indicating that the system was moving from a churn-turbulent flow regime to a more stabilized bubble regime. The results from the CT experiments were also compared to existing correlations for average gas holdup, with none consistently predicting the behavior observed through experiment.

Roy et al. [52] used the imaging equipment of Kumar to investigate a liquid-solid circulating fluidized bed. The lab-scale column was 210 cm tall and 15 cm in diameter. The solid phase was made up of glass beads with diameter of 2.5 mm. The liquid phase

used to fluidize the riser section of the bed was water, which was then recirculated. Four different axial locations were imaged for liquid rates ranging from 12 to 23 cm/s. A mixing zone was identified from the small solids holdup observed near the entrance of the column. The solids holdup was shown to vary with both radial and axial position, with the holdup being highest in the center of the column. This was opposite of the behavior observed in gas-solid systems. Computer-automated radioactive particle tracking (CARPT) was also performed on the riser to obtain solids velocity patterns and verify behaviors such as solids backflow.

Further work by Roy et al. [54] used the same gamma-ray CT scanner, CARPT system, and cold-flow circulating fluidized bed, including the glass beads of 2.5 mm diameter as the solid phase. The solids distribution in the riser was found to be uniform, with minor accumulation of solids near the vessel wall. No variation in solids was seen in the three scan planes located at heights of 0.5, 1.0, and 1.5 m in the riser. Liquid rates of 0.15, 0.20, and 0.23 m/s were used, at varying solids-to-liquid flow ratios of 0.10, 0.15, and 0.20. The average solids holdup at a given cross section was shown to increase with increasing solids flow rate at a constant liquid flow rate. The same property also decreases with increasing liquid flow rate at a fixed solids-to-liquid flow ratio. The CARPT technique showed the solids to be flowing upward in the center of the column, downward near the column wall, and having zero axial velocity where the dimensionless radius is approximately 0.8, signifying gross convective backmixing. Net flow in the radial direction was negligible compared to axial velocity for the solid phase.

Flow distribution in a column containing structured packing was investigated via gamma-ray CT by Roy et al. [53]. The column diameter was 30.48 cm with a height of 152.4 cm. The material of construction was Plexiglas. The column contained four elements of a Norton-type packing made of stainless steel with 45^{o} corrugation angle.

Each element was 27.3 cm in diameter and height. Water and air were contacted countercurrently in the packed column. The vapor superficial velocity ranged from 0 to 10 cm/s, and the liquid rate varied from 0.6 to 2.6 cm/s. These rates correspond to a vapor F-factor less than 0.1, and liquid rates in the trickle flow regime, thus the column was characterized as operating in the preloading zone for structured packing. The scanner was the same as previously used by Roy, Kumar, and coworkers, with modifications. The source used was an encapsulated Cs^{137} isotope, with gamma-ray energy approximately equal to 70 mCi. The detector array consisted of 9 NaI detectors of diameter 5 cm. The source and detectors were rotated around the column to obtain transmission data. The new detector setup eliminated the need to interpolate between detectors, as the angular distance between adjacent detectors has been reduced to match the angle between beam projections. Validation experiments confirmed a spatial resolution of approximately 2.5 mm. The packed section was imaged at levels of 1.5, 2.5, and 3.5 times the diameter of the packing from the top of the packed section. Total scan time for the column was approximately 5 hours. Liquid saturation, or the ratio of liquid volume to bed void volume, was observed to increase as the liquid travels down into the bed, and also to increase with liquid rate. Vapor rate was not seen to effect the flow distribution, largely due to the low vapor superficial velocities studied.

The focus of gamma-ray imaging experiments was shifted to an upflow monolith reactor in the work of Al-Dahhan et al. [3]. Water and air flowed co-currently upward through the monolith. The vapor and liquid rates chosen were from 0.3 to 0.5 m/s for each phase to achieve flows in the Taylor regime. The monolith used for the study had a diameter of 4.8 cm, a length of 0.152 m, and a cell density of 400 cells per square inch. The device was fixed inside a clear PVC pipe of diameter 5 cm. The flow channels were of square cross-section, with a characteristic length of approximately 1 mm. The gamma-

ray CT scanner used was the same as in the work of Kumar [33]. A modified detector collimator increased spatial resolution to 2 mm in the horizontal direction. The CT technique was shown to accurately predict the average bed porosity. Maldistribution of air and water due to wall effects at the entrance to the monolith was quantified by CT. However, this behavior prevented calculation of distributed holdup within the bed. The study emphasized the need to carefully design entrance and exit regions of monoliths.

2.2.4 X-ray Imaging of Fluidized Beds and Bubble Columns

A fluidized bed containing coal particles was scanned by Banholzer et al. [5]. The solids were fluidized by air at room temperature in a 43 mm diameter polyacrylic tube of length 150 mm. Two layers of nylon mesh with openings of 34 μm were used to distribute the air as it entered the bed. A General Electric 8800 Series medical scanner was used to obtain the images. It consisted of a rotating anode X-ray tube capable of producing X-ray intensities from 20 to 120 keV in a 30^o fan-beam geometry that was 1500 μm thick. The detector array contained 517 gas-filled X-ray detectors. This produced images with a spatial resolution of 0.24 x 0.24 mm^2. The total time for one scan was 9 seconds, with 576 views being collected during one rotation of the source and detector gantry.

Scans of the fluidized bed were taken under static conditions, near minimum fluidization, and in the bubbling regime. Unlike the cross-sectional images obtained through gamma-ray scanning of bubble and packed columns, the images produced in this study were vertical slices taken along a diameter of the fluidized bed. Bed void fraction was calculated from the images. A vertical gradient of void fraction was observed for the static condition. It was suspected that compression of the particles in the bed was the cause. A more pronounced gradient was observed top-to-bottom for the case where the

bed approached minimum fluidization. The images obtained during operation in the bubbling regime showed a bypass region in the middle of the bed where void fraction was significantly higher.

Kantzas [28] modified a medical X-ray scanner to investigate holdups in fluidized and trickle beds. The source energy of the 4th-generation machine could be varied between 100 and 140 kVp, and the gantry could be adjusted to scan objects in either a horizontal or vertical orientation. Each slice of data could be acquired in 3 seconds, with the resulting images representing a time average of the flow over that period of time. The scanner could visualize an object with a maximum diameter of 32 cm.

A 10 cm diameter fluidized bed packed with either 20-30 mesh glass beads or 0.4 cm polyethylene particles was used for the first portion of the experiment. The column was 100 cm tall, with the packed bed portion accounting for 15 cm of the height. Nitrogen was used as the fluidizing media. The packed section was imaged through a series of scans at a constant nitrogen pressure. Additional slices above and below the orifice tube distributor were taken while varying the gas rate. The resolution of the images was 0.04 x 0.04 cm^2, with the slice thickness equal to 0.5 cm. The holdup in the bed was shown to be relatively constant by plotting average gas holdup as a function of bed elevation. There was shown to be a large radial variation in gas holdup, which led the researcher to conclude that defining bed holdup in one dimension was an oversimplification. Scanning of one slice continuously for 30 minutes provided insight into the time variation of the bed density. The average gas holdup values obtained from the time-variant experiment were within a 0.04 range. Investigation of mixing patterns was achieved by tagging a portion of the polyethylene particles with sodium iodide to increase the X-ray absorption. The tagged particles were packed in the bottom of the bed, and covered by untagged polyethylene. While scanning the bed under a constant

pressure of nitrogen, it was observed that vigorous mixing occurred in the center of the column, but not at other locations.

Kantzas then studied the behavior of a trickle bed, which consisted of a Plexiglas column 4.5 cm in diameter and 0.45 m in height. The column was packed with glass beads with sizes from 0.4 to 0.6 mm. The column was scanned at a resolution of 0.4 x 0.4 mm^2, with a 3 mm slice thickness, resulting in a total of 150 images. Sequential scans at this resolution covered the entire column, first under dry conditions, then under vacuum while saturated with water, and finally with water circulating from top to bottom at a rate of 1.57 cm^3/s. Despite the packing being uniform, the liquid holdup was shown to vary between cross-sections. The average water fractions calculated ranged from 0.74 to 0.91.

The studies of Kantzas were successful in showing that, while flow dynamics could not be captured via CT due to the inherent time averaging that occurs while a scan is being performed, differences in those time averages are discernible and measurable. The work also served to show that macroscopic column measurements do not capture the small-scale behavior needed to fully understand flow in these types of devices.

Further studies using the same modified medical X-ray scanner were performed by Kantzas and Kalogerakis [29] and Kantzas et al. [30]. High-density polyethylene, linear low-density polyethylene, and impact polypropylene resin were used as the solid fraction in the bed in separate experiments, with the particle size distribution varying. The column used as the packed bed had a diameter of 10 cm. The height of the packed bed varied to provide height to diameter ratios of one, two, and three. Several fluidization velocities were studied, using ambient air or nitrogen as the fluidizing phase. The image resolution used for the experiments was 0.4 x 0.4 x 3.0 mm^3. Channeling was observed in the bed, as the density of the particles was not uniform even at low gas rates.

As in previous studies, it was noted that there was significant radial variation in the void fraction.

The same modified medical scanner was used by Zarabi and Kantzas [86] to investigate fluidized beds utilizing high-density polyethylene and linear low-density polyethylene particles. The bed particles were of a very narrow particle size distribution, and were either 1.50 or 0.75 mm in size. The density of the 1.50 mm high-density polyethylene resin was 0.942 g/mL, while the 0.75 mm particles had a density of 0.943. The density of the linear low-density polyethylene was 0.917 g/mL. For a given flow condition, the entire column was scanned in 3 mm increments at a resolution of 0.4 x 0.4 mm^2. The effect of fluidization number, Froude number, and Archimedes number was investigated in the experiments. Analysis of the images depended on selection of two threshold values to differentiate among the dense phase (bed), emulsion phase (fluidized portion), and the gas phase. Bubbles in the column were measured and compared to correlations for bubble size. The number of bubbles in a given cross section was also determined from the X-ray CT images. The effect of gas rate, bed elevation, and particle morphology were studied, in addition to evaluation of the phase distribution.

Grassler and Wirth [18] used a 60 keV fan-beam X-ray source with an array containing 1024 detectors to characterize the concentration of solids in a circulating fluidized bed. The studies focused on the performance of two separate fluidized beds, each constructed of Plexiglas. The source and detectors rotated around the columns during the scans. The 0.19 m diameter, 14 m tall riser section was subject to upflow of gas, while the downflow section was 8.5 m tall, with a diameter of 0.15 m. Glass beads ranging from 50 to 70 μm in diameter were used in both beds. The superficial gas velocity through the beds varied from 2 to 7 m/s. The images were reconstructed from 128 angular views of the object during a scan, which took 20 to 40 minutes to complete

for each cross section of interest. The spatial resolution of the 256 x 256 pixel images was 0.8 mm. The results of the experiments showed a parabolic profile of the solids distribution, with a maximum near the column wall. The parabolic shape persisted even as the circulating mass flux and superficial velocity were varied. Analysis of the CT images showed the average solids fraction by volume to vary from 2% to 20%.

A fast X-ray CT scanner was used by Kai et al. [26, 27] to investigate the dynamic effects in a fluidized bed. The 1.5 m long bed was constructed of polyacrylic resin, had a diameter of 46 mm, and was packed with silica alumina particles with a broad size distribution. After settling, the bed height was 0.86 m. The density of the particles was 980 kg/m3, and the mean particle size was 36 μm. Ambient air was used to fluidize the bed, and the superficial gas velocities ranged from 0.005 to 0.07 m/s. The scanner used for the experiments consisted of multiple X-ray sources encased in a single vacuum chamber. Eighteen electron guns each had their emitted electrons increased to 100 kV by a high voltage source. The detector array contained 122 $CdWO_4$ scintillation detectors equally spaced at 2.55 mm intervals in a semicircle around the fluidized bed. The X-ray beam was collimated to a 3 mm thick, 24^o fan. The system could acquire images at only one height in the bed, but at a very fast rate of 250 slices per second, enabling the capture of rising bubble interface structures.

The first portion of the analysis involved visualization of the density distribution across the column cross-section. To eliminate noise and systematic errors, the reconstruction algorithm subtracted from the flow image an image of the bed after settling but before gas flow was applied. The ascending velocity of bubbles was calculated from a relationship between superficial gas velocity and bubble holdup. This technique was shown to be valid for bubble velocities up to 1 m/s. Using 500 slices obtained over in a 2 second scan, a 3-dimensional representation of a bubble interface

was obtained. It was shown that the particle density of the lower part of the bubble was higher in the central portion as opposed to the periphery, as expected in the complicated wake region of a rising bubble. The main bubbles also did not appear spherical, but rather as elongated regions and collections of several smaller bubbles. The work successfully used an X-ray scanner with sufficient temporal and spatial resolution to resolve bubble behavior in a fluidized bed. The importance of bubble surface area in determining mass transfer properties in such a bed was especially addressed by the 3-D experiments. However, the low X-ray source energy used would prohibit this scanner being used to image flow in a column containing metal packing.

Hubers et al. [22] investigated multiphase flow in a 32.1 cm diameter, 4.87 m tall bubble column using X-ray computed tomography. The scanning equipment consisted of two portable X-ray tubes with adjustable voltage and two image intensifiers acting as detectors offset 90^{o} from each other. The scanning system is capable of X-ray radiography, X-ray computed tomography, and X-ray stereography, although only one source and detector pair was used for the study presented. A CCD camera is paired with each image intensifier to read the image, with a motorized lens located between the camera and image intensifier to focus the intensifier output onto the CCD pick up area. The sources and detectors are mounted on a slew ring 101.4 cm in diameter, which allows the scanning equipment to rotate around the object being imaged. When used for X-ray computed tomography, an image is taken every 1^{o} as the source and detector rotates around the object, resulting in 360 projections. A filtered back-projection algorithm is used to reconstruct CT images from the projections. The column is situated on a vertical lift that permits scanning at different axial locations. Multiple slices can be obtained in one rotation by considering multiple rows of pixels in the CCD camera pick up array. The resulting data can then be reconstructed to provide a three-dimensional,

time-averaged representation of the flow field. The time required to complete one scan, including calculations for unwarping the data and normalizing the pixel response linearly, is approximately 20 to 30 minutes. More sophisticated algorithms for unwarping, normalization, and beam hardening correction increase the scan time to approximately 1 hour. Image reconstruction requires 15 minutes on a 64-node Linux cluster.

The X-ray CT system was first characterized by imaging a phantom object. Several hollow tubes, 1.52 m in length and of diameters ranging from 0.13 to 15.88 mm, were mounted to a board and placed inside the column. The tubes were constructed of acrylic, PVC, or Teflon. The ends of the tubes were capped so that they contained only air, even when the column was filled with water. The phantom was imaged at an X-ray source voltage of 141 kV. The cross-sectional images obtained showed signs of ring artifacts and beam hardening. The smallest tube that could be resolved was 6.35 mm in diameter. The next smallest tube used in the phantom had a diameter of 1.6 mm, so it is possible that tubes between these two sizes might be resolved. Three-dimensional images of the volume of air in a 10 cm height of the tubes were reconstructed. The images of the largest tube appeared distorted, which was attributed to a combination of beam hardening and thresholding used to filter the slices for three-dimensional visualization.

Computed tomography images were then obtained for a static multiphase system consisting of air, water, and cellulose fibers. The gas was dispersed by a stainless steel distributor plate with 953 holes 1 mm in diameter, resulting in an open area of 95%. The system was studied at superficial gas velocities of 3, 10, and 18 cm/s. The cellulose fibers used in the slurries had an average length of 2.3 mm and a dry density of approximately 1500 kg/m^3. The experiments were performed with two different fiber mass fractions, 0.l% and 1.0%. The water-fiber slurries were treated as a single pseudo-

fluid due to the low fiber mass fractions used and the fact that the X-ray absorption characteristics of the system were similar to that of water. The images obtained in the study were at a column height of 290 cm, which corresponds to roughly 9 column diameters. This ensures that entrance effects of the gas are avoided and that the flow is fully developed. Gas holdup was shown to become more parabolic as the superficial gas velocity increased for the air-water system. When fibers were added to the system, the gas holdup profile changed. At 0.1% by mass, the holdup observed was slightly higher in the center of the column than the air-water case. When small in number, the fibers serve as a separating medium for small bubbles, and reduce interaction between bubbles. However, when the fiber mass fraction was increased to 1.0%, a decrease in gas holdup was observed at all radial locations in the column when compared to the air-water system. This was attributed to the increase in effective viscosity of the liquid phase, where shorter-dwelling large bubbles are required to break through the fiber network.

2.2.5 X-ray Imaging of Packed Columns

Liquid distribution in trickle beds was studied by Lutran et al. [37]. A medical X-ray CT scanner was used to image flow in a Plexiglas column packed with either 3 mm or 6 mm diameter glass spheres to a height of 19 cm. The total height of the square column was 30.48 cm, and the inside length of a side was 6.03 cm. Water was distributed into the column via a plate with 25 holes arranged in a 5 x 5 pattern. Barium bromide was added to the liquid phase to increase the absorptivity for improved contrast. A second liquid system, comprised of a mixture of water and ethanol, permitted the study of the effect of surface tension on flow pattern. The liquid was recycled through the column, drawn from a square tank at the bottom that served as a sump. The liquid rates used for

the experiments were 11.5 mL/s, 23 mL/s, and 33 mL/s. Vapor flow was not applied to the column.

The orientation of the scanner resulted in images that represented vertical slices through the column. The time required to complete a scan of the column was 26 seconds. Slices were taken every 3 mm as the column and recycle pump moved through the scanning plane on a conveyor belt. The column was imaged while dry, and then at increasing liquid flow rates. The effect of pre-wetting on liquid distribution was studied by repeating lower flow rates after the maximum liquid flow had been applied.

The results of the experiments showed that the flow pattern in the column was strongly influenced by pre-wetting. For the case where the bed was not pre-wetted, the flow was dominated by filament flow. However, when the bed was pre-wetted, the flow pattern tended toward film flow. Film flow was also more likely when the larger 6 mm diameter spheres were used in the column. The void space between adjacent spheres was large enough to prevent films from coalescing to form filaments. The authors also observed a reduction in liquid spreading in the column for the lower surface tension liquid system.

Toye et al. [73] used X-ray computed tomography to analyze phase distribution in trickling filters. The scanner used for the studies consisted of an X-ray source capable of producing a 40^{o} fan beam with a maximum energy of 160 kV, paired with a linear array of 1024 photodiode detectors. The source and detectors were arranged in a way that allowed them to rotate around the object as well as move up and down. The maximum object size that could be scanned was 0.8 m in diameter and 2 m in height. The spatial resolution was on the order of 1 to 2 mm, and the time required for a scan was approximately 2.5 minutes.

The trickling filter was constructed by packing a 2 m tall, 0.6 m diameter polyethylene column with Etapak 210 random polypropylene packing. The type of packing used has a characteristic diameter of 0.05 m and void fraction of 0.95. The specific area of the packing is 220 m^2/m^3. Along with the packing, water and air comprise the three phases present in the filter during operation. The void fraction of the packing was verified by analyzing X-ray CT images of the dry packed column. The packing was noted to be non-uniformly distributed at different elevations. Liquid holdup was measured from the tomographic images by subtracting the X-ray transmission data for the dry bed from that of the bed under irrigated conditions. Images were then reconstructed from this new set of data, with the holdup calculated being in good agreement with dynamic holdup measurements determined by a tracer technique.

The same scanning system and trickling filter was used in further studies by Toye and coworkers [74]. The purpose of the new experiments was to examine the flow regime from X-ray CT images. The liquid rates varied from 0 to 14.5 gpm/ft^2, with water again serving as the liquid phase. The water was introduced at the top of the packed bed via a 4-point liquid distributor. As in the previous work, CT images representing the local dynamic liquid holdup were reconstructed by subtracting the raw data acquired from a scan of the dry bed from the raw data taken of the irrigated case. The images showed rivulet flow on the surface of the packing elements. Thus, it would be expected that liquid distribution could be correlated to the distribution of packing in the column. The authors concluded that poor distribution of packing in a column is one of the leading causes for liquid maldistribution when the column is operated. The number of rivulets was shown to grow proportionally with increasing liquid flow. As the flow was increased however, the rivulets began to coalesce and liquid spreading was reduced.

A 0.6 m diameter, 2 m tall column filled with polypropylene #1A Cascade Mini Ring (CMR) random packing was imaged using X-ray CT by Toye et al. [75]. The packing elements were 0.044 m in diameter, 0.016 m tall, and exhibited a void fraction of 0.92 and specific area of 185 m^2/m^3. The X-ray scanner used was the same as that used in prior work by Toye and coworkers. Again, the column was imaged under dry and irrigated conditions, with the raw data from the dry scans being subtracted from the wet scan raw data to reconstruct images of the liquid holdup. The images were processed such that the holdup was calculated by taking the average of regions six pixels by six pixels. This eliminated the geometric detail of the flow. The results compared favorably to holdup calculated from a partial wetting model based on probability.

Additionally, Toye et al. [76] reported on the use of X-ray computed tomography to investigate liquid holdup in a column containing #1A CMR random packing. Table tennis balls were first used as phantoms to characterize the X-ray system. Under dry bed conditions, the X-ray technique was able to reproduce the vendor specified void fraction of 0.92. The axial profile of void fraction showed that the effects often associated with the top and bottom, or ends, of the bed could be neglected, but that there was a significant radial variation in void space, commonly expressed as the wall effect. Using water as the liquid phase, dynamic holdup was measured at several locations in the column and averaged to provide a bulk value. The column average holdup from X-ray CT images was shown to exhibit power law behavior when plotted as a function of liquid superficial velocity, with the exponent of 0.65 falling within the range of exponents found in existing correlations.

Using the same 0.6 m diameter column, Marchot and coworkers [38] investigated liquid maldistribution for #1A polypropylene CMR packing. The spatial resolution achieved was approximately 0.1 mm. Water was used as the liquid medium, and no

vapor flow was applied to the column. The maldistribution was simulated by using three different types of liquid distributors, each with a different drip-point density. The packed column was scanned at several elevations for liquid rates ranging from 1.5 to 8.7 gpm/ft^2. The six-by-six pixel averaging technique was used in calculating the local liquid holdup at each elevation and flow rate. The flow patterns in the column were further characterized by calculating both maldistribution factors and radial dispersion coefficients. Maldistribution was defined at both the bed scale, caused by poor initial distribution and column wall effects, and the particle scale. Local liquid superficial velocities were calculated from local dynamic liquid holdup using an Ergun-like equation.

X-ray computed tomography was applied to polypropylene structured packing by Marchot et al. [40]. The column was the same piece of equipment in previous studies by Marchot, Toye, and coworkers. Four elements of Sulzer Mellapak 250Y were installed in the column, resulting in a packed bed height of 1.24 m. Water was fed to the bed via a liquid distributor with 106 drip points per square meter. Air was applied from the bottom of the column. The superficial velocities for water ranged from 0 to 0.006 m/s, while air rates varied from 0 to 2 m/s. The X-ray scanner was the same device used in the work of Toye et al.

For dry packing, the average void fraction was calculated from CT images, with the average value from X-ray analysis at four separate slices matching the vendor-specified value. A series of 18 scans, vertically separated by 1 mm, were combined to produce a 3-dimensional representation of the packing structure. Analysis techniques used to create the surface from the CT images resulted in the packing appearing thicker than it is in reality. Computed tomography images that superimposed the liquid location on images of dry packing were produced to investigate liquid distribution for the cases

where liquid and vapor flow was applied to the packed bed. The distribution was shown to improve from one packing element to the next. However, increased liquid holdup was observed near the discontinuous interface of two packing elements. A three dimensional representation of the liquid flow field in a small portion of the packing was obtained by stacking slices of CT images where the dry bed data had been subtracted from the irrigated bed data. The three-dimensional liquid flow pattern was overlaid on a three dimensional representation of the packing surface. These volumetric images also exhibited an increase in apparent thickness for both the packing and liquid due to the analysis techniques used during reconstruction. The work was extended by Olujic et al. [43] to quantify the variation in holdup at packing element interfaces. Further analysis of the techniques used in creating three dimensional images of both dry and irrigated packing was presented by Marchot et al. [39].

A reactive distillation packing was investigated using a newly developed high energy X-ray computed tomography scanner by Toye and coworkers [77]. The scanner was comprised of an X-ray source capable of output energies from 30 to 420 kV. The 40^{o} fan beam is collimated by a lead filter to a thickness of 1 mm. The minimum focus size of the source is 0.8 x 0.8 mm. The detector array is composed of 1280 photodiodes in a linear array, with a pixel pitch of 0.4 mm, pixel width of 0.3 mm, and pixel height of 0.6 mm. Each photodiode is coupled to a $CdWO_4$ scintillator. The total detector array is 512 mm long. A mechanical rig was designed to rotate the object being scanned. The new setup permits the object to be raised and lowered over a 3.8 m range. This is in contrast to the previous scanner setup used by Toye, in which the source and detectors were rotated around the object and moved up and down to achieve various scan planes. The scanner is capable of imaging objects up to 0.45 m in diameter. Both computed

tomography and radiography may be performed with the new system. Scan time varies from 45 to 180 seconds, depending on the number of views specified per rotation.

The system was first calibrated using a 100 mm diameter Pyrex cylinder filled with water as a phantom. The grayscale values of water in the CT images were very uniform, indicating that beam hardening artifacts were absent. Measurements of the column wall thickness and diameter through analysis of CT images agreed well with the actual values. One element of Montz B1-250 structured packing was also imaged to validate the new X-ray scanner. The packing is constructed of 0.2 mm thick corrugated sheets of stainless steel, has a diameter of 0.38 m, and exhibits a specific surface area of 244 m^2/m^3 and a void fraction of 98%. The packing sheets possessed an embossed surface texture, but were not perforated. A dry CT image of the structured packing was presented, and beam-hardening artifacts did not appear to be present.

Tomographic measurements were performed on one element of Sulzer KATAPAK-SP-12 catalytic distillation packing. The element was 0.09 m in diameter and 0.20 m tall. The packing consists of a series of 2 corrugated sheets of regular Mellapak PLUS perforated and embossed structured packing followed by a catalyst basket. There were a total of 8 sheets of Mellapak PLUS and 3 catalyst baskets in the element. The catalyst baskets are constructed of wire gauze, and typically contain catalyst particles, in this case Amberlyst. For the CT studies however, the catalyst particles were replaced by 3 mm polypropylene spheres. The packing void fraction specified by Sulzer is 0.82, with a catalyst volume fraction of 24.2%. The overall specific area of the element is 236 m^2/m^3.

The packing was first imaged under dry conditions, with details of all the components clearly visible. Both CT slices and a three dimensional reconstruction were presented. The volumetric image exhibited the same issue with apparent thickness as in

Toye's previous studies. Both perforations and surface texturing were discernible in the volumetric reconstruction. The packing was also characterized in service with only liquid flow applied. The glass column used had a diameter of 0.1 m and height of 1 m. A single point source liquid distributor was used, providing a drip point density of 127 points per square meter. Liquid superficial velocity varied between 13 and 38 m^3/m^2-h. Eight different locations in the packing element were imaged at distances between 10 and 150 mm from the feed point. The liquid flow was observed to split as it approached the central catalyst basket. The majority of liquid holdup was observed in the corrugated sheet zones, although the presence of liquid within the catalyst basket was verified by the CT imaging. As expected, the holdup also increased with increasing liquid superficial velocity. The new scanning system successfully exhibited the ability to investigate characteristics of metallic structures without the influence of beam hardening artifacts.

Deshusses et al. [14] applied X-ray computed tomography to the study of a biotrickling filter. A General Electric medical scanner was used for the experiments. The slices were taken with 3 mm spacing, and the resolution of the images was approximately 0.3 mm. The vessel was constructed of clear PVC tubing with a diameter of 15.2 cm, and filled with 2.5 cm Pall rings made of polypropylene to a bed height of 1.3 m. The filter was partially clogged with biomass. The CT images showed regions where Pall rings were either partially or completely covered with material. Significantly wall effects were presumed due to the location of the biomass channels observed in the tomographic images. The presence of large channels permitted the calculation of interfacial area from the CT images, where the sum of the measured perimeter of all air channels in a slice was divided by the reactor cross-sectional area.

The liquid phase distribution observed in random and structured packings was investigated using X-ray CT by Schmitz and coworkers [60, 61]. The scanning system

used consisted of a fixed X-ray tube source and an array containing 15 detectors. The source produced a 40^{o} fan beam of X-rays that was 2 mm in thickness. The source was set at a voltage of 360 keV and current of 4 mA for the experiments. To reduce beam hardening, a filter with 2 mm of aluminum and 3 mm of copper was placed on the front of the X-ray tube. The time required to obtain one image was 15 minutes at a spatial resolution of 0.4 x 0.4 mm^2.

A 200 mm diameter acrylic column of height 250 mm was used for the flow experiments. Ceramic spheres of diameter 10 mm were used as the random packing. The structured packing used in the column was Sulzer Mellapak 250Y, constructed of metal. Water was used as the liquid phase, and was distributed at the top of the column via a perforated plate distributor. The distributor contained 177 holes 1 mm in diameter. A maximum water flow rate of 30 m^3/m^2-h was used.

The column was imaged under both dry and irrigated conditions. The CT images of the dry column were subtracted from the CT images from flow scans to obtain the liquid distribution. Liquid holdup was calculated for both random and structured packing from the liquid only images. The liquid distribution observed for the ceramic spheres was irregular. Liquid was observed primarily in areas where the density of ceramic sphere was high, which the authors attributed to the high affinity for water that the spheres possessed. The liquid distribution was shown to change dramatically along the axis of the column. For the case of structured packing, a water film was observed over the entire surface of the packing. The thickness of the film was not constant, but dependent on location in the packing element. The upper surfaces of the packing housed a film that was three to four times thicker than the films on the underside of the packing. Local accumulation of water was observed at the points were adjacent corrugated sheets were close to each other. Axial variation of holdup was not observed for the structured

packing. The values obtained for liquid holdup were in good agreement with the data of Suess and Spiegel [71]. When a countercurrent gas flow was applied, the distribution in the column was observed to improve. Reinecke and coworkers [48] presented a pseudo-three-dimensional representation of the data obtained for ceramic spheres.

Using the same X-ray scanner, Schmitz et al. [62] studied the flow pattern observed for an air-water system using Sulzer OPTIFLOW structured packing. Three elements of the packing were installed in a 700 mm tall, 200 mm diameter column. Barium chloride was added to the water to increase the X-ray attenuation for improved contrast. The surface tension of the system was reduced from 0.6 N/m to 0.032 N/m in selected experiments by adding surfactants. A perforated plate liquid distributor with 177 1.2 mm diameter holes was used. No gas flow was applied to the column.

The column was scanned at 1.2 mm spacing in the bottom-most packing element resulting in 40 CT slices, each requiring 15 minutes to obtain. The liquid flow rate for the experiments was 10 m/h. The CT images for the dry and flow cases were subtracted from each other to produce images of the liquid distribution. Water was shown to accumulate at the intersections of the metal sheets. The design of the packing resulted in elevations where only liquid pockets accumulating at intersections were visible, and other elevations where no gross accumulation was observed, only a thin film. Liquid holdup was plotted as a function of bed height, with the calculated values ranging from 1% to 8%, with an average value of 3.05%. In the studies where surface tension was modified, the liquid holdup was reported for five different liquid flow rates ranging from 2 to 26 m/h. Three models were used to compare with the experimentally determined holdup values, with the values obtained from CT falling in the same range as the predictions for both fluids. The liquid holdup was shown to be slightly higher for the fluid with lower surface tension.

X-ray computed tomography was applied to a packed column by Cartmel [10]. A high-energy scanner operating at 420 kV was paired with a linear array of 125 detectors. The system design mandated that the object be rotated during the scans. The total time required for one scan was approximately 5 minutes for detector apertures of 0.2 x 0.2 or 0.3 x 0.3 mm^2. The arrangement of the detectors required the object to be translated perpendicular to the X-ray path several times and re-rotated to produce a full set of data.

The system was first characterized by imaging a 2-foot tall, 6-inch diameter acrylic column under zero flow. The column contained 5 separate packed beds, each containing a different type of packing. Random packings used included both metal and plastic ballast rings (5/8 in.), and plastic #0A and #1A CMR. Sulzer BX wire gauze structured packing was also installed in the column. One slice was taken in each bed and used to determine the smallest features that could be resolved by the system, in addition to the void fraction. The calculated void fractions for each material compared favorably to the values provided by the manufacturers.

An air-water contactor was constructed to investigate the liquid flow patterns observed in a packed bed during operation. The height of the packed section was 16.6 inches, and the overall height of the contactor was 48 inches. The column was also constructed of acrylic, and had a diameter of 6 inches. The column was packed with 5/8-inch metal ballast rings. Water was fed to the top of the packed bed through a 4-point liquid distributor, and air was applied via a ring-type distributor at the bottom of the column. Scans were obtained for a variety of liquid flow rates, vapor flow rates, and column elevations. A three dimensional image of a 3.2 mm thick section near the bottom of the bed was produced by layering a series of CT images acquired under flow conditions. Liquid holdup was calculated from CT images and X-ray transmission data. The results were compared with those obtained by a technique to measure the bulk

holdup of the column. Further discussion of the imaging studies was presented by Schmit et al. [57].

Schmit [56] used the air-water contactor designed and imaged by Cartmel to further explore the application of X-ray computed tomography to packed columns. A phantom system was developed to characterize the ability of the X-ray scanner, also the same used by Cartmel, to discern features present in an operating air-water contactor containing structured packing. Liquid holdup was calculated from transmission data at several elevations for each of the phantom objects and compared to the expected values based on the geometry of the phantoms. The results fell within 10% of the expected values. A second apparatus was constructed to investigate the accuracy of X-ray CT in predicting the thickness of a liquid film. A nominal 3-inch Schedule 10S polished stainless-steel pipe was installed in the air-water contactor, with liquid flow being applied to the center of the pipe from the bottom. The water was allowed to fill the pipe and spill over the outer edge, creating a thin liquid film on the surface. The thickness of the film was successfully calculated from transmission data to within 10% of the value predicted by the Navier-Stokes equations, with the films measuring from 0.2 to 0.4 mm. The experiments also showed that high levels of measurement noise were detrimental to the analysis of the transmission data, and thus must a consideration in addition to spatial and temporal resolution. The results of the phantom and film flow experiments were also reported by Schmit and Eldridge [58].

Additional studies on the air-water contactor containing structured packing were conducted by Schmit. Two elements of Sulzer Mellapak 500Y metal structured packing were installed in the air-water column and imaged using X-ray CT. The packing has a specific surface area of 507 m^2/m^3 and a void fraction of 0.975. The liquid holdup in the packed section was calculated from X-ray transmission data at several elevations in the

column and for flow rates ranging from 2.2 to 20 gpm/ft^2 for water and F-factors of 0.14 to 0.27 for air. Stationary transmission measurements were made on the column while it was operating and showed significant variation in the flow pattern despite the ordered structure of the packing elements. Liquid accumulation above the joint of the two packing elements was observed, even at the sub-loading flow rates used. The liquid holdup values obtained from CT analysis were compared to several predictive models and traditional experimental data for bulk holdup. Computer simulations of X-ray CT were performed to pinpoint the cause of ring-like artifacts in flow scans. These artifacts were attributed to a combination of liquid movement during transmission data acquisition and the use of subpositions in the data acquisition process. Further discussion of the simulations and structured packing experiments have been discussed by Schmit et al. [59].

2.3 Summary

A variety of models for predicting packed column performance exist. Even the most widely accepted of these models contain limitations. The application of these models is limited to systems similarly to those used to validate the models. Many of the models incorporate experimentally correlated coefficients, restricting use to the packing types used in developing the model. Although more rigorous models continue to be proposed, such as those developed using computational fluid dynamics, a dependence on experimental correlations for transport behavior remains.

Any new model, regardless of complexity, will require experimental data for validation. Models, such as those utilizing CFD, are becoming increasingly more intricate, with the ability to capture small-scale local behavior that has been ignored up to

this point. These models will require experimental data that is in sharp contrast to the traditional data used for model validation.

CHAPTER 3: EXPERIMENTAL EQUIPMENT AND PROCEDURES

3.1 Principles of X-ray Computed Tomography

X-ray computed tomography is one example of a non-destructive testing (NDT) method. The technique is used to non-invasively and non-intrusively obtain detailed cross-sectional images of objects, including the internal structure. Non-invasive imaging does not require sensors to be placed inside of the object for measurement and therefore does not alter the object being imaged. This makes X-ray CT a good choice for obtaining data otherwise unavailable from traditional methods of testing.

In X-ray CT, X-rays are transmitted through the object of interest and measured after they pass through the object. The X-ray intensity that is measured depends on the size of the object and the object's material of construction. A material's linear attenuation coefficient, μ, is a measure of the degree to which X-rays are attenuated when passing through a differential length of material, dL, as defined in Equation 3-1.

[3-1] $$\frac{dI}{I} = -\mu dL$$

This expression shows that the change in X-ray intensity is negative as the incident beam passes through the object, as shown in Figure 3-1. For an object of uniform composition and length L, the final intensity of an X-ray beam with initial intensity I_o is given by Equation 3-2. When the composition of the object is non-homogeneous, the X-ray intensity is described by the more general Equation 3-3, where non-constant linear attenuation coefficients are integrated along the X-ray path, z.

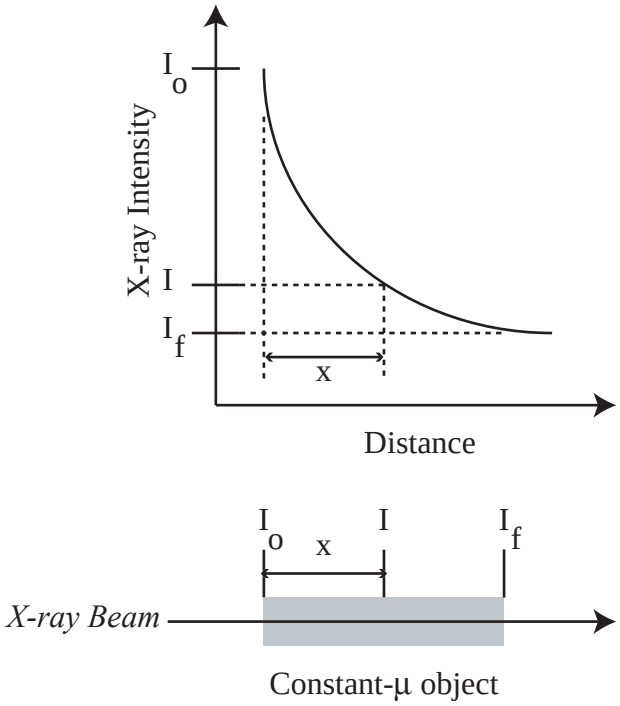

Figure 3-1. Attenuation profile for monoenergetic X-ray passing through a uniform object

Linear attenuation coefficients are proportional to the density of the material, and generally increase with the atomic number of the material [1]. The coefficient is also dependent on the energy of the X-ray beam. Attenuation is typically more pronounced at lower X-ray intensities [20], which can be troublesome when a polyenergetic X-ray source is used. As the beam passes through the object, X-rays of lower intensity will be preferentially attenuated, resulting in modification of the energetic profile of the X-ray beam. This phenomenon is known as beam hardening, and it results in an X-ray beam with higher average energy than the initial beam. Filters are often used to pre-harden the X-ray beam. However, beam hardening can still be significant in cases where long lengths of extremely dense material are present along an X-ray path, or when low-energy X-ray sources are used. In such cases, artifacts are often present in the reconstructed

images. Image artifacts are features in an image that are not representative of the actual physical system being imaged. They may be caused by a variety of scenarios in addition to beam hardening.

[3-2] $$I = I_o e^{-\mu L}$$

[3-3] $$I = I_o e^{-\int \mu(z)dz}$$

The inverse Radon transform is the mathematical basis for X-ray CT. This relationship allows a function *f(x,y)* to be uniquely determined from an infinite set of line integrals of the same function. The desired function *f(x,y)* in the case of X-ray CT is the distribution of the object's linear attenuation coefficient, which can be mapped in two-dimensional coordinate space. The line integrals used to determine the function are the measured values of X-ray attenuation at different projections. By rearranging Equation 3-3 to the form of Equation 3-4, it is easier to see how the measured data relates to the line integrals. The attenuation data measured by the X-ray scanner is fed to an image reconstruction algorithm that approximates the inverse Radon transform. The output of the algorithm is an array that represents the linear attenuation coefficient at different points within the object space.

[3-4] $$-\ln\left(\frac{I}{I_o}\right) = \int \mu(z)dz$$

3.2 Measurement Equipment for X-ray Computed Tomography

The basic setup for an X-ray CT scanner requires an X-ray source and a set of detectors arranged on opposite sides of the object to be imaged. For most medical X-ray CT systems, the source and detectors are rotated around the object to obtain transmission data at a variety of radial positions. However, it is not uncommon for industrial X-ray CT scanners to rotate the object of interest and keep both the source and detectors fixed.

Transmission tomography in general involves a variety of different choices for radiation sources. Industrial systems commonly employ isotope decay sources, x-ray tubes, or linear accelerators to produce X-rays for CT scanning purposes. Isotope sources usually produce X-ray beams of one energy level, although some isotope sources can product two distinct energy levels. The X-ray flux of isotope sources is usually much lower than that of tube or linear accelerator sources. Linear accelerators are capable of producing higher energy X-rays than tube sources, although the beams produced by both types are polyenergetic. The higher energy X-rays produced by linear accelerators are necessary to avoid beam hardening when imaging large objects constructed of very dense materials, as is common for some industrial applications of X-ray CT.

The detectors used in X-ray CT applications generally fall into one of two categories. Scintillation detectors contain fluorescent material that visibly emits radiation when exposed to X-rays. Optical enhancement devices, such as photodiodes or photomultiplier tubes, are connected to the detector to convert the light emitted to an electrical signal. Ionization detectors typically use a Noble gas that produces a measurable current when energy is transferred to it by incident X-rays. Regardless of the detector style used, arrays can be constructed using a large numbers of detectors. These arrays are usually linear and can be either flat or curved, depending on the geometry of the X-ray beam. Some systems permit the effective area of the detectors to be varied by

adjusting the aperture or considering only certain rows and columns from a digital detector. Adjusting the vertical aperture of the detectors controls the thickness of a CT slice.

The X-ray transmission data necessary for image reconstruction may be obtained in a variety of ways. Several generations of CT scanner design have consistently improved the time required to obtain cross-sectional images. The first-generation scanner geometry consists of a point X-ray source and one detector. The source and detector are simultaneously translated to obtain measurements along a number of parallel ray paths. The source and detector are then rotated to a new angular position and the translation process is repeated. The procedure continues until data has been acquired from 180^{o}. A second-generation scanner utilizes a fan-beam X-ray source. This allows measurements to be obtained for several ray paths at once, although translation and rotation is still necessary to acquire a full set of transmission data.

Significant improvement is achieved with third- and fourth-generation scanning systems. For a third-generation system, a fan-beam source is used with multiple detectors arranged in a curved array. This eliminates the need for source and detector translation assuming the detectors are continuous, i.e. no space exists between adjacent detectors. Rotation is still required to acquire all data necessary for reconstruction. A fourth-generation scanning geometry contains a continuous set of detectors that comprise a circle around the object being scanned; only the fan-beam source is rotated.

The improvement of scanner design continues to be an active area of research. Recent developments include the use of multiple sources in a single scanner and the application of cone-beam sources combined with area detectors (two-dimensional detector arrays) to image a volume of the object rather than just a slice. Spiral scanning, where the simultaneous rotation and translation of the source and detectors or object

occurs, allows for quick acquisition of a large set of volumetric data. Many of the applications first appear in the medical field and are subsequently adapted to industrial work. Advancements in scanner design usually necessitate improved or altogether new image reconstruction algorithms, particularly when the scanner geometry and method in which data is acquired have changed.

In addition to the source and detectors that are contained in a tomography system, the mechanical assembly is also of great importance. Precise control of the machinery used to manipulate the object, source, and detectors is critical. Image reconstruction algorithms as well as processing techniques applied to the resulting CT images depend on the manipulator moving with precision and being able to return to certain locations with exacting accuracy. The associated electronics must be designed to ensure proper communication between all related components of the system.

Depending on the geometry of the X-ray system, the transmission data that is collected represents a set of line integrals of the linear attenuation coefficient as was described by Equation 3-4. The transmission data can be interpreted as either parallel-beam data, or fan-beam data. Parallel-beam data is defined as a function of the angle θ between the X-ray path lines and the axes of the object space, and the distance t of a given X-ray path from the center of rotation. For fan-beam geometry, the parameters describing the projection data include the angle between the central ray of the fan and the axes of the object space, β, and the angle γ between the central ray path and alternate ray paths. Figure 3-2 depicts the parameters for different scanner geometries in the object space and transmission data space. A sinogram is the result of displaying transmission data as an image, where the axes of the image are either θ and t or β and γ, depending on the geometry used. When the location of a feature in the object is tracked through the image, a sine wave is produced, hence the name given to the image.

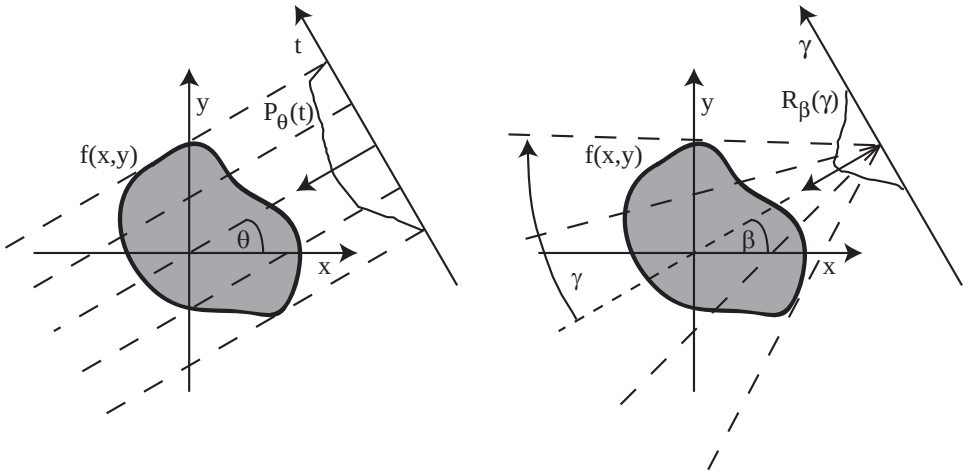

Figure 3-2. Geometry definitions for parallel-beam (left) and equiangular fan-beam (right) X-ray CT.

3.3 Image Reconstruction for X-ray Computed Tomography

Several standard image reconstruction algorithms have been presented by Leahy and Clackdoyle [35] for both 2-D and 3-D data. The two most commonly used algorithms are the algebraic reconstruction technique and the filtered backprojection method, which is implemented for both scanners used in this work.

The algebraic reconstruction technique, or ART, is one example of an iterative method for image reconstruction. The technique uses iteration to solve the system of line integral equations defined by the transmission data by altering an image matrix representing the object imaged. Convergence is achieved with the particular image matrix that provides the best fit to the data. This algorithm is particularly effective when the amount of available transmission data is low.

Filtered backprojection is clearly the most commonly used image reconstruction technique for X-ray CT applications. The mathematical basis for the technique is the Fourier slice theorem, which states that the one-dimensional Fourier transform of the parallel projection of an object at angle θ corresponds to values along a radial line in the frequency domain, also at angle θ, as shown in Figure 3-3.

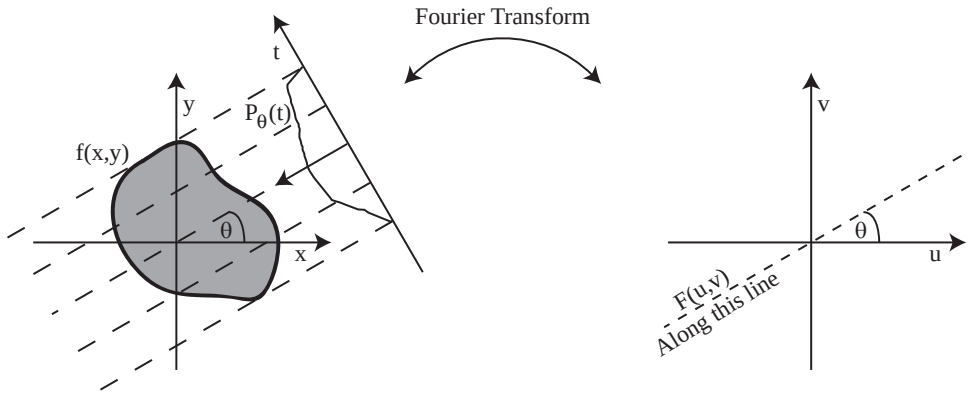

Figure 3-3. Illustration of Fourier slice theorem applied to parallel-beam X-ray CT transmission data (spatial domain on left, frequency domain on right).

For a function defined as $f(x,y)$, the Fourier transform $F(u,v)$ is given by Equation 3-5. Rosenfeld and Kak [51] showed that the Fourier transform of the an object's projection, $S_\theta(w)$, is equal to the Fourier transform of the function, $F(u,v)$. Converting to polar coordinates in the frequency domain, $u = w\cos\theta$ and $v = w\sin\theta$. Substituting these expressions results in Equation 3-6.

[3-5] $$F(u,v) = \int_{-\infty}^{\infty}\int_{-\infty}^{\infty} f(x,y)e^{-j2\pi(ux+vy)}dxdy$$

[3-6] $$F(u,v) = F(w,\theta) = \int_{-\infty}^{\infty} P_\theta(t) e^{-j2\pi wt} dt = S_\theta(w)$$

Assuming the X-ray CT technique could acquire data for an infinite number of projections, the original function $f(x,y)$ that represents the cross-sectional image could be reconstructed by applying the inverse Fourier transform. Regardless of how many projections are obtained using X-ray CT, they are still finite. This is one cause of image degradation. While this discussion has been focused on parallel-beam projection data, a similar result can be obtained for fan-beam data. Usually the fan-beam data is converted to parallel-beam data or a set of similar equations particular to fan-beam data are derived.

The filtered backprojection algorithm makes use of the Fourier slice theorem to reconstruct images from projection data. The first step is to take the Fourier transform of the projection data as shown in Equation 3-6. Filters are applied to the projection data in the frequency domain to improve the quality of the image by reducing noise and improving sharpness. Shown in Equation 3-7, the filtered projection, $Q_\theta(t)$, is determined by approximating $|w|$ via a mathematical filter and applying the inverse Fourier transform. Examples of filters commonly used in filtered backprojection algorithms are the Ram-Lak, Low-pass cosine, Hamming, and Shepp-Logan filters [25].

[3-7] $$Q_\theta(t) = \int_{-\infty}^{\infty} S_\theta(w)|w| e^{j2\pi wt} dw$$

Finally, the backprojection is performed to produce the reconstructed image. In this step, each pixel in the image is determined by the contribution of all filtered

projections. Equation 3-8 shows the relationship between the filtered projection data $Q_\theta(t)$ and the original function $f(x,y)$.

[3-8] $$f(x,y) = \int_0^\pi Q_\theta(t)d\theta = \int_0^\pi Q_\theta(x\cos\theta + y\sin\theta)d\theta$$

The output of the reconstruction algorithm is a digital image comprised of discrete picture elements, or pixels. As resolution increases and pixel sizes become smaller, the discrete image becomes a closer approximation of the continuous object it represents. Each pixel, usually of square dimensions, is assigned a discrete value representing the value of the function in a particular region. The elements in CT images are sometimes referred to as voxels, or volume elements, because the CT slice exhibits a finite thickness determined by the X-ray beam and detector aperture. Thus, voxels represent discrete three-dimensional subvolumes of the object being imaged. Additionally, CT images may also be interpreted as a two-dimensional array of intensities mapping the distribution of linear attenuation coefficients for an object.

X-ray CT images come in a variety of formats, but the most popular are grayscale images 8 to 16 bits in size. The bit size of an image is related to the number of gray levels possible in the image. The formula that determines these values is (2^n-1), where n is the bit size of the image. Therefore, 8-bit images can have pixel values ranging from 0 to 255, with 0 corresponding to black, pixels with a value of 255 displaying as white, and values in between scaling linearly. Image file formats also vary, but lossless formats such as the TIFF (tagged image file format) standard are preferred so as not to lose any pixel information through file compression.

3.4 X-ray Computed Tomography Scanners Used

Two different X-ray CT scanners were used for the imaging experiments carried out in this work. The first scanner is owned and operated by 3D Imaging & Development, Inc. [3DID; formerly Scientific Measurement Systems (SMS)] in Austin, Texas. The second scanner is located at the General Electric Quality Technology Center in Cincinnati, Ohio. This system, known as the Industrial Computed Tomography (ICT) scanner, is used primarily for quality assurance from the neighboring General Electric Aircraft Engine plant. Both of the imaging systems, referred to as the 3DID and GE scanners, consist of measurement equipment to obtain the projection data and reconstruction and analysis software to produce and refine images. The 3DID scanner is a pseudo-third-generation system, whereas the GE scanner is a true-third-generation machine. A comparison of the key features of each scanner is given in Table 3-1. In both cases, the object being imaged is rotated rather than the source and detectors.

Table 3-1. X-ray CT Scanner Specifications

X-ray Scanner	3DID	GE
X-ray source maximum energy (kV)	420	6000
Detector Type	Scintillator	Scintillator
Number of Detectors	125	1024
Detector Aperture	0.2 – 1.0 mm	1.5 mm
Maximum Object Weight	50 lbs	500 lbs
Maximum Object Diameter	10 in	40 in
Maximum Scan Height	30 in	38 in
Maximum Object Height	6 ft	4 ft

Several key differences exist between the two scanners, although the most important are the X-ray sources and the detector arrays. The 3DID scanner uses a conventional X-ray tube source, whereas the GE scanner is equipped with a high-energy linear accelerator. The detector arrangement for the 3DID scanner is gapped; the detectors themselves are discretely spaced, resulting in an area on which X-rays are incident during operation but not detected, as noted in Figure 3-4, even if the X-ray fan beam is wide enough to span the object space. The larger GE detector array is continuous, or close-packed. This difference is the basis for designating the scanner as a pseudo- or true-third-generation device.

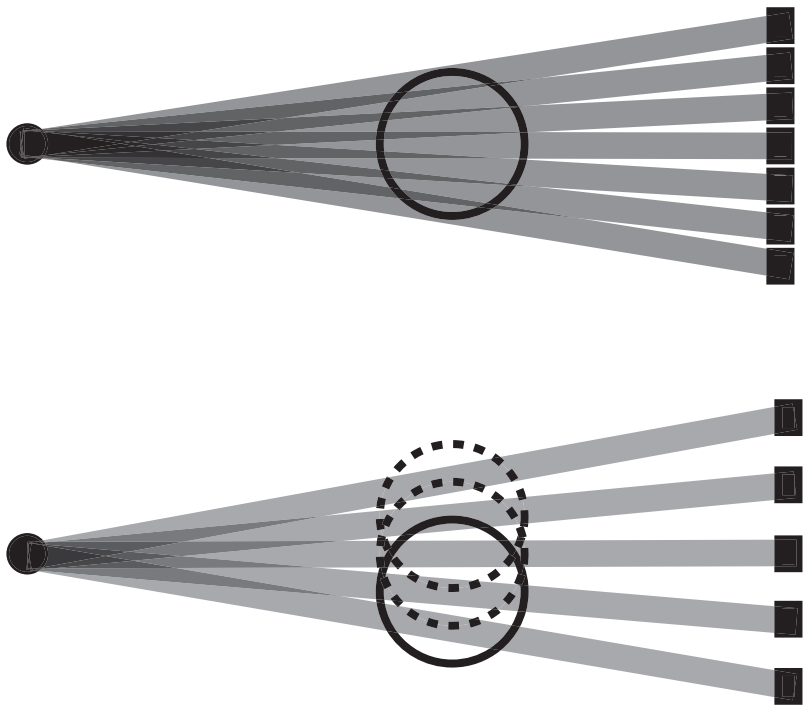

Figure 3-4. Detector arrangement for standard third-generation scanner (top) and pseudo-third-generation scanner requiring subpositions (bottom)

The spacing between detectors that exists for the 3DID scanner requires translation of the object being imaged to several different locations in order to acquire a complete set of transmission data for the object. After each rotation, the object is translated perpendicular to the X-ray path and rotated again. These translational locations are known as subpositions. The number of subpositions required is dependent on the horizontal detector aperture, with a larger aperture requiring fewer subpositions. While the adjustable aperture of the 3DID scanner permits the image resolution and resulting scan time to be varied, the added rotations required to account for detector spacing greatly increase the total scan time. Multiple rotations are necessary to acquire a full set of transmission data using the 3DID scanner, while only one rotation by the GE scanner produces a complete set of data. Subpositions were shown by Schmit et al. [59] to be one cause of undesirable concentric ring artifacts in CT images.

3.4.1 Specifications of X-ray CT Scanners Used

The initial experiments in this work were performed using the 101B+ scanner located at 3DID and described by Schmit [56]. The X-ray source is a Philips industrial X-ray tube capable of producing a fan beam with energies varying from 120 to 420 kV. A collimating device eliminates X-rays not traveling towards the object and detectors. The collimating device also permits the addition of metal plates used as filters to artificially harden the X-ray beam and reduce beam-hardening effects apparent in the CT images.

The 3DID scanner is equipped with a linear array of 125 scintillation detectors, equally spaced along an arc. Each of the detectors links to a photomultiplier tube used to convert the detector reading into raw numerical data, which is then recorded by a computer. A second collimating device is placed in front of the detectors to ensure that

only X-rays that have passed through the scan plane are considered. The detector aperture is variable from 0.2 to 1.0 mm, and adjustment is independent in either the vertical or horizontal direction. The value of the horizontal detector aperture defines the spatial resolution attainable, while the scan plane thickness is specified by the detector's vertical aperture.

Rotation and translation of the object is performed by a mechanical system comprised of drive motors and a turntable. Translation is available in three orthogonal directions. The direction perpendicular to the X-ray beam is required for the subpositions. Moving the object between the source and detectors determines the maximum object diameter that may be scanned. The last translational axis is vertical, allowing the object to be raised and lowered to scan different heights. Spatial encoders are used to determine the exact location of the object.

The computer system that controls the X-ray scanner, records data, and reconstructs images is a Sun workstation. The reconstruction algorithm used is filtered backprojection, incorporating the Shepp-Logan filter. The data is converted from fan-beam to parallel-beam during the reconstruction. An overlap correction may be applied to minimize the difference measured by adjacent detectors along the same X-ray path. The software used for these procedures is proprietary to scanners constructed by SMS, and the output exists as 8-bit TIFF images or an array of 32-bit floating-point numbers. The 3DID scanner is shown in Figure 3-5.

The GE scanner consists of a Varian Linatron linear accelerator X-ray source capable of producing a maximum X-ray energy of 6000 kV, or 6 MeV, but the scanner is typically operated with source energies of 2 or 6 MeV. Both of these values were used for the imaging studies contained in this work, with 6 MeV predominating. The beam is conical in shape, but is collimated to a fan inside the source by two lead blocks. The

beam passes through an adjustable pre-collimator where the slice thickness is set prior to reaching the object. Figure 3-6 depicts the GE scanner with the air-water column mounted for imaging.

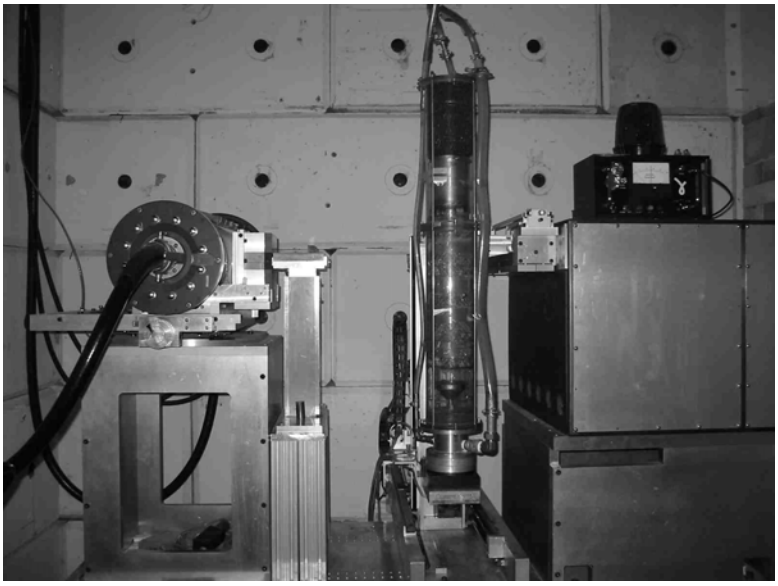

Figure 3-5. Air-water column mounted on 3DID scanner with X-ray tube source on left and detectors on right.

The GE scanner's detector arrangement is a one-meter long linear array of 1024 ceramic scintillator detectors placed consecutively along an arc without gaps. The detectors are digital, meaning they are solid-state devices that convert incident X-rays directly to numerical values without the need for the additional optical equipment in place on the 3DID detector array. A computer then records the projection data. The detector aperture is fixed at 1.5 mm. Each detector has a thin tungsten plate on each side to reduce cross talk between detector elements. The object being imaged is attached to a computer-controlled manipulator capable of moving the object in 8 different axes. Contrary to the 3DID setup where the object is moved up and down to achieve different

scan heights, the source and detectors comprising the GE scanner are both connected to a large beam that is raised up and down to the scan plane of interest. Measurement sensors are present to ensure precise locating of the object.

The computer system used in the GE scanner consists of a Hewlett-Packard computer and several networked hard drives for data storage. The filtered backprojection algorithm is used to reconstruct images. The software and data manipulation procedures used by GE are highly proprietary. The form of output is a 16-bit unsigned integer format, which can be converted to 16-bit TIFF images.

Figure 3-6. Air-water column mounted on GE X-ray CT scanner with X-ray source, pre-collimator, and detector array visible.

3.4.2 Scanner Startup Procedures

While the makeup of the two scanners used in this study may be quite different, the procedures that are performed when starting a scan are relatively similar. Initially, measurements are performed at different conditions to calibrate the detectors. For the case of the 3DID scanner, two measurements are performed; one with the X-rays turned off, and another with the X-rays only traveling through air, i.e. the column is not located in the scan plane. The GE scanner only performed an air calibration. No measurements were taken with the detectors off. The purpose of calibrating without the X-rays on is to account for variations between detectors. The air calibration with X-rays turned on serve to determine the initial intensity of the X-ray beam, which is required to determine attenuation due to the object in subsequent scans.

The 3DID scanner also requires a calibration to determine shift. The shift measurement determines the location of the object's center of rotation. The reconstruction algorithm requires this value to accurately reproduce images. To determine the shift value, a series of images is required by slightly shifting the object perpendicular to the X-ray path. The translation value that produces the sharpest images determines the shift.

The GE scanning procedure does not specifically require shift measurements at the start of a scan. However, the concept of shift is incorporated to other calibration procedures performed periodically. The computer interface used to control the scanner includes commands to verify the manipulator is properly oriented to produce quality images. A jig may be attached to the turntable and imaged to adjust the scanning geometry parameters in the computer system. This procedure is known as CT-Center. Once CT-Center has been completed, a metal bowl that has been precisely milled to different radii is scanned. The operator confirms the size of the bowl by measuring the

CT images; if the measurement from CT images agrees with the known physical dimensions of the bowl, then the scanner has been calibrated. This procedure is typically required after the manipulator and computer system suffer any communication errors.

3.5 Description of Experimental Systems Scanned

The air-water column used for the imaging studies, shown in Figure 3-7, was inherited from the work of Cartmel [10] and Schmit [56]. The clear acrylic column consists of three sections, each with an outer diameter of 6 inches and an inner diameter of 5.75 inches. The sections are 6, 18, and 24 inches in height and have flanges on both ends used for connecting the sections together. The bottom flanges of the 18- and 24-inch sections contain a groove designed to hold an o-ring, providing a watertight seal. The 6-inch section has a groove on both flanges.

The acrylic sections are connected together and attached to a 3.5-inch tall aluminum base. There are two process connections on the base, one for liquid flow out of the column and the other for vapor flow into the contactor. The bottom of the base has a series of holes used to attach the column to the 3DID scanner turntable. When the GE scanner is used the column base is simply clamped to the turntable. Four stainless steel support rods are fed through holes on the flanges of the column sections and threaded into the base to provide additional mechanical stability. A schematic of the column is provided as Figure 3-8.

The lower section of the column contains the packed bed and the vapor distributor. The inverted cone-type air distributor has a base diameter of 4.5 inches and tapers to a 1/2-inch tubing connection that attaches to a 1/2-inch Swagelok fitting inside the column base. The base of the cone is covered with a perforated plate.

Figure 3-7. Acrylic air-water column used for imaging experiments.

Several types of structured packing were used in the air-water contactor for imaging experiments. Initially, two 8-inch tall elements of Sulzer Mellapak 500Y (a_p = 500 m^2/m^3, ε = 0.975 [45]) stainless-steel structured packing were installed in the column. Sulzer Mellapak is a corrugated-sheet structured packing constructed of stainless steel. The metal sheets are perforated to help equalize radial pressure profiles in the packing element and to promote liquid spreading, although quantifying the effects of

perforations on these properties would be difficult. The surface of the packing is also textured to enhance spreading of the liquid. Wire gauze strips called wiper bands are wrapped around the circumference of the element and bent towards the column wall prior to installing the packing. This helps direct liquid flow back into the packing element and prevent vapor channeling. The Y designation means that the angle of corrugation with respect to the horizontal is 45^{o}.

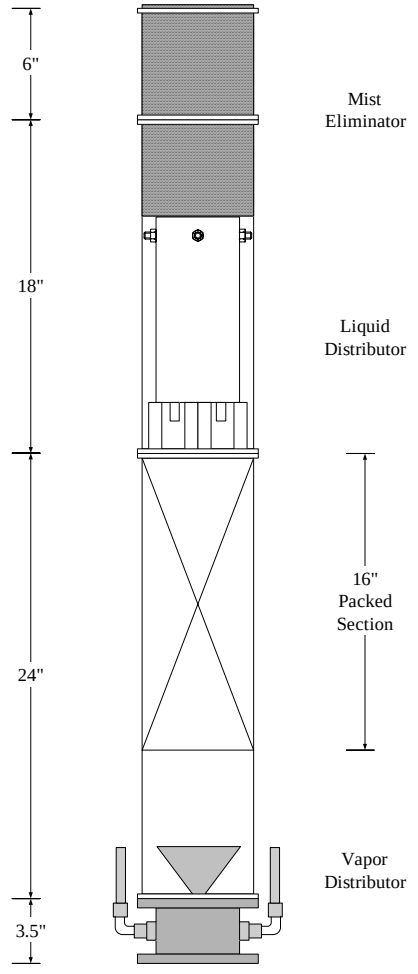

Figure 3-8. Schematic of the 6" air-water contactor used for X-ray imaging experiments.

To improve the liquid distribution, half-elements of 500Y were tested in the contactor. The packing was constructed of the same material, but at 4 inches tall was half the height of the original packing. It is believed that the interface between two packing elements acts as a liquid redistributor. To address different liquid flow patterns, a sample of less dense Mellapak 250Y (a_p = 200 m^2/m^3, ε = 0.987 [45]) was installed in the column. Both full and half elements of this packing were tested. All structured packing elements in this work were installed 90^o with respect to the previously installed element. The total height of packing for all Mellapak studies was 16 inches. The liquid flow rates used for the experiments were 2.2, 10.5, 15, and 20 GPM/ft^2. Vapor rates were F-factors of 0.14, 0.21, 0.27, 0.48, 0.65, 0.82, 1.00, 1.30, 1.40, and 1.50 (ft / sec)($lb^{0.5}$ / $ft^{1.5}$). Figure 3-9 shows the packing types used in the imaging studies.

Figure 3-9. Structured packings used in the imaging studies. From left, Mellapak 250Y half-element, 250Y full element, 500Y half-element, and 500Y full element.

3.5.1 3DID Scanner Flow System

The original setup for the air-water contactor as used by Schmit [56] was a once-through flow system. The vapor feed to the column is supplied by a Sullivan Industries

D130Q6 air compressor. This is a single stage diesel-powered screw compressor capable of a maximum flow rate of 130 ft^3/min. A 3/4-inch air hose delivers the air to the flow meter from the compressor. The air first travels through a drying filter to remove condensed water. The stream then passes through a Micro Motion Basis F050 mass flow meter. The signal from the flow meter is fed to a laptop computer via a National Instruments DAQCard-700 data acquisition board. LabVIEW software, also from National Instruments, is programmed to read the flow meter signal and totalize the flow over time. The process lines leading to and from the flow meter are 3/4-inch stainless steel tubing. Pressure and temperature gauges are present on the vapor feed line to analyze the properties of the air. The line delivering the air feed to the contactor is 3/4-inch outer diameter, 1/2-inch inner diameter flexible vinyl tubing. Two 3/4-inch NPT bore-through fittings are located on the aluminum base of the column. The fitting used as the air inlet has a 1/2-inch Swagelok adapter to connect to the air tubing. Airflow is controlled using a needle valve on the flow meter outlet line.

Water is fed to the column from the house water supply via a 5/8-inch outer diameter hose. A rotameter is used to measure the liquid flow rate. Before and after the rotameter, the liquid flow tubes are 3/4-inch stainless steel. The liquid flow continues to the column through 3/4-inch OD vinyl tubing and feeds into a four-point riser type liquid distributor designed by Koch-Glitsch, Inc. The drip point density is 22.2 points/ft^2. The feed tube to the distributor passes through the center of a 6-inch thick mist elimination device made of polypropylene mesh. After passing through the packed bed, the water accumulates in the bottom of the column. The second NPT fitting on the column base serves as the liquid outlet. The outlet line that connects to this fitting is also 3/4-inch OD vinyl tubing. Suction is provided by a 1/12-horsepower pump. The pump is turned on and a liquid level is maintained in the bottom of the column by manipulating a throttling

valve. The liquid taken from the column is fed to an on-site drain. Figure 3-10 shows a process flow diagram for the initial air-water contactor setup.

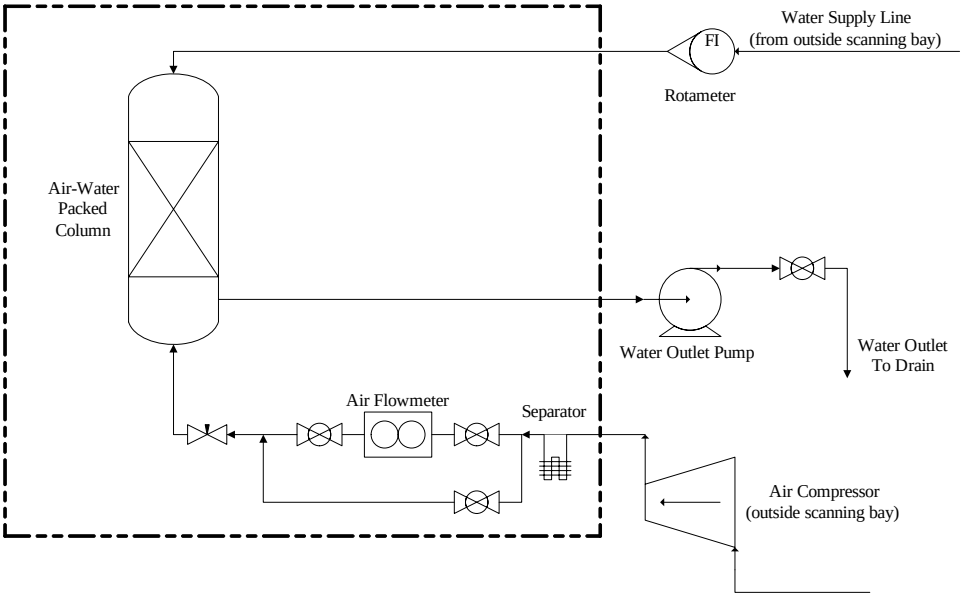

Figure 3-10. Process flow diagram for air-water column when 3DID scanner is used. Heavy dotted line indicates scanning bay containment wall.

While the air-water column system used in previous imaging work provided a convenient method to continue with research with minimal interruption, the design of the system had some shortcomings. The dependence on steady liquid flow rate from an on-site water source made controlling the liquid flow to the system difficult. Additionally, the relative inaccuracy of using a rotameter was in sharp contrast to the precise Coriolis meter used for measuring airflow. When the limitations of the subposition-dependent 3DID scanner became apparent, the decision was made to pursue using a more sophisticated scanner. The selection of General Electric as the service provider meant that modifications to the column equipment would be necessary in order to adapt to a

more restrictive scanner setup. The system needed to become more portable. A system was designed that can be operated remotely and utilizes a recycle stream for liquid flow instead of a once-through arrangement.

3.5.2 GE Scanner Flow System

The X-ray containment room that the GE scanner resides in is more extensive than the containment around the 3DID scanner. This is necessary due to the much higher energy X-ray source that is used. The only path into the scanning bay while the door is closed is through a trench in the floor. Modifications were made to the existing equipment setup to accommodate the unique challenges presented at the Quality Technology Center. However, no modifications were made to the air delivery system. The initial scans using the GE scanner used the in-house air supply. However, the flow was not sufficient to operate the contactor at industrially relevant vapor rates. Therefore, a diesel compressor similar to the model used with the 3DID scanner was obtained for subsequent experiments. The GE scanner flow system equipment is shown in Figure 3-11.

The existing air flow meter was mounted to a cart along with the stainless steel tubes connected to the inlet and outlet. A second Micro Motion Basis F050 mass flow meter was installed on the cart to provide measurement of the liquid flow. The flow meter was wired to the existing data acquisition card and the LabVIEW code was adapted to display and totalize both air and liquid flow.

To convert the liquid delivery system to a recycle configuration, a Price model CD100AI centrifugal pump was paired with a model M1105SC variable-frequency drive from AC Tech. This combination allows the pump speed, and thus flow rate, to be controlled from outside the X-ray scanning bay. By adjusting the amount of liquid in the

system via a bleed valve, a steady state liquid level is held in the bottom of the column below the vapor distributor. The liquid is pumped out of the bottom of the column, through the water flow meter, and back into the top of the column. The larger pump required the liquid lines to be resized. The majority of the flexible vinyl tubing for water is 1.25-inch OD, 1-inch ID. However, this tubing is not as flexible as the smaller tubing. The larger hose was not ideal during the rotation of the column on the scanner. Thus, a short section of the original 3/4-inch OD tubing is used for the feed line to the liquid distributor. The mist eliminator was also improved to help prevent liquid entrainment at the higher vapor rates used for studies with the GE scanner. A 9-inch tall bale constructed of a stainless steel and Teflon co-knit was obtained from ACS Separations & Mass Transfer Products. The distributor feed tube was routed through the middle of the mist eliminator and inserted into the distributor.

Figure 3-11. Flow system used with GE X-ray CT scanner. From left, air-water column, water pump, and cart containing flow meters. On top of the cart is the laptop computer and pump drive controller.

A new liquid distributor was designed by Koch-Glitsch, Inc. to replace the original design. The original distributor had four drip holes in the annular region between the distributor outer wall and the vapor riser. The new design utilized drip tubes instead of holes to ensure that liquid head was maintained in the distributor for flow rate assurance. The drip tubes have a series of holes drilled at various heights to achieve the desired range of flow rates. The modified process flow diagram for the GE scanner setup is shown in Figure 3-12.

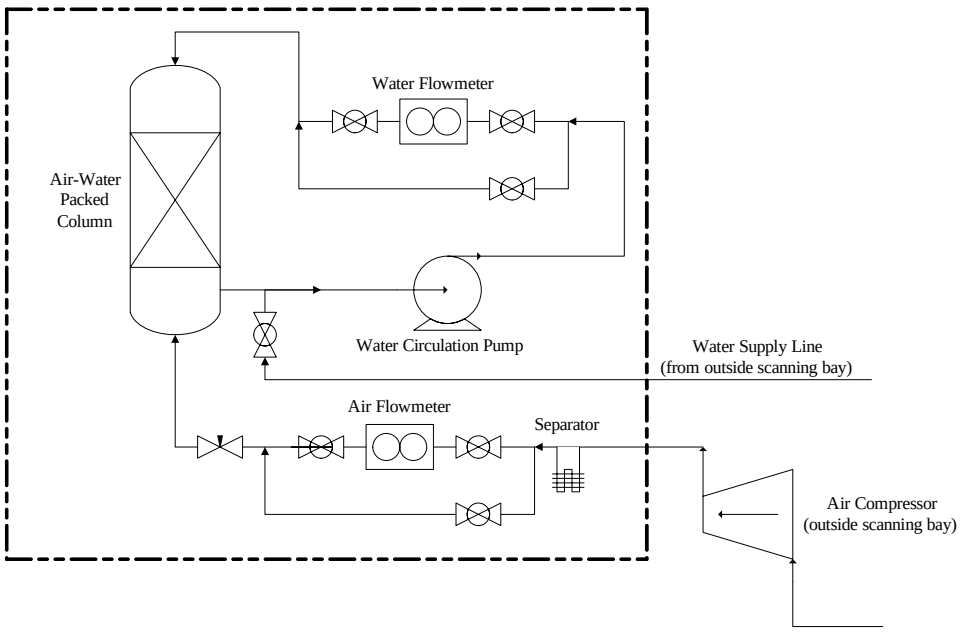

Figure 3-12. Process flow diagram for air-water column when GE scanner is used. Heavy dotted line indicates scanning bay containment wall.

3.5.3 GE Scanner Standard Startup Procedure

The procedure for assembling and operating the air-water contactor when imaged with the GE scanner was developed and practiced several times before the first actual

experiments were conducted. The equipment was packed and shipped to Cincinnati in such a way as to allow quick unpacking and setup.

Once all of the equipment is unpacked, the cart to which the flow meters are mounted is placed in the scanning bay. The pump is placed near the cart, and the air and water tubing is laid out. Next, the electrical cables providing flow meter signals to the laptop and the pump power cord are routed through the trench next to the scanning bay door. The pump power cord connects to the variable-frequency drive interface, which is then plugged into a 220V outlet. The flow meter signal lines have quick connect clips and plug into the data acquisition board. The ribbon cable from the circuit board plugs into the DAQCard installed in the laptop's PCMCIA slot.

The pump discharge line, which connects to the flow meter via the steel tubing on the cart, and the feed line to the air flow meter are typically the first process connections made. In addition to the air feed line, the water feed line must also pass under the scanning bay door. The water feed line connects to a PVC valve that leads to a tee in the pump suction line. By leaving the PVC valve open after the system is charged, the addition of water to the system to compensate for evaporation and entrainment can be achieved without having to enter the scanning bay; the house water valve is manipulated for this purpose. This allows the system to operate for long periods of time without the need to interrupt the X-ray scanning process, which is particularly valuable during the acquisition of three-dimensional modeling data.

Once all lines have been routed under the floor, the column can be mounted on the scanner turntable. The process connections to the column can then be made. The air inlet line connects the needle valve on the flow meter outlet to the air inlet fitting on the column base. As with any connection, care must be taken to ensure a tight fit. Hose clamps are used with layers of duct tape to prevent the hose itself from becoming

compromised. The liquid outlet line connects to the larger fitting on the column base and becomes the pump suction line. The two hoses that are fixed to the column base are fed through large washers that connect to the metal struts of the column. This provides a stable anchoring point for the hoses during column rotation. If necessary, duct tape will be used to ensure the hoses maintain relatively steady. The final process connection is the liquid feed. The tube is fed through the middle of the mist elimination device and routed into the annulus of the liquid distributor. Care should be taken to make certain that the feed tube does not slip onto a drip tube or into the vapor riser section. The tube should rest slightly above the bottom of the distributor pan. The mist eliminator is then packed into the top of the column.

The final step in preparing the column for scanning is to route the process connections to the column through a clamp attached to a beam above the scanner. Enough slack should be given to the lines so that the scanner can translate back and forth as well as rotate. Adjusting the hoses is usually a trial and error process. Once the proper alignment is achieved, the hoses can be taped together and fixed to the clamp to prevent slippage. The manipulator can be operated in a “dry-run” mode to test the rotation and stability of the column before actual experiments commence.

Once the X-ray scans of the dry column have started, it is important to avoid moving the column as it negatively impacts the image analysis. When dry scans are completed, the system can be charged with liquid. The PVC valve on the liquid supply line should be opened. The water is then turned on from outside the scanning bay, and the hoses are allowed to fill. As the amount of liquid in the system increases, the pump may be started to assist in filling all of the liquid lines. The amount of liquid required is usually enough to fill the bottom of the column up to the bottom of the packing. When enough water has been added, the water is shut off outside the scanning bay, but the PVC

valve is left open. The pressure in the supply line will prevent water from escaping the column's recycle loop. When first starting the system, water can be filled to a level equal or slightly higher than the packed section to pre-wet the packing and then be pumped out of the system.

The pump should be raised to its maximum output and allowed to run for several minutes to permit air to escape from the system. It is common for the system to be quite bubbly initially. A leak test is conducted to ensure that all connections are satisfactory. When the system has warmed up, the bleed valve on the pump is used to remove water from the system if necessary. As water is taken from the system, the level in the bottom of the column will drop. Once the level is below the vapor distributor, airflow should be applied to flush out the air line and distributor. The pump can then be adjusted to the desired flow rate and the liquid level finalized. At higher liquid flow rates, the level in the column will be lower. Also, entrainment and evaporation is higher at higher vapor rates. Thus, careful planning of the order of experiments will minimize the interruptions required. It is easier to start at low flow rates and work up, as it is easier to add water to the system to bring the level up if necessary than to remove water. Once the leak test is complete and liquid rate chosen, the air rate can be set and scanning can proceed.

3.6 Imaging Techniques Used

X-ray CT scanners are capable of producing a variety of output data. These data types are not limited to images. The numeric data representing attenuation that is used to reconstruct images can also prove valuable. Three basic imaging techniques were used to produce the data presented in this work.

3.6.1 Radiogram

In much the same way that conventional film radiography produces a two-dimensional image of X-ray transmission characteristics, a CT scanner can also be programmed to acquire the same type of data. A radiogram, which depicts the shadow an object projects as X-rays pass through it, is obtained by translating the object such that all measurements are taken along the same projection. There is no rotation during acquisition of a radiogram. For the pseudo-third-generation 3DID scanner, this involves translating the object vertically through the scan plane. The process is repeated at each subposition until the object has been completely characterized. The GE scanner accomplishes a radiogram by lowering the source and detectors simultaneously via the overhead beam they are both attached to.

The radiogram, also called a radiograph, is usually the first image taken, as it allows scan planes of interest to be defined for further investigation using X-ray CT. While the radiograph can identify the plane in which features of interest are located, it does not define the spatial distribution of those features within the plane. Radiographs are fairly quick to produce since they do not require rotation or image reconstruction. The radiogram itself is a visual representation of the integral of attenuation coefficients encountered along a given X-ray path.

3.6.2 CT Slice

The image that represents a cross-sectional slice of an object at a given location is known as a CT slice. To produce such an image, transmission data must be acquired for a number of different projections of the object. This is accomplished in X-ray CT scanning by rotating either the object or the source and detectors to acquire a full set of transmission data. Both the 3DID and GE scanners rotate the object to obtain projection

data, but the 3DID scanner requires the additional step of translating and re-rotating the object several times to account for the space between detectors.

Several parameters must be specified in order for the X-ray scanner to measure the data needed by the reconstruction algorithm to produce an image. The 3DID scanner requires input of the number of views, number of subpositions, snapshot time, and scan elevations. Similarly, the GE scanner input procedure specifies the number of views, number of integrations, scan spacing, number of slices, and start height (analogous to scan elevations), source energy, dimensions of the output image, coordinates of the center of rotation, and output image pixel size. The number of views specifies how many times data will be sampled for one rotation. Dividing 360^{o} by the number of views will yield the angular rotation between each data collection point. The GE scanner includes the number of integrations, which determines the degree of averaging that occurs between successive measurements to smooth out the data. For example, if a scan is set for 750 views and one integration, the data will be sampled 750 times. If 750 views and 2 integrations are used, the data will be sampled 1500 times, with adjacent measurements added together and divided by two. The snapshot time provided to the 3DID scanner determines the length of time that the detectors record data at each view.

Specifying the number of subpositions for the 3DID scanner determines how many perpendicular translations of the object will be performed during the scan, and thus, how many times it will be rotated. Scan elevations can be expressed individually or as a series. The GE scanner works slightly differently, with the start height, slice spacing, and number of slices specified. This method of input is related to the procedure used to acquire data for a three-dimensional model of the object, which will be explained later.

During the rotation of the object, each detector records a data point at each view. Therefore, the total number of data points recorded for reconstruction is equal to the

product of the number of detectors and the number of views. For the 3DID scanner, 900 views were obtained for each rotation, corresponding to rotational increments of 0.4^{o}. The number of views specified for the scans using the GE system was 750, equivalent to one measurement roughly every 0.5^{o}. Two integrations were used during the GE scans. To accommodate the unique demands of the air-water contactor, each scanner had an unwind step added to the computer's data acquisition code to prevent the tubing attached to the column from becoming tangled. Data was not recorded during the unwind step. This returned the object to its initial position in the rotational axis, at which time the manipulator would position the object at the next scan height or subposition. The 3DID scanner starts at the lowest slice and proceeds upward, while the GE scanner accomplishes multiples slices in the opposite manner. The time required to obtain a CT slice with the 3DID scanner was approximately 5 minutes. Without the need for subpositions, the GE scanner was able to acquire a CT slice, unwind, and proceed to the next elevation in 50 seconds.

The transmission data acquired in producing a CT slice may also be used to construct a sinogram. Sinogram images may be interpreted as radiographs of the slice of interest plotted versus rotational position. Each row of the sinogram is the object's projection for a particular view, with each column representing the integral attenuation measured along a given ray path for a particular view. For the 3DID scanner, a full row of sinogram values is not acquired at once due to the detector spacing. A number of spaces equivalent to the number of subpositions minus one will exist between values, and as rotations are completed for each subposition the spaces will be filled in. Sinograms provided by the GE scanner, however, are constructed continuously one row at a time, with each column representing one detector.

3.6.3 Stationary Transmission Measurements

While not considered a traditional X-ray CT imaging technique, the collection of stationary transmission data can be performed with small modifications to existing scanner operating procedures. Similar to CT slices and radiographs, stationary transmission data is a measurement of X-ray attenuation. X-rays are applied and detected, but the object of interest remains stationary. This permits the quantification of measurement noise and the variation of any property of the object that could be changing over time. The particular application of this technique to this work is to determine the flow variation at various locations in the air-water column over the course of a scan.

The measurements are acquired for a number of X-ray paths equal to the number of detectors. The stationary transmission experiments performed for this study used the GE scanner exclusively. Previous work by Schmit [56] applied the same technique using the 3DID scanner. For the GE scanner, the number of views was specified to determine the period of time data would be recorded. A data-sampling rate of 60 Hz was introduced to the scanner's operating code, and the manipulator was programmed to not rotate. For 1800 views, the scanner would record data for 30 seconds. The number of views (scan length) was limited by the available hard drive space for data recording. The output data was similar to an image sinogram, with each column representing a detector and each row representing a time step. The values of the pixels were indicative of the measured attenuation for a given detector and time. The average, minimum, maximum, and standard deviation were calculated at each detector for the various flow cases considered.

3.6.4 3-D Modeling From 2-D CT Slices

As was mentioned previously, the input procedures for the GE scanner required a start height, slice spacing, and total number of slices. This could be used to schedule a series of scans at equal spacing, such as completing a CT slice at 1-inch intervals in the

air-water column. However, the primary use of the GE ICT equipment outside the scope of this work is the development of three-dimensional models of objects. This can be accomplished using the CT slice procedure repeated extensively with very small changes in height between successive slices. Since each slice has a small but finite thickness, the data can be read into numerous third-party software packages and reconstructed volumetrically to form of a model. The models consist of volume elements, or voxels. Voxels are the 3-D equivalent of pixels. Commercial applications of this technique include reverse engineering, rapid prototyping, and quality control. In addition to CT slice output, data files known as point clouds may be produced. Point clouds are simply large lists containing coordinates for points in 3-D space that lie on the surfaces of the object. Such files are increasingly used to compare manufactured items to their initial designs in Computer Assisted Design (CAD) programs, or input as an object's geometry to be meshed for CFD simulation. It should be noted that the image reconstruction procedures for this type of 3-D modeling are the same as for 2-D CT slices, whereas when a cone-beam X-ray source is paired with an area detector to produce volumetric CT data, an entirely different reconstruction algorithm is required.

Once 3-D models have been visualized from CT slices, surfaces may be extracted for further analysis, including surface area and volume. Unfortunately, the process of obtaining the data is very lengthy, particular when subpositions are required. Obviously when considering a flow system, the time required to image the device is of importance. Currently, this technique represents a time average with each slice taking roughly 50 seconds. Cone beam X-ray sources paired with large-area flat panel detectors can significantly reduce the time required, as one rotation of the object will produce an entire set of volumetric data. However, that technology is still being developed for high X-ray energy applications.

Very small spacing is required for high-resolution models. Slice spacings of 0.10 and 0.15 inches were used in this work. This resulted in a scan time of approximately 10 hours to model a 6-inch tall section of the air-water column. Experience using this technology has led GE to suggest using cubic voxels; the pixel size specified in the 2-D CT slices should be equal to the slice spacing used. The 3-D modeling performed in this study used only the GE scanner, although the 3DID scanner is also capable of this technique.

3.7 Calculations Applied to Air-Water X-ray CT Data

The analysis of the X-ray CT images obtained for the air-water contactor focuses on identifying the material present in the image pixels. Rather than using X-ray transmission data to perform calculations as done by Schmit [56], the actual reconstructed CT images were used. While using images introduces the need to identify small regions of liquid in order to determine the total amount in the column, it reduces the number of base scans needed to characterize the data. Only the completely dry and flow cases need to be considered since the parameters are calculated directly from images rather than being scaled between the minimum water case (dry) and maximum water case (flooded). In addition to determination of liquid holdup, CT images allow visual inspection of the liquid distribution in the column. Two columns may exhibit identical liquid holdup, even on the local scale, yet performance of the devices can be drastically different depending on how the liquid is distributed in the column. All image processing was performed using IDL and Adobe Photoshop.

3.7.1 Liquid Holdup and Void Fraction from CT Slices

The liquid holdup is defined for vapor-liquid contacting processes as the volume of liquid per volume of packed bed. Tomographic slices can be viewed as pseudo-volumes since they have a finite thickness, or a two-dimensional analogy to holdup can be derived where the number of pixels that represent water is divided by the total number of pixels that represent the column cross-section. This method automatically provides correction for the packing void fraction.

The main processing technique applied to the calculation of void fraction and liquid holdup from CT data is image subtraction. The characteristic grayscale of water is very close to that of the edges of the metal packing, making it difficult to determine which material is actually represented. Thus, quantitative analysis using only flow images is difficult. When one image is subtracted from another, the grayscales of corresponding pixels in each image are subtracted, with the difference being assigned to a pixel at the same location in a new image. All three images should be of identical dimension and use the same color map scaling. Using this process, features that appear identical in two processed images will disappear in the resulting image. This allows analysis of features in an image that may vary from one experiment to the next, such as the location or thickness of a liquid film on the surface of structured packing.

Application of image subtraction to the air-water column involves subtracting the CT image at a specified elevation obtained under zero flow from a CT image at the same elevation taken under flow conditions. Assuming the column has not moved and the manipulator can return to the same physical location accurately, the image that results from the subtraction will not show the column or any internal features other than the flow.

Several factors can negatively affect the image subtraction process. It is particularly sensitive to image artifacts including beam hardening, which typically vary greatly from one image to the next. Unless the artifacts are identical in all images, artifacts will also appear in the difference image. To fully understand how subtractions can be affected, it is necessary to address some issues specific to the imaging process.

While the grayscale of a pixel is determined by the attenuation coefficient of the material represented by that pixel, several factors can influence the actual value assigned to a pixel. One cause of variation in grayscale, even for a uniform object, is the blurring effect inherent to X-ray CT. This is a result of a limited number of source-detector paths available to pass through a given point in the object. The physical measurement of this phenomenon is the focal spot size of the X-ray scanner. A machine with a larger focal spot size will produce images that are blurrier.

Imaging in general is a process that discretizes a continuous domain. Each pixel in an image represents the physical features present in the corresponding region of the object. Therefore, when a region of the object is non-uniform, the pixel represents an average of those features. This is known as the partial-volume effect since features occupy only a portion of the total volume represented by a pixel. To address this issue, each pixel grayscale is typically treated as a linear combination of material attenuation weighted by volume fraction. Interface locations, volume fractions, and feature measurements can all be obtained quite accurately using this technique.

It is common for the interface between phases or materials to occur within the area of a pixel, even at very high resolutions with small pixel sizes. Material boundaries can be blurred due to the resolution limitations of X-ray CT, which can affect the grayscale value of neighboring pixels. This is described by the edge response function, where the grayscale of pixels encountered along a line normal to the interface between

two materials shows a slow transition from one characteristic value to the next rather than a sharp step change. This phenomenon makes differentiation between packing edge pixels and water film pixels difficult, affecting the accuracy of film thickness measurements.

An extension of the partial-volume effect is the fact that X-ray CT represents a time average of the material properties over the course of a scan. When a flow system is imaged, the object is changing with time. Therefore, the pixel grayscales will vary depending on how the flow varied in a given region of the object. Any combination of time-averaging and partial-volume effects can appear in an image. Unfortunately, deciding which phenomenon contributes to the grayscale value assigned to a pixel is difficult. A grayscale value is just a number, and contains no information about how that number was determined.

The CT images of the air-water contactor include partial-volume and time-averaged features. The structured packing is constructed of very thin metal sheets, smaller than the size of a pixel. The corrugated structure also contributes to some partial-volume behavior. When images are subtracted to produce images that only show the liquid at a given elevation, a distribution of grayscales is observed for the water, indicating that many pixels are not completely filled by water. To determine the volume present, it is necessary to have a characteristic value for the grayscale of a pixel completely filled with water.

Even for a uniform object, there is typically a distribution of grayscale values associated with a given material. An image histogram, which displays the number of pixels of a given grayscale value, is very helpful in determining the characteristic grayscale of a given material in an image. Figure 3-13 is an example of an image histogram. The total under the curve of a histogram is equal to the total number of pixels

considered. Histograms may be obtained for entire images or smaller regions of interest within an image. For a homogeneous region in an image, a normal distribution of grayscale values is usually observed. If multiple materials are present in an area, the histogram will have multiple peaks. When materials have similar characteristic grayscale values, the peaks will appear overlapping. The value of performing calibration scans through air prior to scanning the object means that air can be assigned a gray value of zero since it is typically the least-attenuating material present during scans. The system is benchmarked by scanning materials of known composition to determine a characteristic grayscale value for the material. Analysis of the histogram of these calibration images provides the data needed to select the grayscale level most likely associated with a given material. Successive pixels can be divided by this characteristic value to determine the volume fraction of material present in the pixel. Since there is a single characteristic value, error can result where a partial-volume effect is assumed instead of simple blurring. It is advantageous to have the reconstructed image to help determine which phenomena might be occurring.

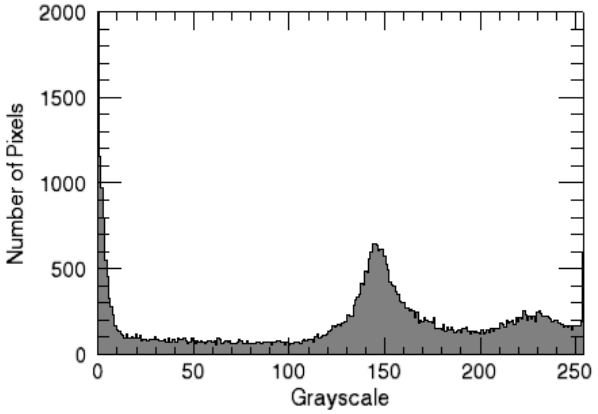

Figure 3-13. Sample image histogram.

Liquid holdup is calculated using the partial-volume technique. Once the dry image has been subtracted from the flow image, an image representing only liquid is obtained. Since the pixel dimensions are known, the total number of pixels representing the column cross-sectional area can be determined using the column's actual area. Image processing algorithms can be written that divide each pixel in an image by a characteristic value. This value can be obtained for water by analyzing the histogram of images where large amounts of water are present, usually in the water outlet line that runs parallel to the column. Normalizing all pixels by the characteristic value for water P_w will provide the volume fraction of water in each pixel. Summing all of the pixel values for water fraction and dividing by the total number of pixels inside the column, A_c, produces the local liquid holdup for a given slice, as expressed in Equation 3-9. The column-average holdup in the packed bed can be determined by averaging the values obtained from equally spaced CT slices taken throughout the packed section. Spatial variation of liquid holdup within a slice is investigated by dividing the column into four quadrants and applying the holdup calculation to a specific section.

The measurement for calculating void fraction from a dry CT slice is similar but does not require a subtraction. A value for a pixel completely filled by packing is selected from the image histogram, and all pixels inside the column are divided by that value, summed, and divided by the total number of pixels in the column to determine the void fraction. Since a pixel full of packing is rare due to the small thickness of the metal sheets, some iteration is required to find a value that produces a void fraction that matches the specification provided by the packing vendor.

[3-9] $$h_L = \frac{\sum_{i=1}^{N} \frac{P_i}{P_w}}{A_c}$$

3.7.2 Area Measurement from 3-D Reconstructions

Three-dimensional models of portions of the packed section can be produced by taking CT slices at consecutive closely spaced intervals. The images can be read into volumetric visualization software as an image stack. The programs used for the models constructed in this work were Amira by Mercury Computer Systems and Volume Graphics' VGStudio Max.

To display the volume, the raw data or images are read in to an array by specifying the image dimensions, size of the header in each file, and the byte ordering. The color map is then adjusted to filter out noise and artifacts and highlight features of interest in the image. Volumetric histograms can be produced for the image stack. However, the primary use of the stack technique is for visualization. For calculations to be performed on the volume, it must be converted to a surface.

Surfacing the image stack involves the creation of many small planes that pass through voxels of a given threshold value. Values higher than the threshold are located on one side of the plane, and values lower on the other side. The threshold is usually chosen to be halfway between the characteristic voxel grayscales for the two phases that are to be separated. Due to the variation in grayscale associated with blurring, partial-volume, and edge response behavior, selection of a threshold value is a trial and error process. Surfacing is a computationally intensive procedure, sometimes requiring the data to be subdivided into smaller volumes with fewer image slices in order to process the data faster.

The imaging programs have built-in procedures for the calculation of surface area. The total area of packing can be calculated by creating a surface from an image stack of dry CT slices. Visualization of the time-average liquid flow can be achieved by reading in an image stack of subtracted images. Film-flow is a steadier phenomenon than rivulet flow and may be more easily resolved. Since the subtracted images contain a large amount of partial-volume pixels, the choice of threshold during surfacing becomes an important issue. Theoretically, the surface area of liquid can be calculated in similar fashion to the packing surface area. The liquid can also be assigned a different color map than the dry packing to help distinguish areas that contain liquid.

3.7.3 Line Profiles

When visualizing a CT slice, the software packages used allow profiles of grayscale to be extracted along lines drawn on the image itself. By clicking and dragging to form a line, a plot will display that shows the grayscale values along the line. The technique is valuable for locating and defining interfaces as well as performing measurements on features of interest in the images. The difference in line profiles normal to the packing surface for flow and no flow conditions is very small, making it difficult to measure the apparent film thickness on the packing.

3.8 Traditional Experimental Techniques

Experimental measurement of liquid holdup in the air-water contactor was conducted by traditional techniques for comparison to the values obtained using X-ray CT imaging. The procedure has been widely used for air-water systems to measure the volume of liquid retained in a packed bed during hydraulic testing of column internals. The column is first allowed to reach steady state for a given set of liquid and vapor flow

rates. The fluid flows to and from the column are then simultaneous stopped. The volume of liquid that drains from the bed is then measured to determine the column-average holdup.

This procedure was applied to the 6-inch air-water contactor containing Mellapak 250Y structured packing. Flow rates for both air and water were identical to those used in the imaging studies. Due to the unique design of the column, the liquid holdup of the packed bed had to be corrected to account for holdup in the liquid distributor. Equation 3-10 was used to determine the average liquid holdup, where V_W is the volume of water drained, V_D is the volume of the liquid holdup in the distributor, and V_{PB} is the total volume of the packed bed.

[3-10] $$h = \frac{V_W - V_D}{V_{PB}}$$

3.9 Pilot Plant Equipment and Procedures

Data for liquid holdup and fractional area obtained via X-ray CT was compared to experimental measurements of the same parameters for Sulzer Mellapak 250Y collected from the Separations Research Program's (SRP) pilot plant equipment. Located at The University of Texas' J.J. Pickle Research Campus in Austin, Texas, SRP features an 42.8-cm inner diameter air-water column used for hydraulic testing of both random and structured packings, as well as trays. The column, shown in Figure 3-14, is also equipped to perform mass-transfer measurement, particularly in the area of CO_2 scrubbing. The system is equipped with a Delta-V distributed control system from Fisher-Rosemount. The packed bed height was 114 inches for the holdup and effective area experiments.

Liquid holdup is measured for the pilot plant air-water column in much the same way it is measured for the 6-inch air-water column used for the imaging experiments. A 350-gallon tank is located at the base of the column. A liquid level is held in this tank while water is circulated back to the top of the column. Flows to the column are shut off, and the level change associated with liquid draining from the bed is used to calculate the volume of water that drains, which in turn is used to calculate holdup. Corrections accounting for holdup in the liquid distributor and evaporation in the sump are also applied.

Figure 3-14. SRP air-water column used for experimental liquid holdup and interfacial area data acquisition.

The procedure for determining fractional area using the air-water column involves mass transfer measurement of the absorption of carbon dioxide into a dilute aqueous solution of sodium hydroxide as described by Pohorecki and Moniuk [46]. Equation 3-11 gives the second-order reaction that occurs.

[3-11] $$CO_2 + 2OH^- \rightarrow CO_3^{2-} + H_2O$$

Using a modified two-film theory, a correction can be applied to the liquid phase mass transfer coefficient to account for the chemical reaction. The key assumption of the technique is that the gas phase resistance is negligible. In general, at high gas velocities and for low concentrations of sodium hydroxide, the liquid phase resistance will dominate. For an irreversible, pseudo first order reaction, the expression for the overall gas phase mass transfer coefficient/area combined term $K_{OG}a$ is given by Equation 3-12, where D_{CO2} is the carbon dioxide diffusion coefficient, C_{OH-} is the concentration of hydroxide ion, k_r is the reaction rate constant, and H is the Henry's law coefficient [64]. Solving for gas/liquid contact area, a, results in Equation 3-13. A detailed derivation of the calculation procedure is provided as Appendix A.

[3-12] $$\frac{1}{K_{OG}a} = \frac{1}{k_G a} + \frac{H}{a\sqrt{D_{CO_2} C_{OH^-} k_r}}$$

[3-13] $$a = \frac{HK_{OG}a}{\sqrt{D_{CO_2} C_{OH^-} k_r}}$$

The experiments are carried out in the SRP pilot plant air-water column. Carbon dioxide is scrubbed from ambient air using a 0.1 N sodium hydroxide solution. Liquid is recycled from the sump back into the top of the column via a centrifugal pump. A 40 HP blower provides the airflow. A carbon dioxide analyzer measures the CO_2 concentration in the ambient inlet air and in the air outlet stream at the top of the column, from which $K_{OG}a$ can be calculated. Continuous online monitoring of CO_2 concentration allows calculation of the mass transfer efficiency during operation.

CHAPTER 4: EXPERIMENTAL RESULTS AND DISCUSSION

The application of X-ray computed tomography to an operating air-water contactor resulted in data that can be classified into four categories. Initially, CT slices of the packed section were obtained under both dry and flow conditions to measure the local void fraction of the packing and the local liquid holdup. Extending the data acquisition to include a series of closely spaced slices resulted in a data set that could be reconstructed and visualized in three dimensions. Using image processing techniques, the 3-D slices were used to determine isosurfaces for both dry packing and liquid flow. Surface area was measured from the isosurfaces in an attempt to quantify the gas-liquid contact area. Finally, stationary transmission measurements were performed to evaluate the stability of liquid flow and measurement noise associated with the X-ray scanners. The results of these studies will be presented in the following sections.

4.1 CT Studies Using 3DID Scanner

A series of CT experiments were performed using the 3DID scanner for Mellapak 500Y and 250Y structured packing. Initially, a radiogram is obtained to determine the CT scan planes of interest. A radiogram for Mellapak 500Y half-elements is shown in Figure 4-1. The flange that connects the packed section of the column to the section that contains the liquid distributor and mist eliminator can be seen at the top of the image. The four steel support rods appear very bright in the image due to their large attenuation of X-rays. Clearly, four packing elements can be identified in the column. Elements 1 and 3 appear differently than elements 2 and 4 because they have been installed at 90^{o} angles. Bright regions appear in the middle of each element where the wiper band is

located. In general, the packing elements appear very dense. Increased void space is apparent in the region of the interface between two elements.

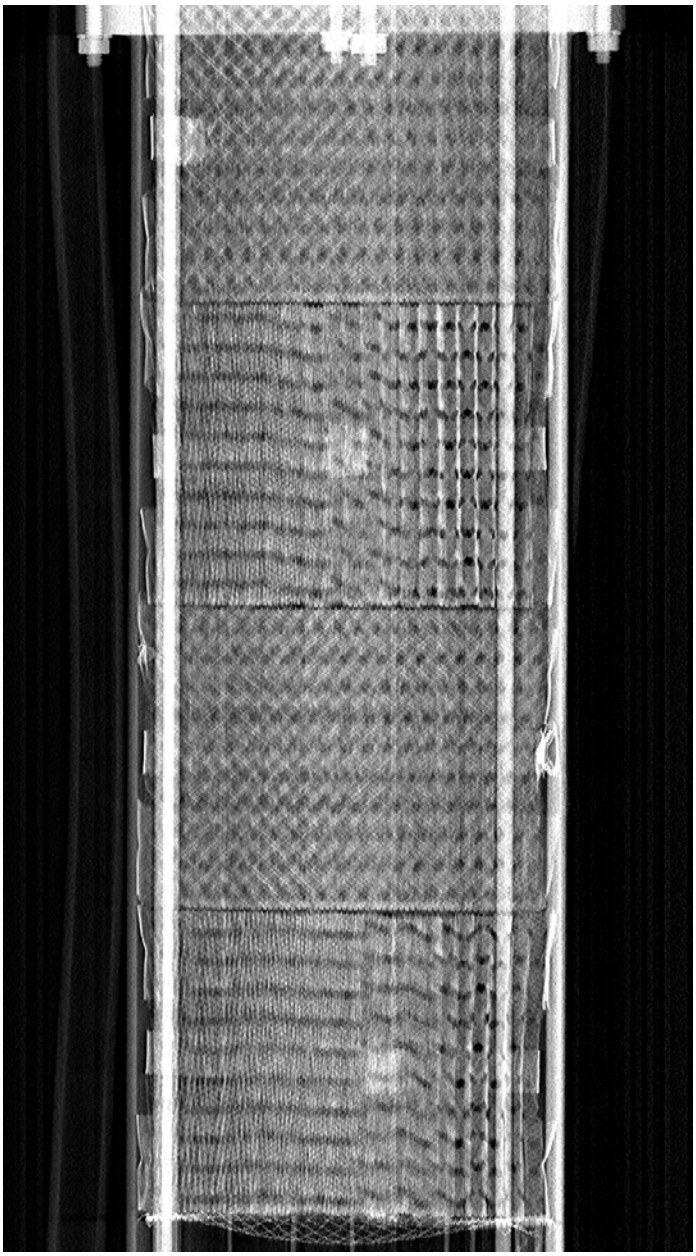

Figure 4-1. Radiogram of Mellapak 500Y half-elements from 3DID scanner.

A total of nine scan planes were identified for analysis. The scan planes included the bulk packing region as well as the middle and lower packing element joint. The column was initially scanned under zero flow. The column was then filled with water and scanned at the lowest four elevations. The flooded scans were limited by the weight capacity of the scanner turntable. Finally, a series of scans were performed while vapor and liquid flows were applied to the column.

The materials present within the walls of the air-water contactor during the scans were air, water, and stainless steel. Figure 4-2 is presented to identify the features present in a typical CT slice of a packed column. The image was taken approximately 0.3 inches from the middle packing joint after the column had been leak tested. Indicated by region marked 1, the gray circle in the image represents the column wall. The four stainless steel support rods appear as bright white circles around the perimeter of the column, marked as region 2. Beam hardening artifacts are noticeable in the air region around each support rod. The air inlet and water outlet lines also appear as gray circles, shown as region 3 in the upper right corner of the image. For the dry scans, the tubes are both filled with air. During the flow scans, one tube will contain water. The metal packing sheets appear as bright wavy lines in the middle of the image. Region 4 shows an area where the packing sheets are continuous. However, at some elevations the perforations in the packing sheets are visible in the CT images, as shown by region 5. Perforations appear as discontinuities in the packing sheets. It is evident that the sheets in the middle of the element represented in this image are not very well aligned in the area to the right and below region 5. The bright region denoted by 6 around the perimeter of the packing is the metal wiper band. Overlaps and discontinuities in the wiper band show the regions where the band has been cut to be bent down before installing the element. Finally, water in the column is highlighted in region 7. Although no liquid was circulating through the

column during the scan, flow had been applied during the leak test. The water regions present in Figure 4-2 are defined as static holdup, or liquid that does not drain from the bed.

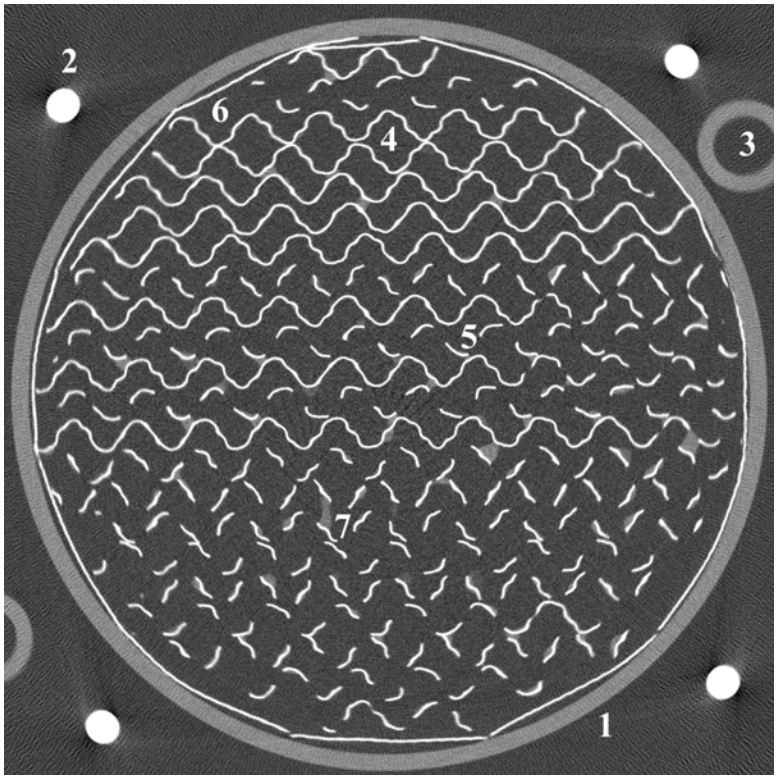

Figure 4-2. Representative CT image of dry structured packing.

A series of images representing the dry, flood, and flow cases is shown in Figure 4-3 for a scan plan elevation of 339.7 mm (13.37 in.) above the turntable surface. In the flooded scan, the column is completely filled with water. Thus, the grayscale of the void space increases accordingly. The grayscale values of the water regions appear similar to those of the column wall. On the right, the flow image is shown for a liquid rate of 10.5

GPM/ft^2 and a vapor F-factor of 0.27. The water outlet tube now contains liquid. An increased amount of liquid is observed between the packing sheets.

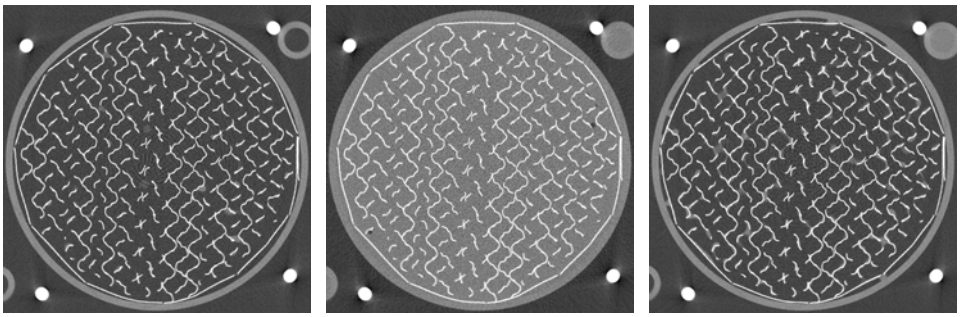

Figure 4-3. CT images for three conditions at an elevation of 339.7 mm. From left, dry, flooded, and flow.

In the flow image, circular artifacts have become more pronounced within the column region. These ring-shaped streaks appear as a result of the density profile within the scan plane changing over time due to flow variation, and are not representative of the physical reality of the column interior. The artifacts make the image blurry, complicating analysis. A sample flow scan is shown in greater detail in Figure 4-4.

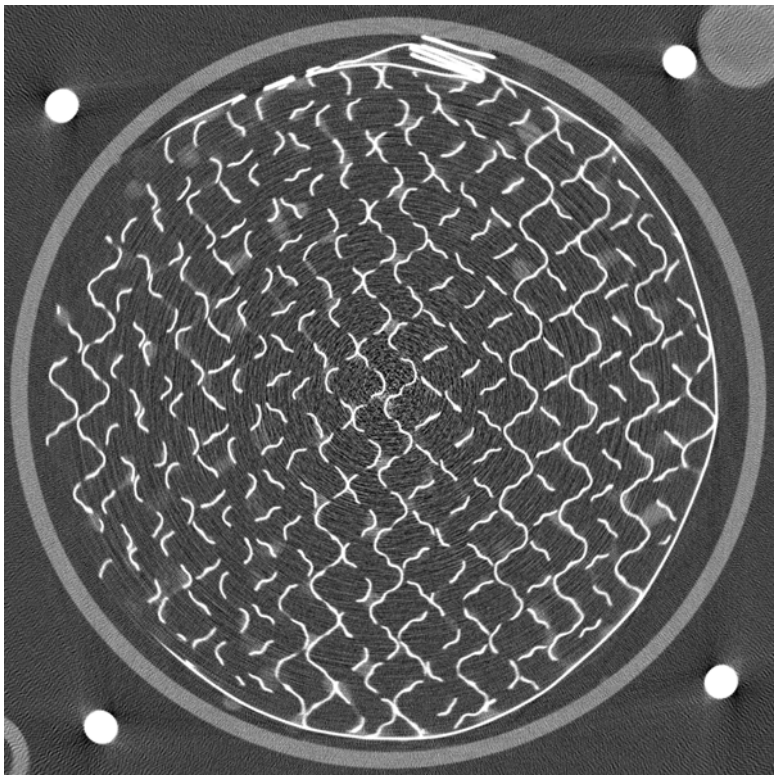

Figure 4-4. Image of Mellapak 500Y under flow conditions. Liquid rate is 10.5 GPM/ft^2 and vapor F-factor is 0.14.

The liquid flow pattern observed in the images of Mellapak 500Y appears to favor rivulet flow. The liquid is present in large amorphous-shaped areas, rather than as a film on the surface of the packing. One suggested explanation for this behavior is the combination of small flow channels and a high surface tension fluid. Water has a surface tension of 72 dyne/cm, whereas most hydrocarbons are in the range of 20 to 25 dyne/cm. A lower surface tension fluid will be more likely to spread out into a film on the packing surfaces. However, a high surface tension fluid like water that exhibits a high contact angle when applied to metal packing will tend to accumulate, particularly in the troughs of the corrugations and at the contact points between adjacent sheets. The liquid flow pattern may be examined more clearly by subtracting the dry image at a given elevation

from the flow image at that same elevation, causing material in similar locations between the two images to cancel out, leaving only the liquid. An example of image subtraction is shown in Figure 4-5.

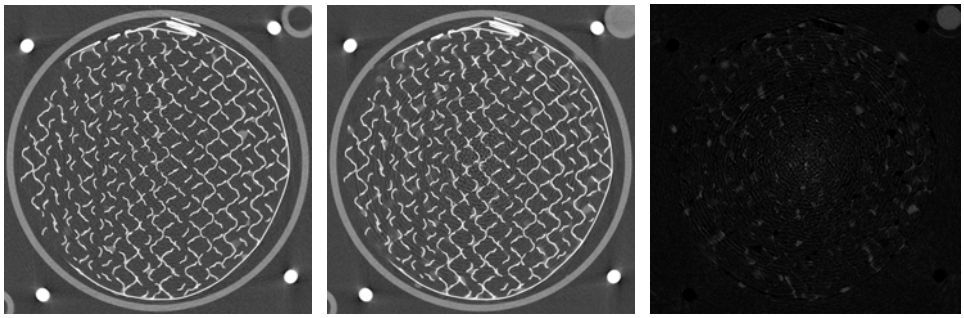

Figure 4-5. Example of procedure for subtracting images. From left, dry scan at 350.0 mm, flow scan at same elevation (L=10.5 GPM/ft^2, V=1.3F), and image resulting from subtraction.

The subtracted image shows the differences between the two source images. Regions of water can be identified in the subtraction by comparing the areas to the corresponding location in the flow image. However, a large amount of artifacts appear present in the dry image, and they are of a similar grayscale as water. These artifacts would be counted as pixels containing water during holdup calculations as described in Chapter 3. Thus, the holdup values would be artificially higher than the true value for a given slice. It is necessary to reduce or eliminate artifacts for accurate image analysis. Additionally, the presence of static holdup in the dry image affects the subtraction process. Liquid that should be identified from the flow scan will be cancelled out if the liquid was present in the same form as static holdup. Therefore, it is crucial for the dry scan of the column to be completely void of liquid.

The interface between two packing elements has received much attention as a potential area for improvement of structured packing. To evaluate the behavior of the joints during column operation, a series of CT slices was taken in the packing element joint region. An example of a flow scan taken at the interface between two elements is shown in Figure 4-6. The liquid flow rate was 10.5 GPM/ft^2 and the vapor flow rate was an F-factor of 0.27. The appearance of the column interior is drastically different than that seen in slices taken in the middle of a packing element. The packing sheets appear oriented in both directions, indicating that sheets from one element are at the same height as sheets from the element above. The void space is increased. Since the packing elements are separate and often vary in size and shape due to manufacturing tolerances, it is difficult to ensure a tight fit across the entire column cross-section during installation.

A large accumulation of liquid is present in the slice. As liquid drains from one element into the next, it is forced to change direction. This bottlenecking causes the liquid to spread out in the small void space between the two packing elements. As a result, the vapor flow path often must change as well. This behavior results in the interface between packing elements serving as the trigger point for column flooding.

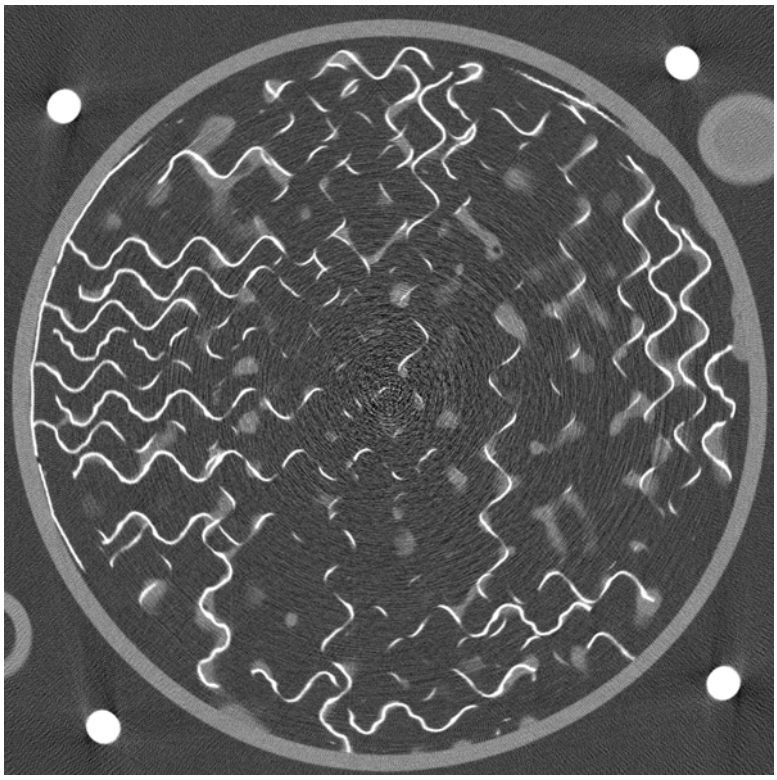

Figure 4-6. CT image of packing element joint. Liquid rate is 10.5 GPM/ft^2 and vapor F-factor is 0.27.

Mellapak 250Y was installed in the air-water contactor in an attempt to improve the liquid flow pattern. It is a less dense packing than 500Y with longer corrugation lengths, resulting in larger channels for vapor flow and decreased proximity between adjacent sheets. The radiogram of the packing as installed in the column is shown in Figure 4-7. The elements are twice the height of the previously installed 500Y half-elements; therefore only two elements were installed to keep the packed bed height constant. Each 250Y element contains two wiper bands, visible at the top and bottom of each element in the radiogram. The air inlet and water outlet hoses are visible in the column interior, as they happened to be oriented in line with the X-ray paths through the column. The characteristic pattern of the elements appears less dense than the 500Y

packing. As with all packing, the elements were installed with a 90^{o} rotation between adjacent layers.

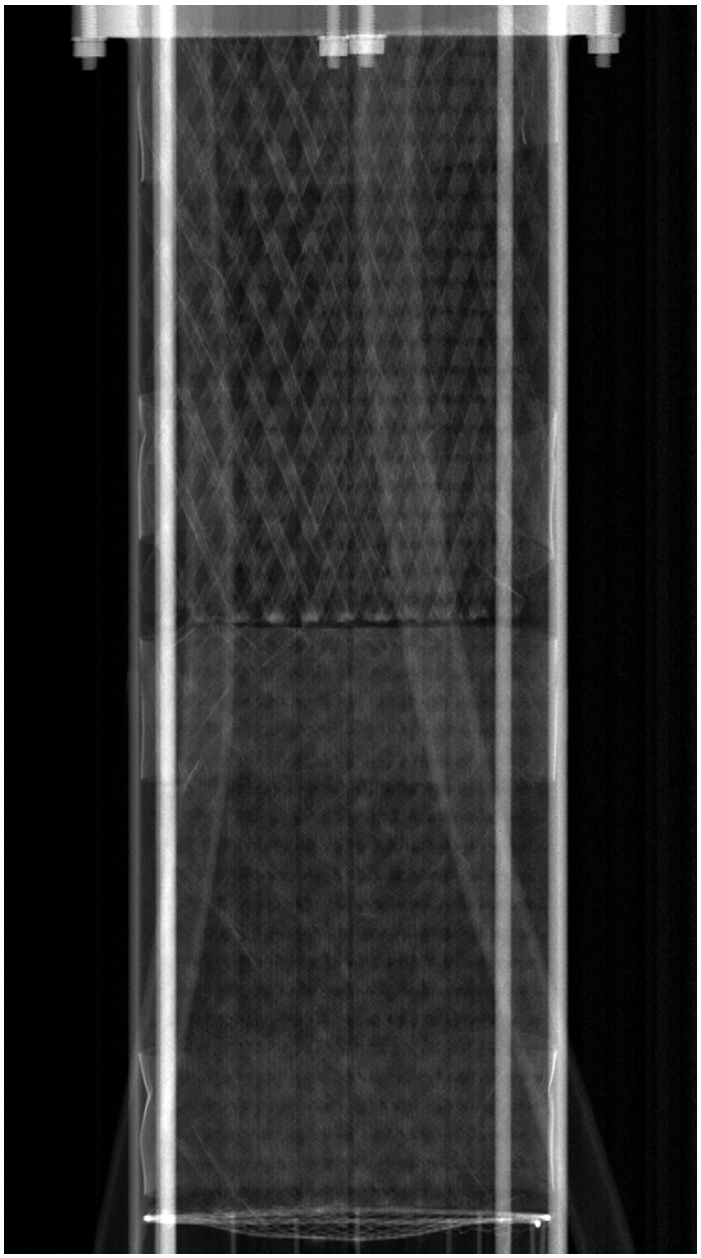

Figure 4-7. Radiogram of Mellapak 250Y using 3DID scanner.

The dry and flooded slices for 250Y at an elevation of 356.0 mm, shown in Figure 4-8, detail the distinct difference in flow area available to vapor and liquid when compared to the 500Y packing. Circular artifacts are much more apparent in these images than in comparable images for 500Y, even when no flow is applied to the column. The resolution of the images appears better, with the surface texturing present on the metal surfaces appearing in the reconstructed images. The wiper band is present around the entire circumference of the element at this elevation. The bright region in the center of the dry image shows a small amount of static holdup present at the contact point of adjacent packing sheets. The overall amount of static holdup observed in the image is significantly less than the dry images of 500Y packing. This suggests that the high surface tension of water, combined with the small, cramped flow paths of the dense 500Y packing lead to a greater retention of water within the bed after flows are stopped. The more open 250Y allows the liquid to drain more easily. Some small dark regions are visible in the flooded scan, indicative of air bubbles trapped in the packed bed.

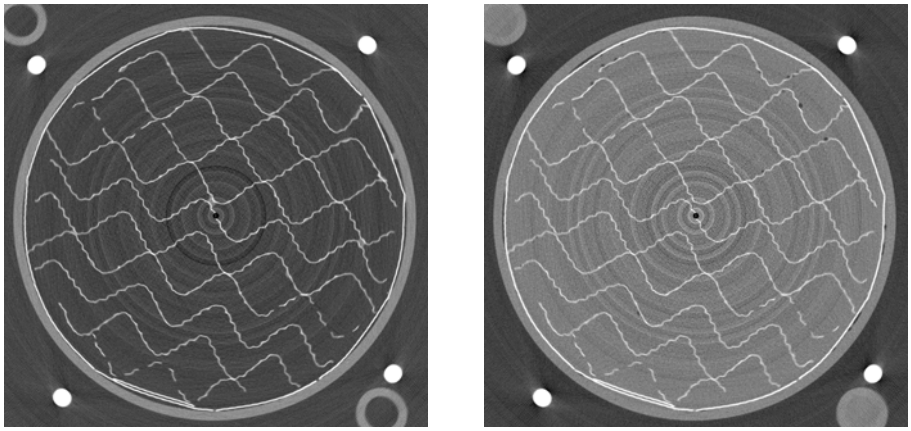

Figure 4-8. Dry (left) and flooded (right) CT images of Mellapak 250Y from 3DID scanner.

Ring-like artifacts are compounded by the fact that flow is occurring in the column, where the data that is to be reconstructed is constantly changing with time. Such artifacts are also present in the 250Y flow images, as seen in Figure 4-9, where identical sections of a dry image and flow image are detailed. The artifacts are streakier in the flow image, and appear as a grayscale similar to water. Regardless of the cause, these artifacts significantly affect the analysis procedures.

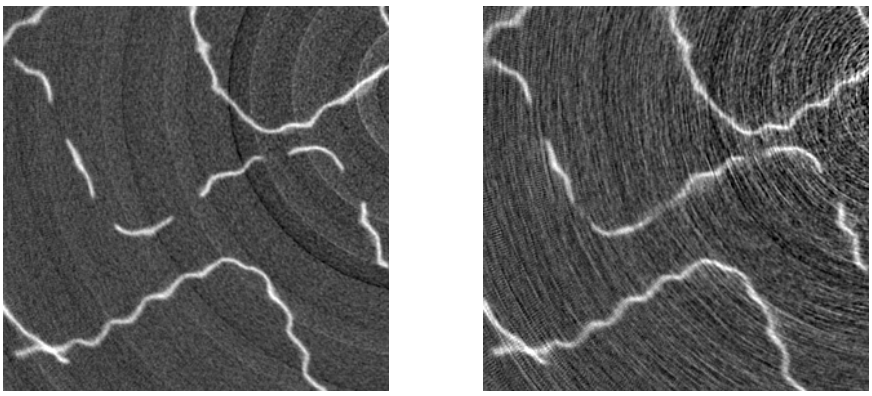

Figure 4-9. Comparison of artifacts in Mellapak 250Y dry image (left) and flow image (right). Liquid rate is 15 GPM/ft^2 and vapor F-factor is 0.27.

In addition to the different styles of artifacts, the zoomed images shown in Figure 4-9 also provide insight as to the liquid flow pattern. Large regions of water do not appear between the packing sheets in this subset, but rather the packing surface itself appears fuzzy compared to the packing surfaces in the dry image. Also, near the center of the image liquid appears to be covering the perforation. The presence of gray pixels in the flow image at this location means that liquid was flowing in that portion of the packing for some period of time during the scan.

An example of a subtraction image for 250Y is presented in Figure 4-10. The liquid regions are more organized than those observed in the 500Y subtraction image. The liquid appears to orient along the same geometrical pattern as the structured packing sheets, indicating that film flow is the pattern likely occurring. Liquid also collects at the contact points between adjacent sheets. However, in this image more wall flow is noticeable, particularly around the packing wiper band in the lower left and upper right portions of the image. For a 6-inch column, 250Y packing is approaching the limit of the least dense packing that vendors suggest using. Otherwise, wall effects become increasingly important to consider. Image artifacts continue to be present near the center of the column in the subtracted image.

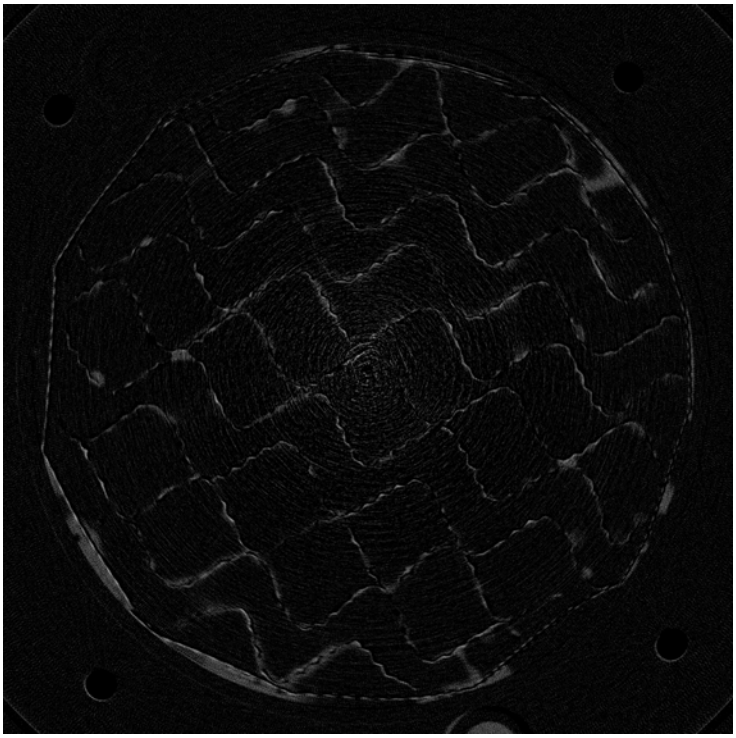

Figure 4-10. Mellapak 250Y subtraction image for L = 15 GPM/ft^2 and V = 0.27 F.

The subtraction technique is very sensitive to movement that occurs between the two scans used for the procedure. As a result, small movements of the column can cause the images to be slightly shifted. When two such images are subtracted, crescent-shaped shadow regions commonly appear. Such a phenomenon is visible for the column support rod in the lower left corner of Figure 4-10, and also for the water outlet line.

Figure 4-11 shows the performance of Mellapak 250Y at the interface between packing elements. The void space at this particular joint is quite high, although packing sheets from both elements oriented orthogonally are visible. Liquid films draining from one element, generally oriented from bottom to top, are maintaining their structure as they enter the lower element, which is oriented from left to right. Liquid branching across adjacent sheets is present. The liquid is not as prevalent in the flow channels as was observed for the 500Y packing. As with other images from the 3DID scanner, flow artifacts are present. The presence of artifacts restricts the available methods for analysis and introduces error into calculations for liquid holdup from CT images. Therefore, a true third-generation scanner operated by General Electric was chosen for further imaging studies.

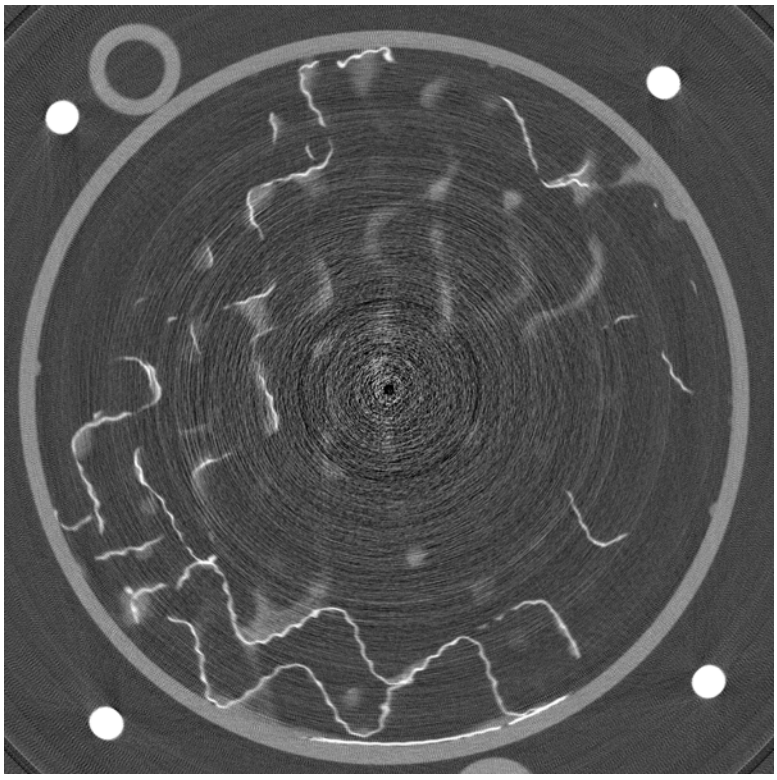

Figure 4-11. CT image of Mellapak 250Y at joint under liquid flow of 15 GPM/ft^2 and F-factor of 0.2.

4.2 CT Slices Using GE Scanner

After the flow system was modified as discussed in Chapter 3, experiments were conducted using an Industrial Computed Tomography scanner located in Cincinnati, Ohio. Four trips were made to image the column. The first experiments carried out were similar to those performed with the 3DID scanner. The maximum airflow rate was increased to an F-factor of 0.48. The experiments began by imaging the packed section of the column at 1" intervals while dry for a total of 16 slices. An example of a dry image is shown in Figure 4-12.

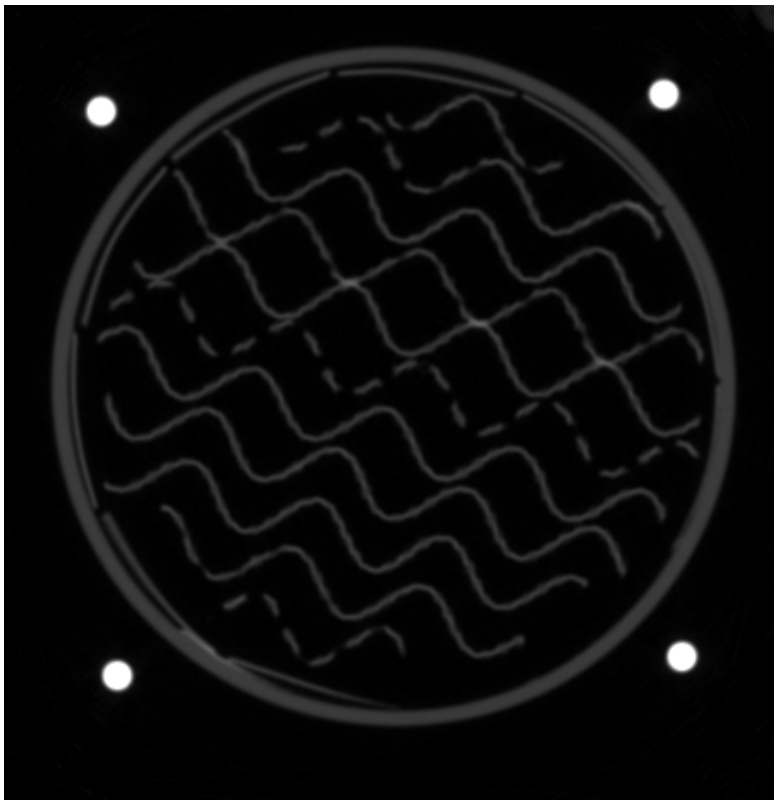

Figure 4-12. Sample dry CT image of Mellapak 250Y using GE scanner.

The contrast of the image, specifically of the air region, is greatly improved over the images obtained with the 3DID scanner. Although no flow is present, there is much less noise, and no artifacts appear anywhere in the image. The edges of the metal support rods are very distinct. At this elevation, perforations are apparent on several of the corrugated sheets. The wiper bend around the perimeter of the packing is also present. The contact points between adjacent sheets appear brighter in this image due to static holdup. The column was leak-tested and allowed to dry prior to acquiring the dry scan data.

As with the 3DID scans, the column was then filled with water to observe the grayscale variation that could be expected during flow scans. Such an image is shown in

Figure 4-13. A small amount of artifacts are present in the image, but they are still more muted than those observed in the 3DID images. The center of the artifact is located at the center of rotation of the scanner turntable, and the intensity of the concentric rings dies off as the rings approach the column wall. The grayscale value of water is again similar to that of the column wall, but the two phases can be differentiated visually. The overall grayscale intensity of the packing appears lighter in the flooded image due to the partial volume effect. The regions around the thin metal packing now contain water rather than air. The combined volume fractions of water and metal are considered for those pixels when reconstructing the image. As water attenuates the X-rays more than air, the pixels representing packing regions in the image appear brighter.

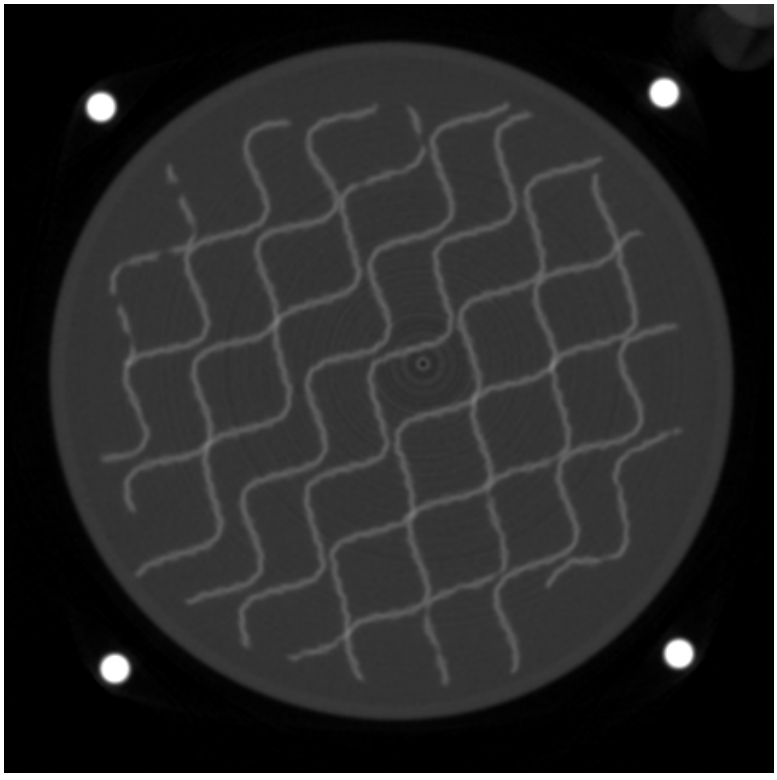

Figure 4-13. Flooded CT image from GE scanner.

The column was then operated at several liquid and vapor rates while CT images were acquired for 16 slices in the packed region. Figure 4-14 shows a flow image where a liquid rate of 15 GPM/ft^2 and a vapor F-factor of 0.27 was applied. Artifacts do not dominate the image as they did with the previous scanner. The image represents a very distinct picture of the location of liquid, which can easily be identified on the surface of the packing sheets. Liquid does not appear in the flow channels, but some regions of water are present near the column wall.

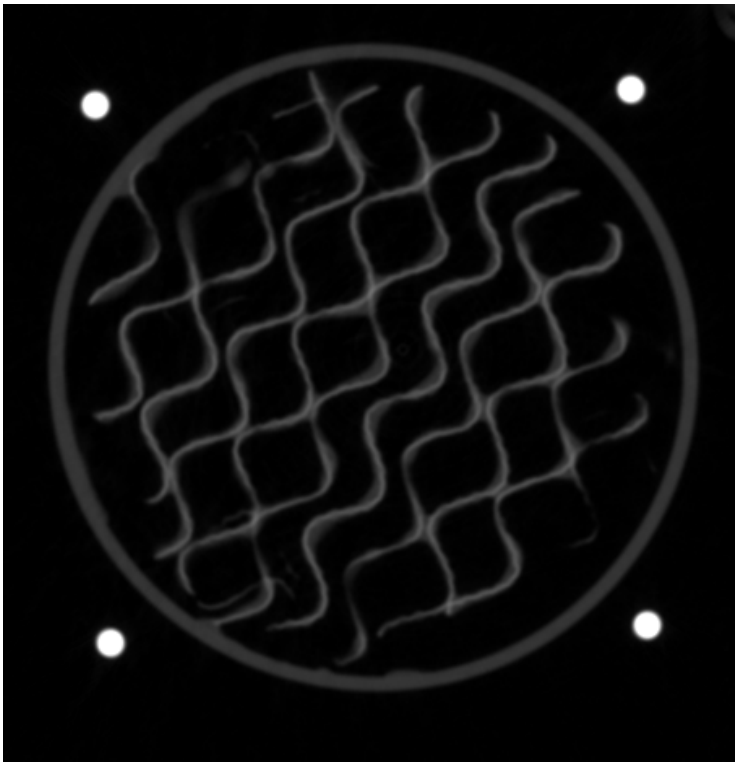

Figure 4-14. CT image of flow taken with GE scanner. Liquid rate is 15 GPM/ft^2 and vapor F-factor is 0.27.

Figure 4-15 details the liquid films on the packing surface. The image grayscales have been adjusted to highlight the features. At this relatively high liquid rate, a large

amount of water should be detectable throughout the packed section. Since the flow channels continue to remain as dark as they were in the dry images, it can be reasoned that the liquid flows as a film on the surface of the corrugated sheets. Regions of moderately light pixels appear on either side of the packing sheets. A well-defined meniscus is visible in the troughs of the corrugations, and liquid is observed to spread from one sheet to another at the contact points. The high surface tension of water is likely contributing to these phenomena. In the extreme of this case, potential area for mass transfer is being lost as the films are "pulled up" off the packing by surface tension forces.

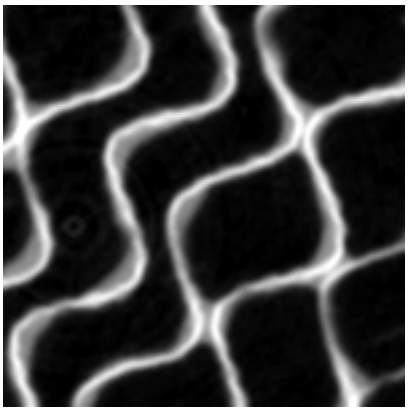

Figure 4-15. Water films on surface of Mellapak 250Y. Liquid rate is 15 GPM/ft^2 and vapor F-factor is 0.27.

Since artifacts were greatly reduced for the images obtained using the GE scanner, it was expected that the image subtractions would more clearly show the differences between dry CT slices and slices obtained under vapor and liquid flow. The pixels in the subtracted images using GE scanner data could be more definitively classified as being air, water, or a combination of the two phases. No longer was it necessary to determine whether a given pixel represented physical reality or artifact. An

example of a subtracted image based on GE scanner data is shown in Figure 4-16. The liquid flow applied was 15 GPM/ft^2, and the vapor F-factor was 1.3.

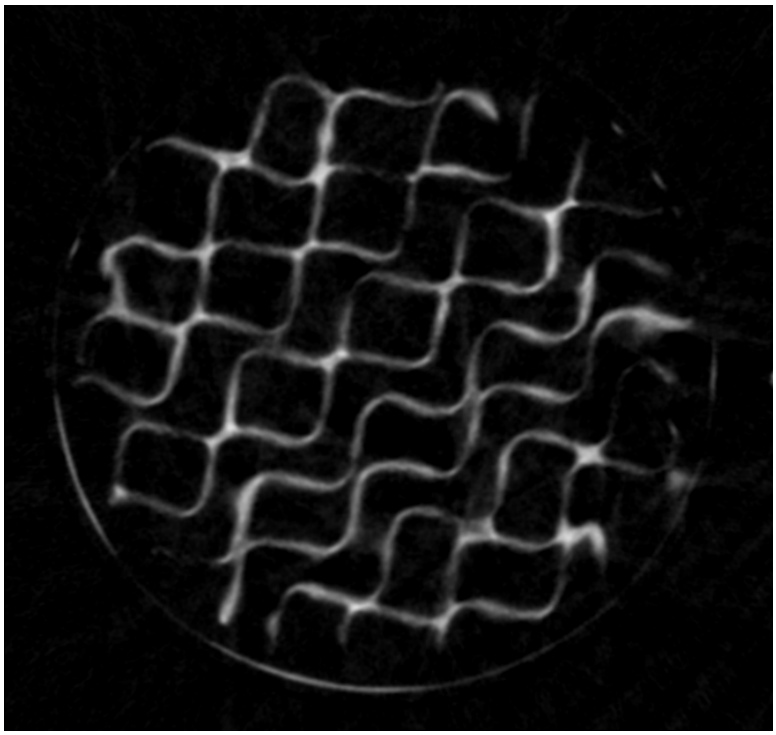

Figure 4-16. Subtraction image from GE scanner data. Liquid rate is 15 GPM/ft^2 and vapor F-factor is 1.3.

The subtraction image clearly shows that the liquid flows as films on the surface of the packing sheets. Near the right side of the column, there is some flow off the packing sheets into the flow channels. Liquid branching near packing contact points is evident. The films appear to be thickest near the contact points. Some wall flow is visible in the lower-left portion of the column. Bright regions in the image exist where water was flowing for a long period during the scan. Lighter colored regions define locations where the liquid flowed for only a portion of the scan or pixels where the liquid volume was small. Although the image is a time-averaged representation of the flow, it

provides some insight about the preferred flow pattern for the liquid under the flow conditions specified. Differences in film thickness and surface coverage can be seen in Figure 4-17, where subtractions of 2.2 GPM/ft^2 and 15 GPM/ft^2 are shown side by side. The air rate was an F-factor of 1.0.

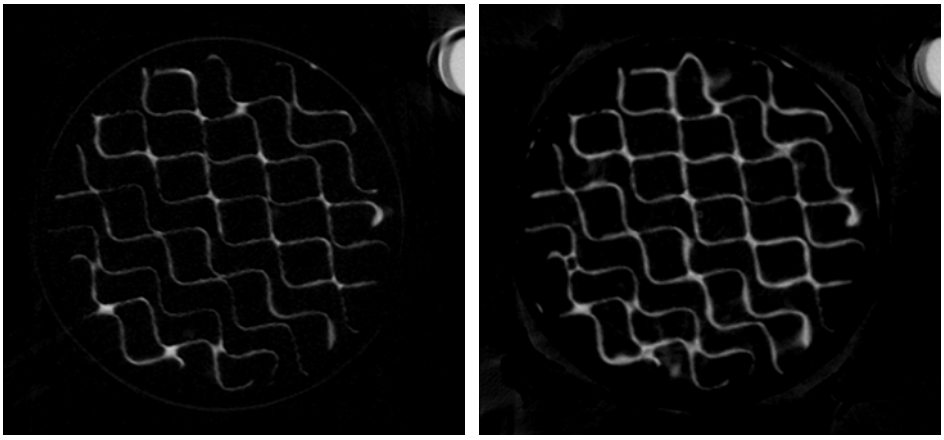

Figure 4-17. Difference images for liquid flows of 2.2 GPM/ft^2 (left) and 15 GPM/ft^2 (right) at an F-factor of 1.0.

The area around the packing joint was also investigated using the GE scanner. Based on the results from the 3DID CT studies that showed increased liquid presence at and above the interface between two elements, a wider range with more slices was used to image the joint area. Over the course of the GE scans between 8 and 19 slices were taken around each of the three packing joints for a variety of flow rates, covering a total height range of 0.25 to 1 inch, centered at the interface. Figure 4-18 shows the flow progression at the interface between packing elements 2 and 3 for a liquid rate of 15 GPM/ft^2 and a vapor F-factor of 1.0. The spacing between images is 0.05 inches, with a total height of 0.75 inches shown.

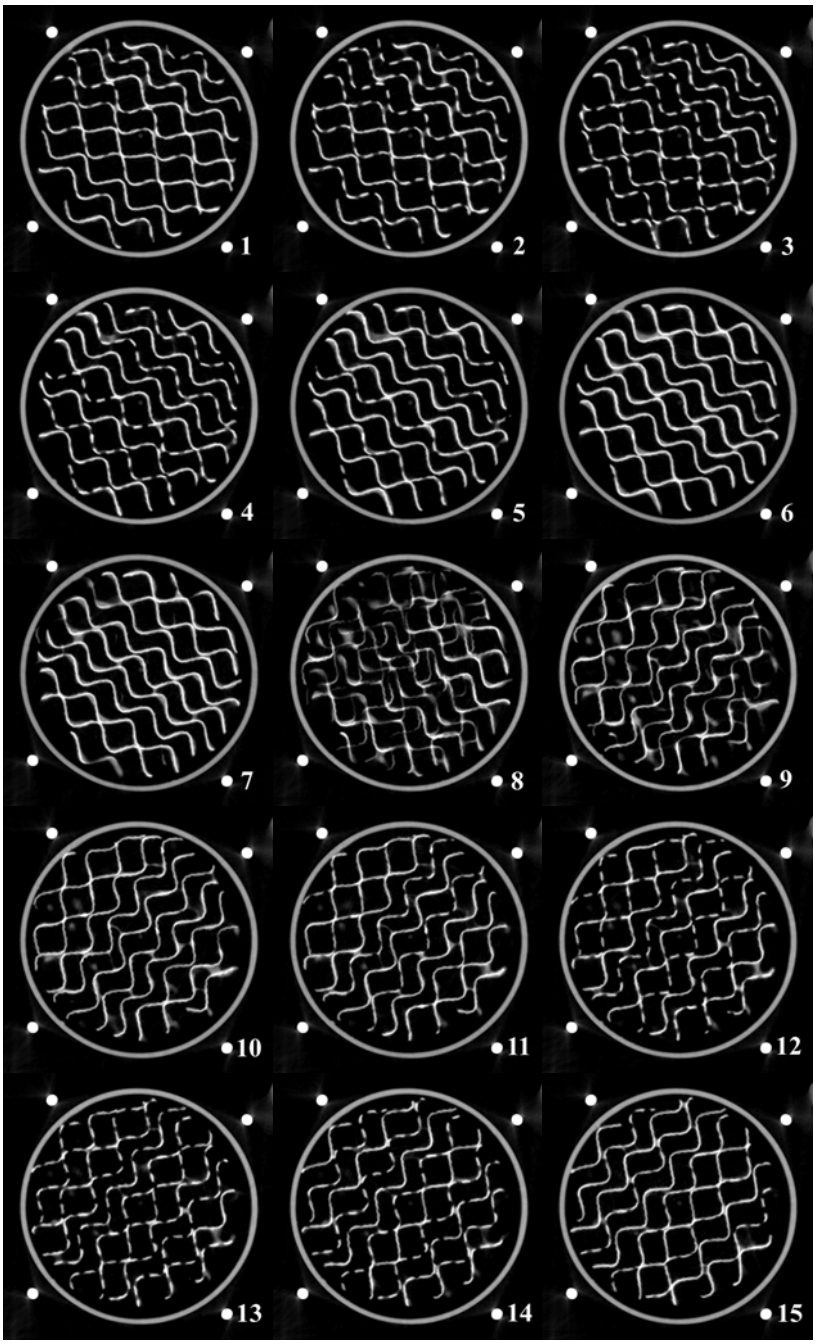

Figure 4-18. Sequential CT images depicting flow behavior at the joint between adjacent structured packing elements. The elevation change between slices is -0.05 inches. Liquid rate is 15 GPM/ft^2 and vapor F-factor is 1.0. Slice 1 elevation is 19.27 inches.

The images progress from top to bottom in the column as they are viewed from left to right and top to bottom. The eighth image in the series is located at the packing interface itself. Images 1 through 3 appear very similar to a normal slice under flow conditions. Beginning with image 4, liquid is shown to accumulate, starting in the upper-left portion of the image. The liquid films in images 5 through 7 appear much thicker than in the images taken higher up in the element. In image 8, taken at the interface, a large amount of liquid can be seen. Packing sheets oriented in both directions can be seen at this elevation. Liquid draining from the upper element can be seen falling into the space between sheets in the bottom element. The area available for liquid flow at this elevation is significantly lower than in other slices. This supports claims that flooding is most likely to start in the packing joint region. Images 9 through 11 also show liquid in the void space between sheets in addition to liquid films on a limited portion of the packing surface. From image 12 through 15 the majority of liquid has returned to film flow, with the exception of some liquid branching between sheets on the right side of the column. The main conclusion to be drawn from these images is that the liquid holdup is not constant throughout the column, but depends on elevation. Total column holdup will also be a function of the number of packing elements installed in the column. Liquid accumulation in the column, particularly as seen in the joint region, contributes to poor hydraulic and mass transfer performance. Capacity is limited by increased pressure drop and approach to flood that accompanies a reduction in flow area for vapor. Mass transfer is inhibited by increased resistance in large liquid regions as opposed to thin films in good contact with vapor.

Despite the improvement in image contrast and the reduction of image artifacts provided by the GE scanner, there are some phenomena that will be observed with any CT imaging system. One of these occurrences is beam hardening. Even with a very high

energy X-ray source, large regions of dense material will present problems for image reconstruction algorithms. An example of such behavior is shown in Figure 4-19. The packing element contained a steel pin to hold the metal sheets together, which is visible at the elevation at which this image was obtained. Along the longest axis of the pin, the beam hardening is the greatest. The dense material significantly altered the energies of the X-ray beams that traveled along that path. This resulted in the material along the line defined by the pin to be viewed as lower attenuating than it truly was since the average energy of the beam dropped. The resulting image shows an apparent discontinuity of the column wall at either end of the pin. This known to not be the physical reality of the system, but could potentially affect image analysis in those regions. The bright colored pin also saturates the detectors resulting in the pin being assigned the maximum grayscale value possible. Also as a result of beam hardening, the boundaries of the pin are not clearly defined, and the fuzzy edges affect neighboring pixels.

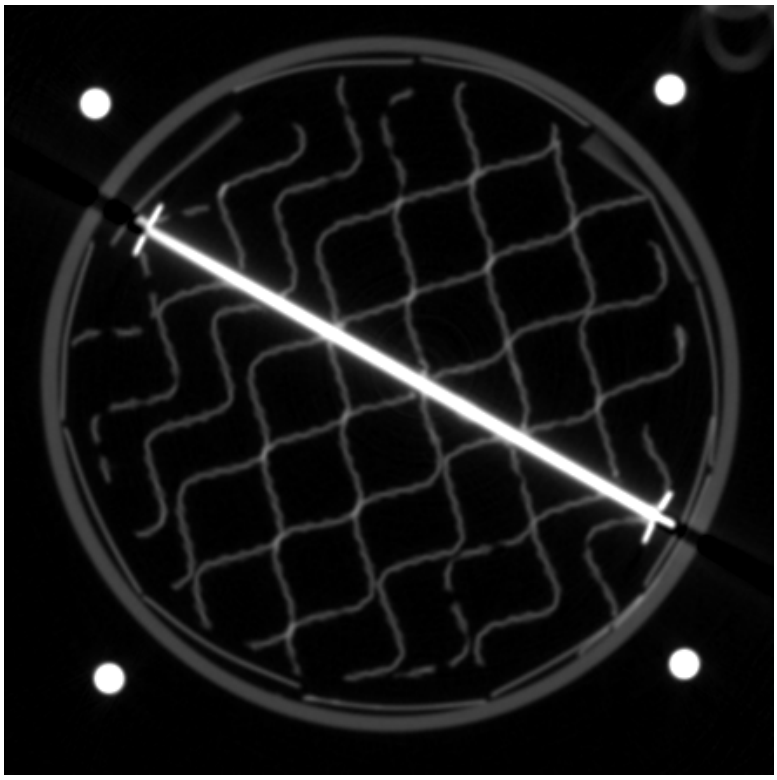

Figure 4-19. Example of beam hardening in a CT image from the GE scanner.

4.3 Void Fraction and Liquid Holdup from CT Slices

By analyzing the pixel grayscale values in the 2-D CT slices obtained from the 3DID and GE scanners, the void fraction of dry packing and liquid holdup in irrigated packing was calculated. The first step in processing the images is to determine the characteristic grayscale values for each of the phases present in an image. Since the analysis was limited to the column interior, the phases possible were air, water, and packing (steel). Image histograms were used to determine the most likely value for each phase. Figure 4-20 is a portion of a histogram for CT images from the GE scanner. A similar result was obtained for the 3DID scanner images with a reduced number of

possible grayscales. The characteristic values are not the same for both scanners due to the large difference in X-ray source energy. Image artifacts and measurement noise associated with the 3DID scanner resulted in histograms with broader peaks.

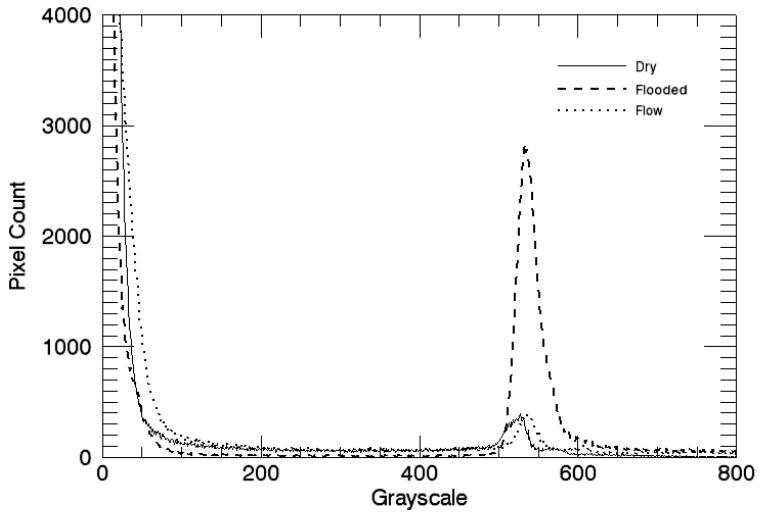

Figure 4-20. Histogram of three images representing different flow conditions for structured packing.

The histogram has been cropped to the region of interest that contains peaks for air and water pixels. Each peak exhibits a normal distribution for a pure material. At the left edge of the image, the plot increases to a very large number of pixels, which represents air. The purpose of the air calibration prior to the scans is to set the attenuation of air as the baseline value that other materials are compared to. Doing so forces a distribution centered at approximately zero. The number of pixels shown at zero will be higher, as grayscales cannot be negative. At a value of approximately 580, a large peak representing water is observed for the flooded image. In both the dry and flow

images, a smaller peak is observed at nearly the same region. The dry image used for this histogram exhibited some static holdup, which will result in the grayscale of some pixels falling in the water region. Due to variances in air conditions and X-ray source energy, the characteristic grayscale values for each material can vary from scan to scan.

The dry and flow images contain a greater number of pixels in the grayscale region from approximately 100 to 500. Due to the partial volume effect, thin packing sheets are not resolved when the majority of the pixel is filled by water as opposed to air, thus grayscale values in this region are not as plentiful for the flooded image. Since the grayscale value of a pixel filled with metal packing cannot be determined due to the packing sheets being thin, an estimation of the grayscale value of a metal-filled pixel is required. The stainless steel struts outside the column region provide a good estimate which can then be fine tuned to produce a void fraction value close to the vendor specified figure. To verify the value, packing sheets were extracted from a surplus packing element, stacked, hammered flat, and folded to occupy more than one pixel of space. The sheets were attached to the side of the column during a scan and analyzed in the images to determine the characteristic grayscale. For the number of pixels in the grayscale range between air and water, the pixel value is divided by the chosen characteristic grayscale for metal packing to determine the fraction of the pixel filled by metal. Summing the fractions over the entire column area of pixels and dividing by the total column area determines the metal fraction. The sum of the metal fraction and void fraction will equal unity in a completely dry image.

A separate method for identifying grayscale values involves drawing a line across the image and plotting the grayscale value of each pixel along the line. This is known as a line profile. Additional information can be gathered for the measurement of features in the image relative to the size of a pixel. One specific example is evaluating the

difference in grayscale between dry and flow images by investigating the edge response function along a line that passes across packing sheets. Figure 4-21 is an example of line profiles drawn in dry and flow images, with both the images and the grayscale response shown. The lines are shown in red on the CT images.

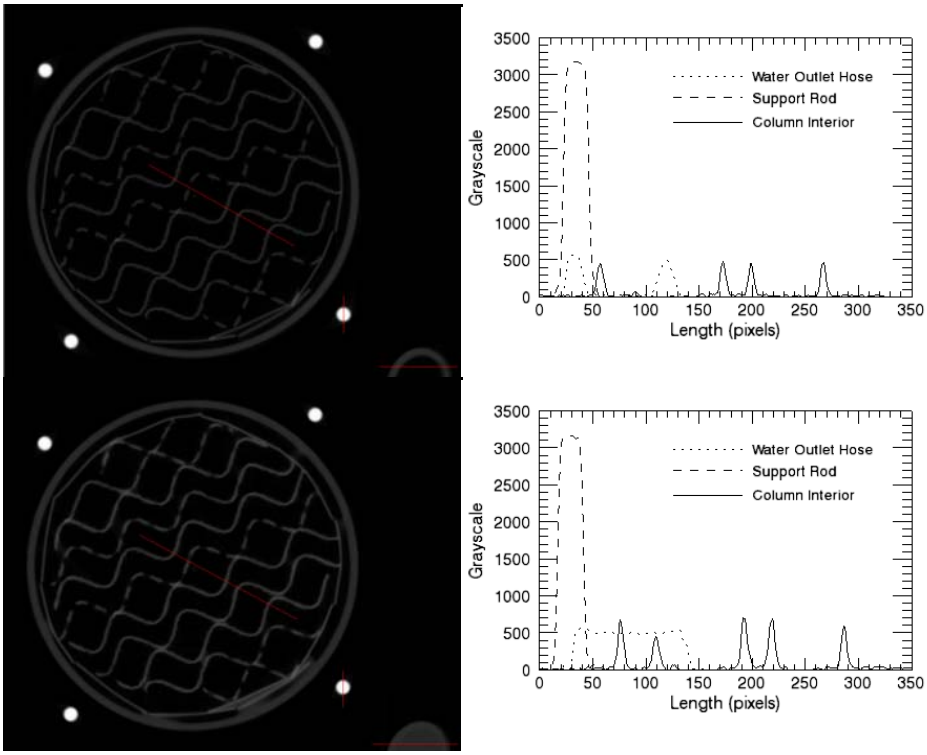

Figure 4-21. Line profiles for dry (top) and flow (bottom) CT images. Liquid flow is 10.5 GPM/ft^2 and vapor F-factor is 1.0.

The profile through the stainless steel support rod appears the same in both the dry and flow line profile. The grayscale response forms a plateau at the characteristic grayscale value of the bulk material. Near the edges, the response drops off sharply. A clear difference can be seen in the response for the line drawn through the water outlet hose. In the dry image, the hose is empty, and the response between the peaks for the

hose wall is low. However, when the hose is full during the flow scan, the height of the plateau region defines the average grayscale of water. The characteristic grayscales for water and the vinyl wall of the hose are similar. The water grayscale is fairly constant across the tube. Finally, the response across the packing sheets is different for the flow and dry scans. In the dry profile, the peaks for water are shorter and narrower, indicating that a small amount of material is present. As the grayscale value of metal packing is expected to be high, the reduced height of the packing peaks indicates that the packing is small compared to the pixel size. The peaks do not exhibit a plateau, but instead resemble a spike. In the flow image however, the packing peaks are higher and somewhat broader. This signifies that material that attenuates X-rays more than air was present in the region around the packing, and added to the overall thickness in the region being considered. Quantification of the liquid film thickness by comparing the respective edge responses for the dry and flow cases is difficult due to the small fraction of water present compared to the size of a pixel. The line profiles are helpful in determining the grayscales associated with particular regions in the column.

When the GE scanner was used, the local void fraction of dry packing and liquid holdup of the irrigated bed was evaluated for 16 slices through the packed section, spaced at 1-inch intervals. For reference, Figure 4-22 shows a radiogram of the column equipped with Mellapak 250Y half-elements. The image has been marked to denote the relative elevation from the zero height point on the scanner turntable. The joint between packing elements can be identified by the small void space that spans the column diameter and by the change of packing sheet orientation. In the top element, the pin holding the corrugated sheets together that was seen in Figure 4-19 is visible.

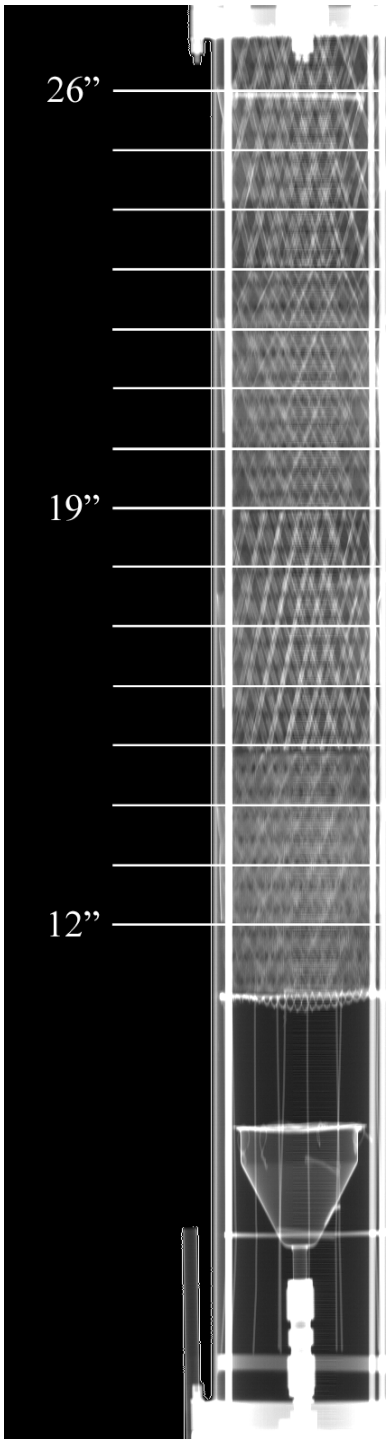

Figure 4-22. Radiogram with scan planes for bulk holdup and void fraction marked.

Figure 4-23 shows the variation in void fraction with elevation in the packed bed along with the average from the 16 CT slices and the vendor-specified value. It is clear that void fraction is not constant throughout the bed. Factors that contribute to this behavior are the location of the scan plane in relation to perforations, wiper bands, and joint interfaces. The vendor specified value does not account for wiper bands, which will cause the average true void to be lower. Additionally, the 16 slices throughout the bed may fall in locations that skew the average. For instance, if a slice is located at a packing element joint, the calculated void fraction will be higher than in the bulk of the packing.

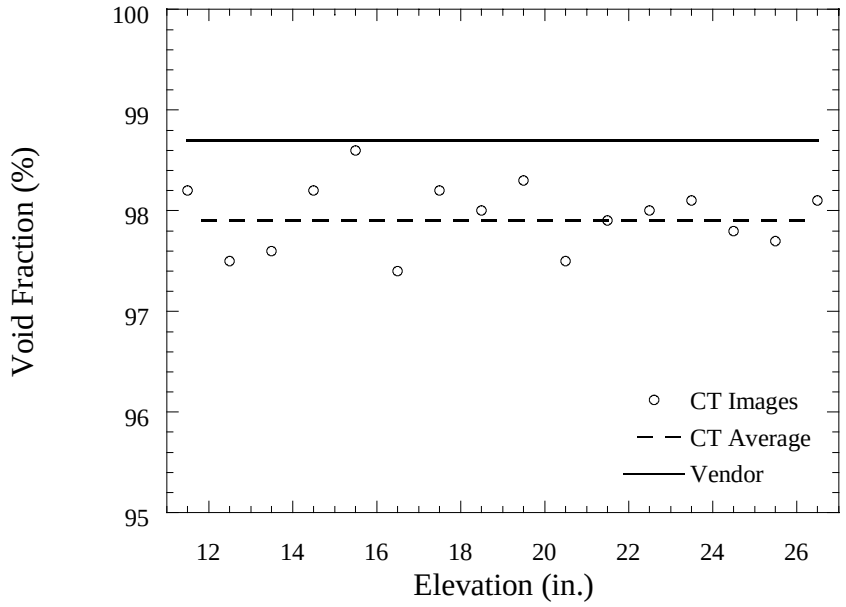

Figure 4-23. Void fraction profile in Mellapak 250Y structured packing.

In addition to observing behavior throughout the column, the packing element joint area was investigated further by taking a series of closely spaced CT slices near the interface. The total height scanned above and below the actual interface ranged from 0.12 to 0.45 inches using slice spacings of 0.03 to 0.05 inches. A plot of void fraction

versus elevation is shown in Figure 4-24. The horizontal line was determined to be the elevation where the actual interface was located. Portions of corrugated sheets from both elements were visible in CT images obtained at this elevation.

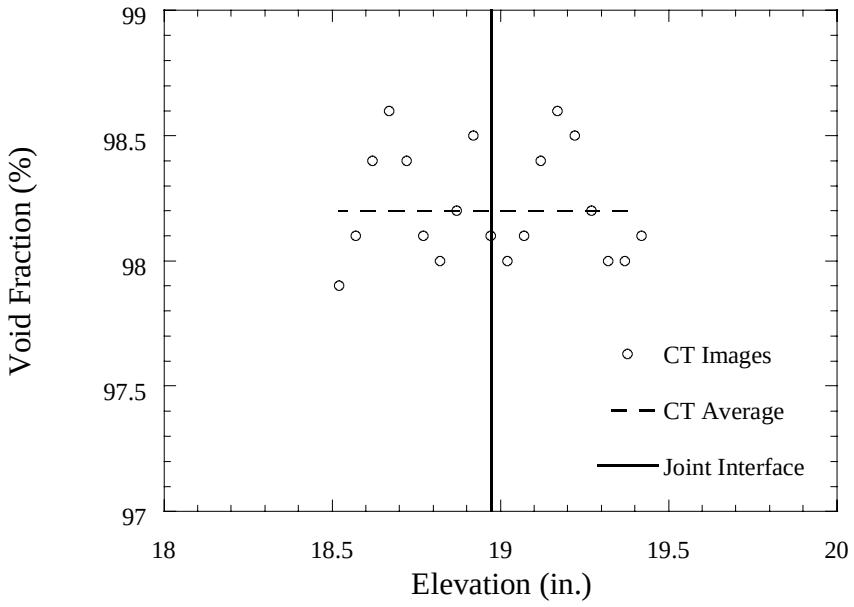

Figure 4-24. Void fraction in packing element joint region.

Difference images were created to analyze liquid holdup by subtracting the dry image from a flow image at the corresponding elevation. Applying the void fraction calculations to the water phase present in the column using the characteristic water grayscale provides the fractional amount of liquid at a particular location in the packed bed. Image artifacts with the 3DID scanner posed problems for the analysis, as the artifacts were within the characteristic grayscale range for water pixels. Thus, holdup calculations could not be automated. Pixels within the column region were classified as either artifact or water, and only water pixels were selected to add to the current count.

The procedure was tedious and very subjective. Error was introduced if pixels were misclassified.

As the column was operated well below the loading point when the 3DID scanner was used, the holdup was expected to be independent of air rate. In Figure 4-25, holdup is shown to vary widely with elevation, liquid rate, and vapor rate. In general, and as expected, the holdup was lower for lower liquid rates. A total of 15 elevations were imaged, but several elevations were left out of the analysis because of overwhelming artifacts.

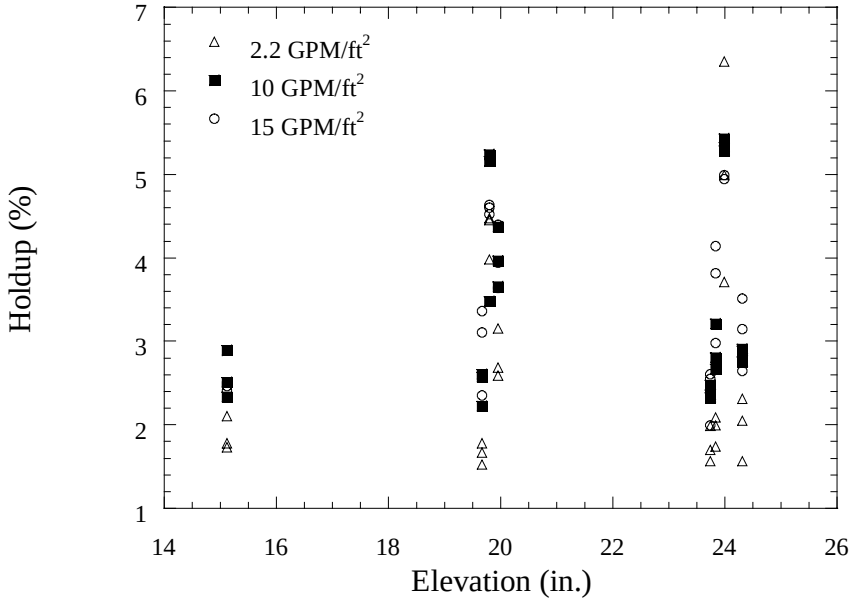

Figure 4-25. Liquid holdup calculated from images obtained with the 3DID scanner. Vapor flow rates were F-factors of 0.14, 0.20, and 0.27.

Moving to the GE scanner provided a significant reduction of artifacts in the images. The holdup calculations could be performed numerically using IDL, which increased the throughput of data analysis. The first images acquired with the GE scanner

were for moderate F-factors up to 0.48. As depicted in Figure 4-26, for liquid rates of 2.2 and 10.5 GPM/ft^2, the holdup was mostly independent of the gas rate, indicating that the column was still operating below the loading point. However, for a liquid rate of 15 GPM/ft^2, the holdup exhibited greater variation with respect to air rate. At the low vapor F-factor of 0.27, the liquid holdup was similar to that calculated for a liquid rate of 10.5 GPM/ft^2, at least near the bottom of the column. At higher elevations, the holdup was higher, mirroring the data calculated for the F-factor of 0.48. At a lower vapor rate and higher liquid rate, the vapor drag forces on the falling liquid are low compared to the gravitational force acting on the liquid. The liquid is then able to drain unobstructed from the bed. As the vapor rate increases, however, the liquid will be held up in the packed bed by the vapor drag. The fact that the holdup at 15 GPM/ft^2 is similar for both air rates near the top of the column is likely a distribution issue. After approximately 4 inches, which is the height of one packing element, the holdup plots begin to deviate, suggesting a change in flow pattern as the first element interface is encountered.

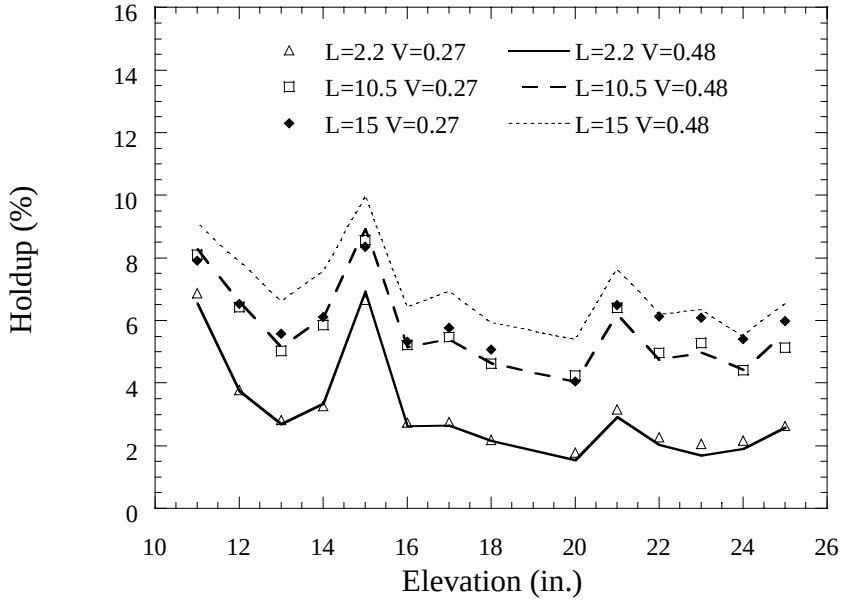

Figure 4-26. Liquid holdup as a function of elevation calculated from GE scanner images. Liquid rate unit is GPM/ft^2, vapor rate unit is F-factor.

Overall, local peaks are observed in the holdup plots. When elevation 15 is located on Figure 4-22, it is found to be located slightly above a packing element interface. Elevation 11 is located in the bottom of the bottom-most packing element, and near to the vapor inlet. Vapor entrance effects were noticeable during column operation using video cameras mounted in the scanning bay. Both vapor inlet considerations and joint behavior are likely to result in increased holdup as observed in Figure 4-26.

At higher vapor rates, the holdup behavior becomes somewhat more erratic. In Figure 4-27, the liquid holdup throughout the column is shown for F-factors of 1.0 and 1.4. More variation is seen across the packed section, with fewer regions where the profile is relatively flat. The holdup is actually higher for both liquid rates at an F-factor of 1.0 compared to the data at F-factor 1.4. This behavior is not expected.

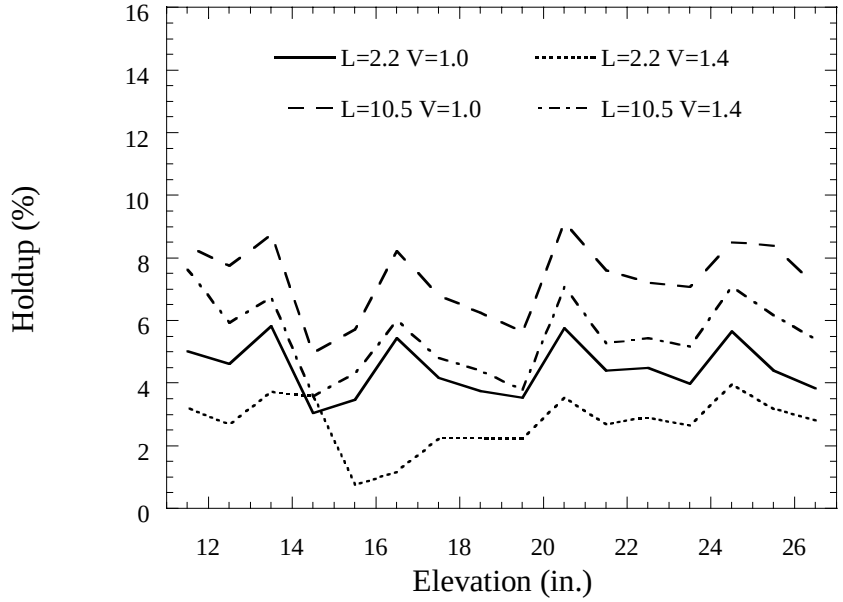

Figure 4-27. Liquid holdup versus elevation at F-factors of 1.0 and 1.4. Liquid rate is expressed in GPM/ft^2.

At a liquid rate of 2.2 GPM/ft^2 F-factor of 1.4, the overall holdup is comparably low. During operation at this rate, the bottom packing element was bordering on a flooding regime. The low liquid flow allowed material to be easily pushed back into the column by the higher vapor flow, creating a turbulent pattern in the bottom element. Such flow will not be resolved by the X-ray technique, as the time scales are very different. The flow will appear as a random assortment of pixels with grayscales determined by partial volume and partial time components in a time averaged image. Near elevation 14, the holdup is a minimum for three of the rates. This corresponds to an area slightly below a packing joint. Liquid pooling at the interface above seems to impede the overall liquid progress through the bed. Poor overall distribution will result from accumulation in any one part of the column.

Local peaks in liquid holdup observed near packing joints were further investigated by calculating the holdup for closely spaced slices taken around element interfaces. Initially, a total of 8 slices were taken at 0.03-inch spacing resulting in a total height of 0.24 inches. The holdup profiles at the bottom-most joint are shown in Figure 4-28. The vertical line represents the actual location of the interface. As was observed for the holdup data at these same flow rates, the holdup is independent of gas rate. Each condition exhibited higher liquid holdup above the joint, transitioning to a moderate value at the interface, and tapering off as the liquid enters the bottom packing element. The apparent discontinuity in holdup from packing entrance to packing exit suggests that the holdup above the joint was actually a local maximum. Additional slices taken above and below the joint would provide additional insight to the expected pattern of holdup across an entire packing element.

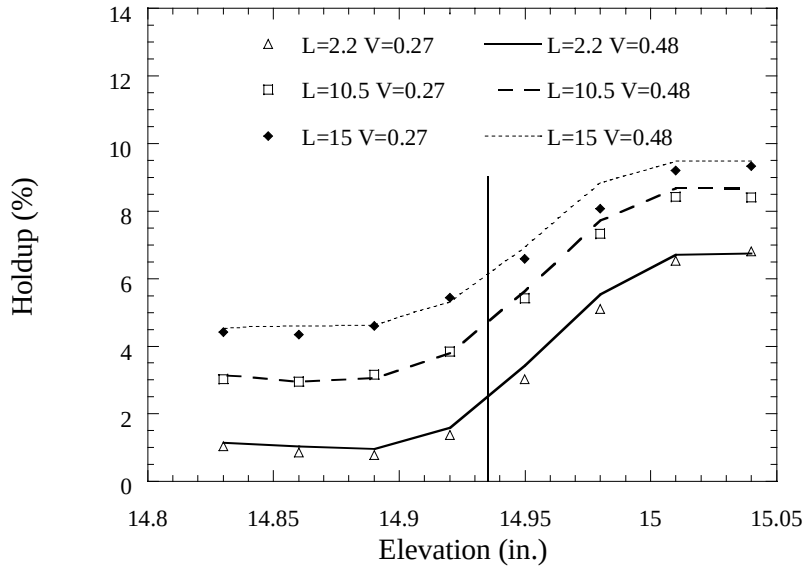

Figure 4-28. Liquid holdup at bottom packing element joint. Liquid rate unit is GPM/ft^2, vapor rate unit is F-factor. Vertical line represents actual interface.

The number of slices around the joint region was increased to 19 in subsequent scans of the middle packing joint at higher F-factors. The slice spacing was increased to 0.05 inches. Holdup profiles for F-factors of 1.0 and 1.4 are shown in Figure 4-29. The behavior in the region that was shown previously in Figure 4-28 is very similar. Additional slices taken above the interface show that the high holdup at the joint is a local maximum, where the value of holdup ranges roughly from 2 to 5 times the value observed in the bulk of the element. The region of liquid accumulation extends approximately 0.25 to 0.4 inches above the interface of the elements. After passing into the next element, the holdup returns to a lower value. Similar to the bulk column holdup data at higher vapor rates, the liquid holdup appears to decrease with increasing F-factor. The data in Figure 4-29 was also obtained just prior to the GE X-ray scanner experiencing problems. Level shifts in the data sets could lead to such a phenomenon in the calculations.

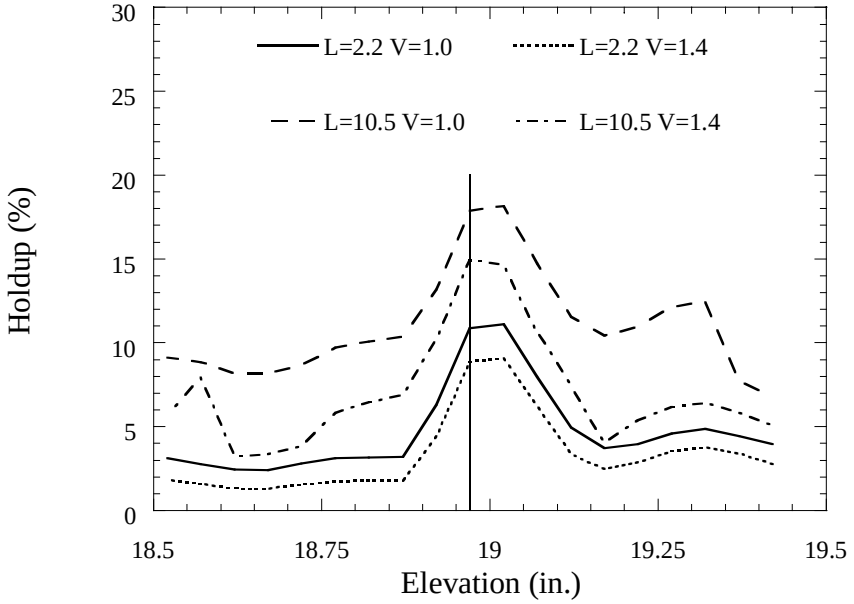

Figure 4-29. Profile of liquid holdup at a packing element interface. Liquid rate unit is GPM/ft^2, vapor rate unit is F-factor. Vertical line represents actual interface.

To evaluate the validity of the holdup data calculated from X-ray CT images, traditional experimental methods for determining holdup were used. Both the 6-inch air-water contactor used for the imaging studies and the SRP 18-inch air-water column were used to determine the volume of liquid that drained from the packed bed following shutoff at different flow conditions. In Figure 4-30, the results of experimental holdup measurements on the column used for imaging are compared with SRP data from the hydraulic testing of Mellapak 250Y. The experimental measurements on the smaller column were limited to low F-factors provided by the building nitrogen supply. The agreement with the large column data in the low range of vapor rates is acceptable. The general trend shows holdup to be independent of gas rate up to the loading point, and then increasing dramatically as the flood point is approached. A corresponding increase in overall column pressure drop would accompany the sharp upturn in holdup.

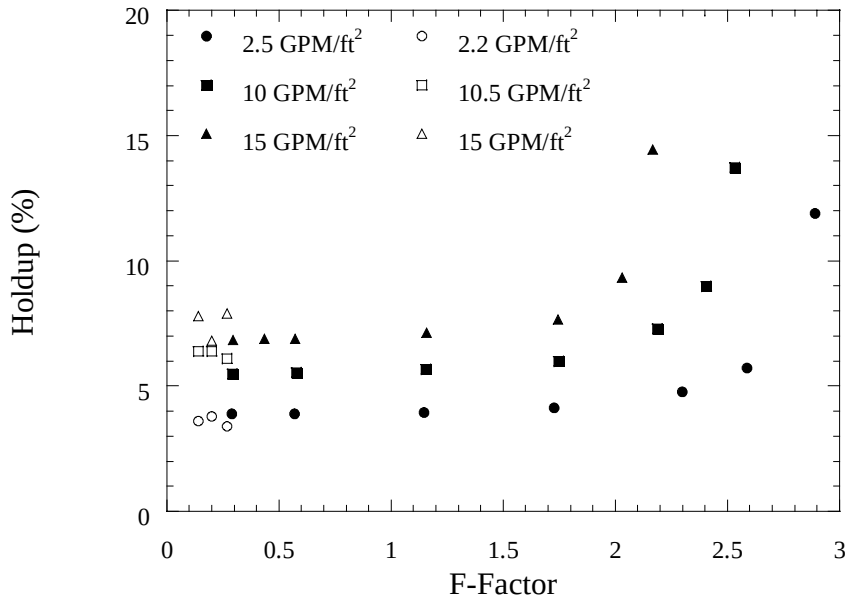

Figure 4-30. Experimental liquid holdup for Mellapak 250Y. Solid data markers represent SRP column data, open data markers taken from 6-inch column used for X-ray experiments.

The traditional experimental techniques report the column average holdup, whereas image analysis provides a local value that has been shown to vary with elevation. Comparing the experimental values of liquid holdup to the values calculated from X-ray CT requires the data from images to be averaged over the series of equally spaced slices to obtain an average holdup for the column. The average of the holdup values determined from CT images is not a true representation of the entire column because relatively few data points were taken in relation to the column height, some of which fell in regions near joints known to deviate highly from the bulk flow. However, as seen in Figure 4-31, the agreement between the two methods generally falls within 20 percent. The traditional method of calculating holdup does not account for liquid that

remains in the bed as static holdup, whereas the CT technique gives the total amount of liquid present in a slice, whether it constitutes a static or dynamic holdup.

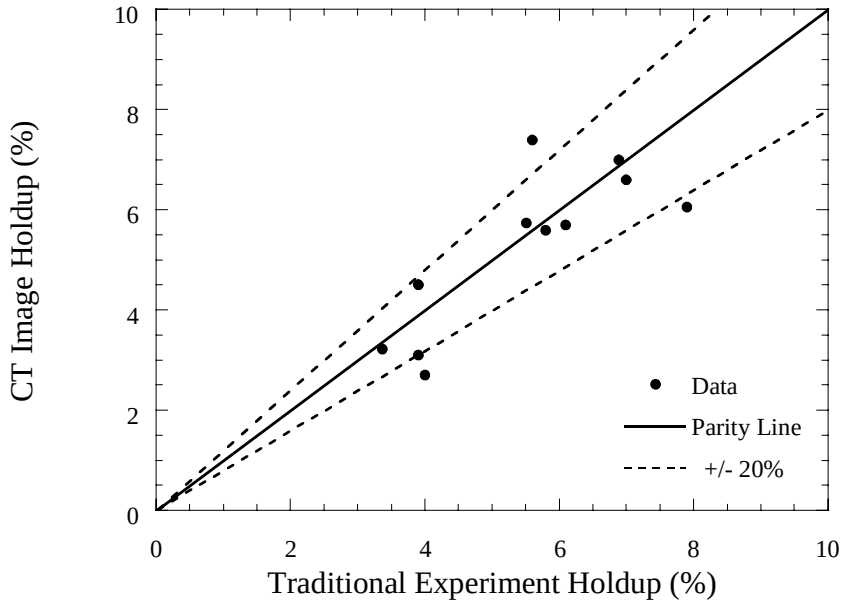

Figure 4-31. Parity plot comparing two experimental methods for predicting holdup.

When the experimental data measured for holdup is compared to two existing models for predicting column performance, the strongest agreement exists between the two experimental techniques. Neither the Stichlmair model nor the Rocha-Bravo-Fair model predict liquid holdup close to the experimental values. It should be noted that all data in Figure 4-32 is below the loading point. Models for predicting hydraulic performance above the loading point are notoriously inaccurate, as the hydraulic parameters are tweaked or fit empirically to satisfy the mass transfer constraints. Both models underestimate the liquid holdup at low liquid rates. The Rocha-Bravo-Fair model consistently predicts values for holdup much lower than experimental data showed,

whether it was by traditional experiment or by CT image analysis. The Stichlmair model follows the general curve exhibited by the experiment data at intermediate liquid rates, but begins to deviate from the data as higher liquid rates are encountered.

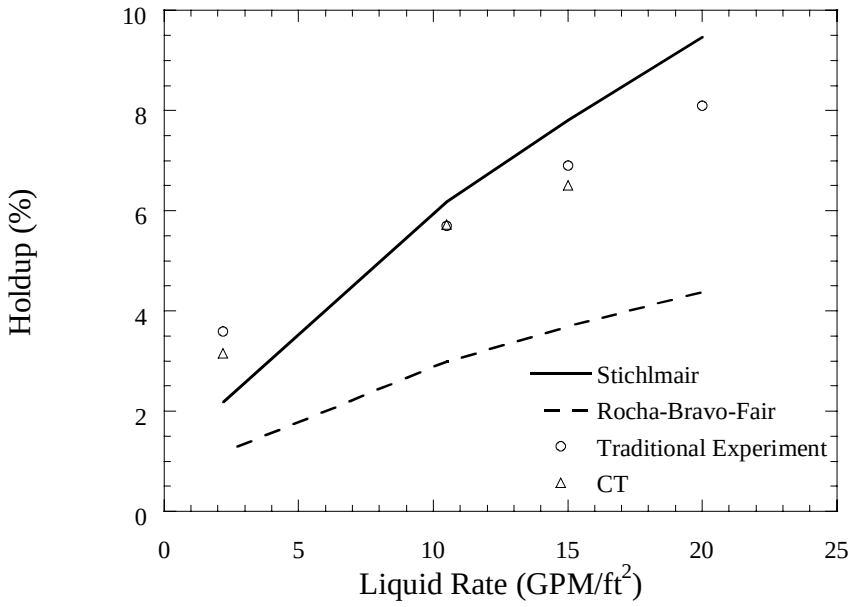

Figure 4-32. Comparison of traditional and X-ray experimental measurements of liquid holdup versus predictive models.

4.4 3-D Reconstructions from GE Data

With each X-ray CT slice being of finite thickness, a series of slices can be stacked to simulate a volume. As the slice thickness and spacing between slices decreases, the data set becomes a more accurate representation of the physical system. Volumetric visualization of the packed bed under dry and flow conditions was possible using this approach. As with CT slices, the 3-D reconstructions of the column under flow conditions represents a time average of the flow behavior over the course of the scan.

Initially, a 3-inch section of structured packing at the top of the bed just below the distributor was modeled while a liquid flow of 10.5 GPM/ft^2 and vapor F-factor of 0.48 was applied. The first attempt at modeling was used to evaluate the technique therefore a corresponding dry model was not obtained. The reconstruction shown in Figure 4-33 was provided by General Electric's image processing team.

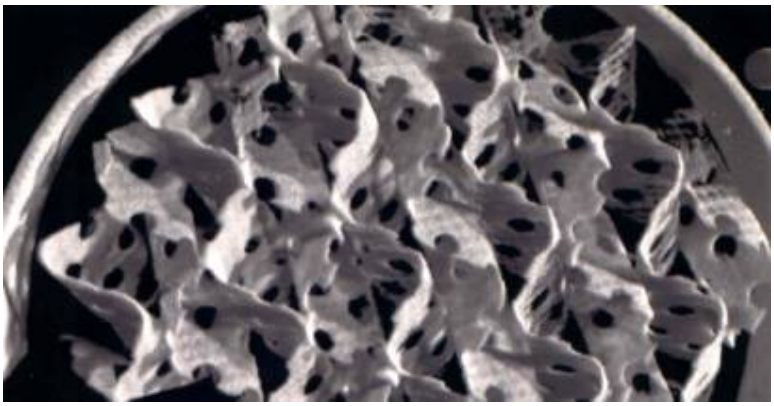

Figure 4-33. 3-inch model of irrigated structured packing created from a series of CT slices. Liquid rate is 10.5 GPM/ft^2 and vapor F-factor is 0.48.

The resolution of the X-ray CT scanner is sufficient to capture the surface texture and perforations of the packing sheets. Without a corresponding dry image to compare to, it is somewhat difficult to identify features that may be present due to flow. Also, since the model was obtained near the top of the bed, the liquid has not had ample time to distribute across the sheets. Based on this fact, it is presumed the majority of the liquid is in the center of the column. One theory that has been discussed relates to the appearance of the surface texturing. Near the column walls, the surface treatment appears more pronounced than it does in the middle of the column. It would be expected that a film of liquid on the surface of the packing would obscure the surface texturing, resulting in a

smoother appearance in a reconstruction of this type. However, the light source that has been applied to highlight the features of the packing may be contributing to this observation.

Subsequent experiments using the 3-D modeling technique employed both dry and flow models at identical locations in the packed column. Thus, a series of subtracted images could be obtained that corresponded to the same region. In theory, the subtracted images could also be stacked to create a model that included only the liquid flowing through the bed. Unfortunately, the modeling scans are very lengthy. For example, at a spatial resolution of 0.01 inches for both the pixel dimension and slice spacing, a 600 slice, 6-inch model takes approximately 10 hours to obtain. Therefore it is critical to maintain precise control of the liquid and vapor flows to the column. The technique is currently unable to capture turbulent flow patterns such as those encountered as the flood point is approached. However, for cases where liquid films dominate at steady state, the reconstructions have shown some promise.

Using Amira, a three-dimensional data visualization software package, image stacks from subsequent modeling experiments were created. An example of such a reconstruction is shown in Figure 4-34. By manipulating the color table, noise and artifacts can be filtered out of the system and the features of interest, such as the packing, can be emphasized. The image shows a 6-inch tall section of the air-water column containing structured packing. As in the GE-provided image, the perforations and texture of the packing is apparent. Also visible in the image are the four steel column support rods, the acrylic column wall, and the water outlet hose, which is empty in this case. Bright spots in the packing signify regions of pixels where the metal fraction is higher, such as near the contact points of adjacent sheets.

Figure 4-34. 3-D reconstruction of air-water column using a series of 2-D CT images.

A cutaway view of the column showing the packing interior is shown in Figure 4-35. The wiper bands surrounding the elements are visible between the packing sheets and the column wall. The change in packing sheet orientation from one element to the next can also be seen. Numerous bright spots are visible on the open side surface of the packing due to the cutaway procedure. These are areas where packing sheets are in contact when the volume is viewed as a whole. A distinct void is observable at the interface between the two packing elements. The grayscales associated with metal packing, metal support rods, and the acrylic wall are constant, providing good differentiation among the materials present. The surface treatment and perforations can be examined in detail with this view. The perimeter of the perforations appears smooth, indicating that the spatial resolution of the 2-D images and the slice spacing is adequate.

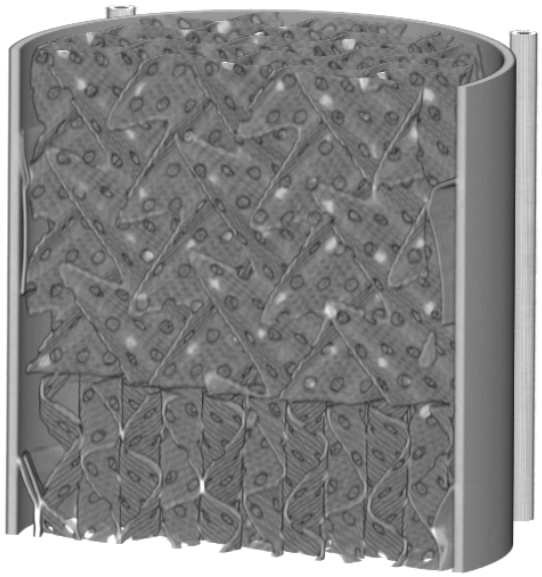

Figure 4-35. Cutaway view of air-water column containing structured packing.

If the two-dimensional CT images are cropped prior to being read into Amira, the column wall, support rods, and hoses can be removed in order to focus on the packing elements themselves. Figure 4-36 provides several views of a packing element reconstructed from cropped CT images obtained from the dry bed. The flow channels are clearly visible in the angular view. The wiper band appears around the perimeter of the element, including the tabs that have been bent to provide a seal against the column wall. Portions of the wiper band are not resolved after the cropping procedure since they touch the column wall. Due to the partial volume effect and the related low grayscale value of packing in the CT images, the packing sheets appear thicker in the reconstructions than they are in reality. However, all other characteristics of the packing are to scale.

Figure 4-36. 3-D reconstructions of a Mellapak 250Y half-element from X-ray CT data

In the side view, the tack welds used to fasten the wiper band to the element are visible. The top-down view provides a look at how the fit of 250-series packing in a relatively small column can emphasize wall effects. A large amount of void space can be seen in the upper- and lower-left portions of the image.

With the joint region of packing producing interesting results for liquid holdup, a 3-D reconstruction of the column cross section near a packing element joint was created. Seen in Figure 4-37, the overhead image shows how packing sheets from the lower element are visible through the flow channels of the upper element. As the total height of column viewed in this manner is decreased, the apparent void space will increase. The path for liquid flow from one element into the next is clearly non-ideal. Films falling off of sheets in the upper element are fed directly into void space in the lower element. Rising vapor in the flow channels interacts with this liquid, which must change direction sharply. This bottleneck serves as a likely point for flooding to begin.

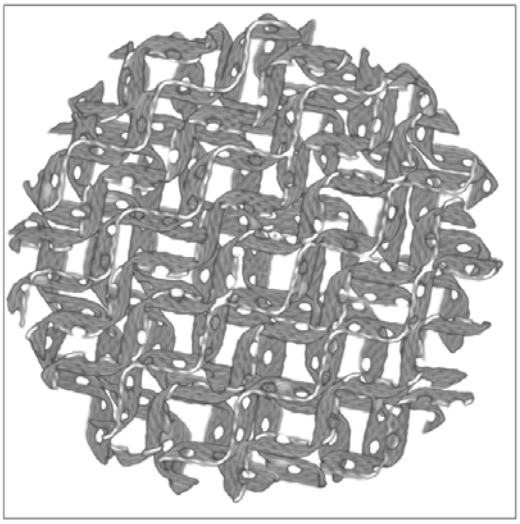

Figure 4-37. 3-D image of column cross-section as a packing element joint is approached.

Reconstructing 3-D models using CT slices obtained while flow was applied to the column can provide insight as to the liquid flow pattern in the column. This assumes that the liquid flow pattern remains relatively steady over the course of a scan, with the image stack being a time average. Several views of a flow model are shown in Figure 4-38. The liquid flow rate was 15 GPM/ft^2 and the vapor F-factor was 1.3.

Several interesting features can be noted in the flow model images. When considering the angle view of the packing element, the corrugated sheets appear slightly wider and significantly brighter than for the dry case in Figure 4-36. The can be contributed to the presence of water on the surface. Also, there are some fuzzy regions along the surface of the packing and visible in the flow channels. These can represent small regions of liquid that existed for a portion of the scan. Faint circular regions of material can be seen when looking down the flow channel. These are the volumetric equivalent of image artifacts due to flow.

The apparent packing thickness and some artifacts are also visible in the top down view. However, the most interesting aspects of that particular view are the appearance of the packing surface and the perforations. The surface texturing that was apparent in the dry images does not appear here in the flow reconstructions. Rather, a different pattern that resembles waves is visible. This likely indicates the presence of a water film on the surface of the packing sheets for the majority of the scan. When the column is observed under operation, regions of packing visible near the wall show the liquid films to continuously ripple. Additionally, the perforations on the sheets appear smaller and fuzzier than in the dry images. If liquid films were flowing over the perforations during the scan, the resulting images would exhibit behavior similar to what is observed. Clearly the area around the perforations must be changing over the course of the scan for the resolution to differ this much from the dry case.

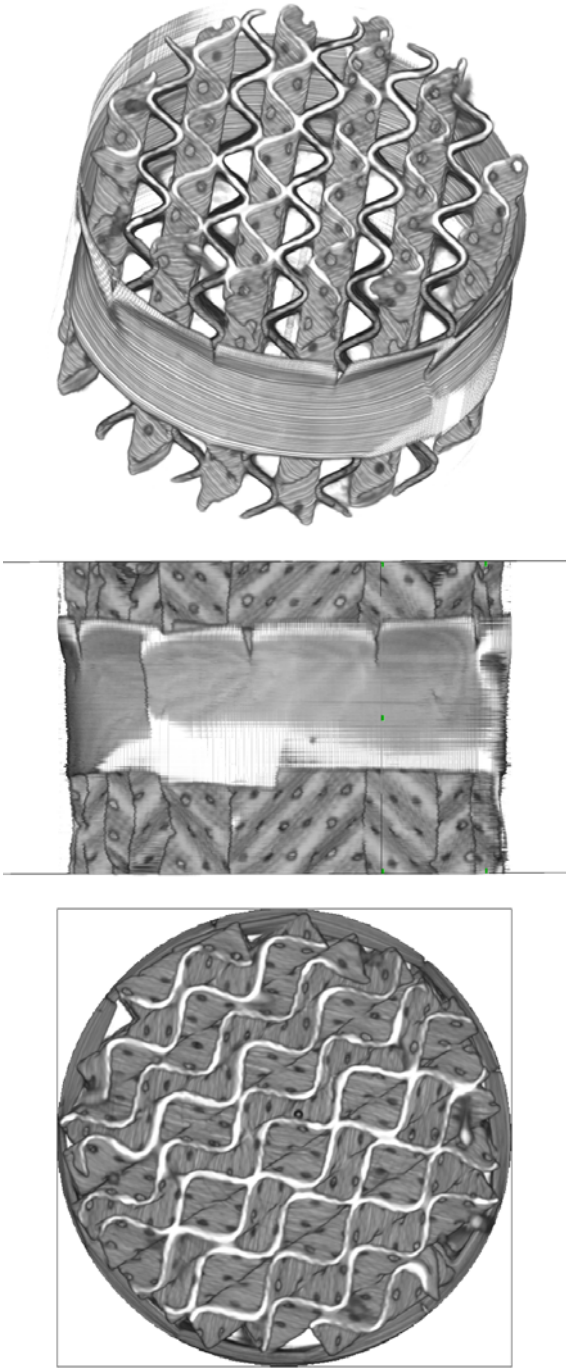

Figure 4-38. 3-D reconstructions of CT slices obtained under flow. Liquid rate is 15 GPM/ft^2 and vapor F-factor is 1.3.

Considering again the joint area, an image similar to Figure 4-37 was created to evaluate the difference between the packing appearances near the joint for dry and flow cases. With the region above the interface exhibiting much higher holdup than the rest of the element, it would be expected that the 3-D model of the region would contain interesting features related to liquid accumulation. Unfortunately, it is difficult to discern areas of liquid accumulation in the region between corrugated sheets. The packing sheets themselves exhibit a surface pattern similar to that observed for the bulk element in Figure 4-38. Similarly, the sheets appear somewhat thicker and brighter, and the perforations appear smaller and less resolved than in the dry images. Circular artifacts can be seen in the left hand side of the element. While excellent in reproducing images of dry packing, the image stack technique does not capture the small scale flow features necessary to visualize the liquid flow pattern itself or gross accumulations of liquid within an element.

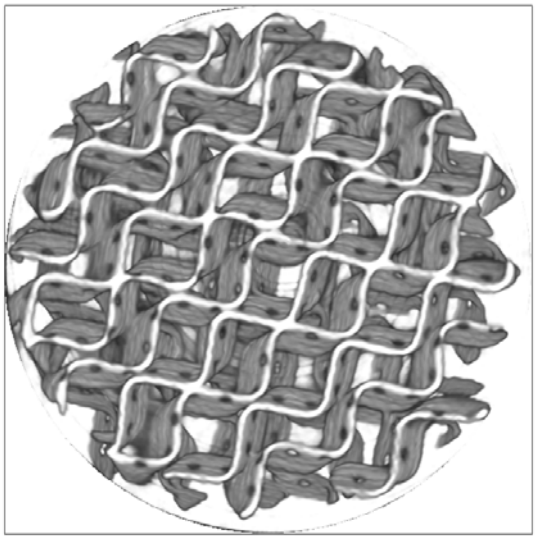

Figure 4-39. Packing element joint region under flow conditions. Liquid rate is 15 GPM/ft^2 and vapor F-factor is 1.3.

As each model consists of a large series of discrete CT slices, it is possible to apply the image analysis techniques for void fraction and liquid holdup discussed previously. Evaluating these parameters for a large data set permits a more detailed understanding of the flow behavior in the column as a whole, rather than solely on a local level. Plotting the two values together as shown in Figure 4-40 allows elevations of interest in one data set to be directly compared to the other data set.

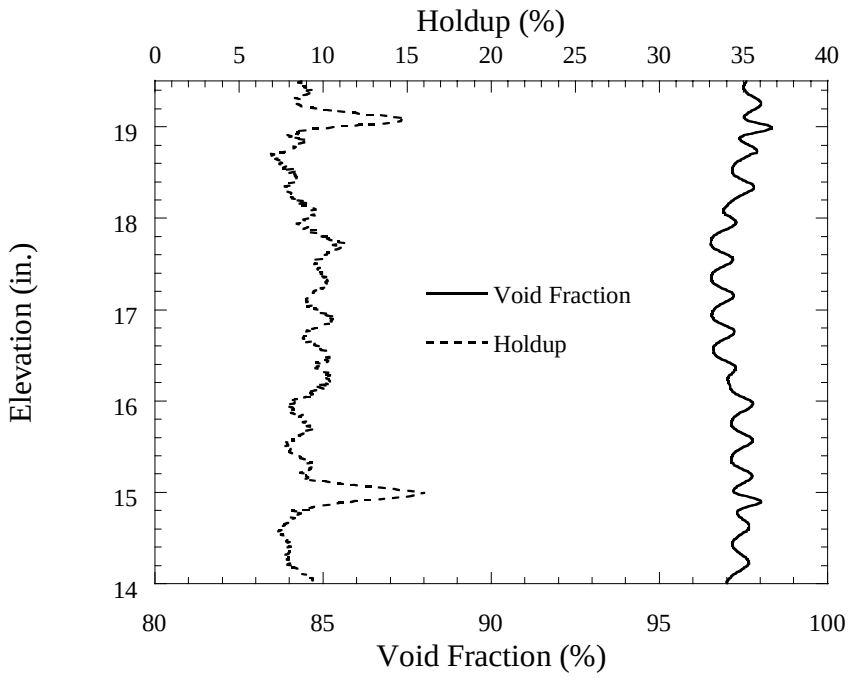

Figure 4-40. Void fraction and holdup profiles in a 5.5-inch tall section of packing. Liquid rate is 15 GPM/ft^2 and F-factor is 1.3.

Figure 4-40 shows that the void fraction profile in the packed bed follows an oscillatory pattern. The period of the regular oscillations is equal to the distance between perforations on the packings sheets. As expected, the void fraction is lower at elevations where no perforations are located, and higher when the slice plane is located within a

perforated region. It may also be noted that from a height roughly from 16.5 to 18 inches the void fraction profile shifts somewhat lower. This region of the column contains a wiper band. The presence of extra material in this region will decrease the apparent void fraction.

In terms of liquid holdup, the packing joint areas can be clearly identified by the large spikes. Just above the interface, the holdup can be nearly 3 times the value observed in the packing bulk. The lowest holdup appears to be located just below the top of a packing element. The holdup is not constant through the middle portion of the element, however. The holdup profile and void fraction profile appear to be related. This is independent of the calculation method, since the holdup and void fraction were both normalized over the entire column cross-section. Some areas where the void fraction exhibits a maximum, the holdup exhibits a minimum. In other regions, the holdup remains constant or increases when the void fraction increases. This could indicate that the liquid intermittently flows over the perforations.

Image stacks are also useful for troubleshooting. At times scanner error is too small or short-lived to be noticed; yet when a stack of slices obtained over a large time is constructed, differences in characteristic grayscales can indicate that a malfunction has occurred. Figure 4-41 is an example of this phenomenon, known as a level shift.

At the top of the model, the column wall appears as a medium gray, and the packing in the column interior exhibits a similar color. After the scanner has proceeded approximately one-fifth of the way through the top element, the grayscale of the wall and packing changes. A similar change can also be seen just above the bottom of the top element. Something has caused the scanner to view these regions as a different material than the same region in previous slices. Causes for such behavior could be detector

malfunctions or variations in X-ray source energy. This undesirable occurrence will affect data analysis, as the characteristic levels of each material will need to be adjusted.

Figure 4-41. Cutaway view of packing showing level shifts that occur over the course of a scan.

Another example of a troubleshooting application is evaluation of the scanner drift. X-ray detectors tend to be very sensitive to humidity. The air calibration steps prior to scanning are designed to minimize variation in data due to changes in the composition of air. When the air-water contactor is operated in the enclosed space that houses the X-ray system, significant variation in the properties of air can be expected. Although a mist eliminator is installed in the column, the air exiting the top of the device no doubt contains a significant fraction of water, perhaps even to the point of saturation. While the volume of the room is large enough to not pose problems for short scans, experiments that take several hours to complete, such as data acquisition for 3-D models, are susceptible to scanner drift. Figure 4-42 shows the behavior of a 30x30 region in a 600-slice CT model. The region contains only air for the entire scan, with the 900 pixels

averaged to produce a data point for each slice. At 50 seconds per slice, the total scan time was roughly 10 hours.

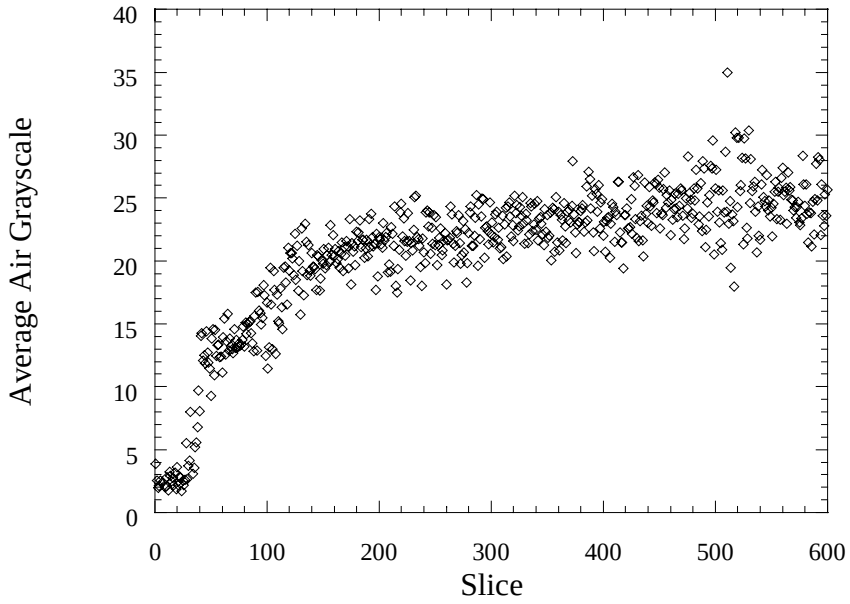

Figure 4-42. Variation in average grayscale of air over a 10-hour scan.

The air average started off fairly low and maintained a tight distribution for the first 20 slices. Spikes in the response associated with a detector error not visible in the plot occurred around slice number 35. The average value began to climb steeply and become noisier. Around slice 200 the value began to level off, but continued to exhibit high amplitude noise. In terms of the total number of grayscales possible, the increase from an average of 3 to an average of 24 over 10 hours was minimal. However, it provided insight necessary to determine if any corrections needed to be applied to the characteristic material grayscales used in the image analysis procedures.

4.5 Isosurfaces from GE Data

In order to perform numerical analysis on the volumes created from individual CT slices, it was necessary to establish a continuous description of the surfaces contained in the images, rather than just a visual representation. The process of creating an isosurface from a volumetric data set requires the selection of a characteristic threshold value. The threshold defines the location of the surface to be created. The surface will be calculated and constructed in such a way that data with values below the threshold will be on one side of the plane, and data with values higher than the threshold will be located on the opposite side of the plane.

To benchmark the surfacing procedure, a set of dry model data for the air-water contactor was considered. In order to ensure that the surface constructed represented the packing as desired, the 2-D CT data was cropped just inside the column wall. A total of 390 slices were used, representing 3.9 inches of the packed section height. The goal was to model and calculate the area available in one Mellapak 250Y half element. The stack was broken up into four sections to reduce the computational load.

A histogram was obtained for the data set to determine the distribution of grayscale values, including the maximum and minimum. For the dry case, cropping the images inside the column wall limits the materials being considered to air and packing. Since many of the data values were partial volume forms of packing, the threshold grayscale value needed to be chosen low enough to include the voxels fractionally filled by metal, yet exclude air pixels with values at the high end of the characteristic distribution. In an ideal two-phase system, the histogram peaks for each phase would be very sharp, narrow, and distinct, and the optimal threshold to differentiate between the two phases would be the grayscale located halfway between the peaks. However, the structured packing system presents a unique challenge because the packing sheets are so

thin. This results in a broad distribution of grayscale values representing partial volume effects that overlaps with the distribution of air pixels. Thus, selection of the threshold is more complex. By analyzing the histogram in Figure 4-43, a threshold value of 150 was chosen to distinguish the structured packing surface. The peak near 40 represents air, with a much smaller and broader peak centered at 400 representing the structured packing. If the right hand side of the air peak is extended to the x-axis, it appears to intersect at an approximate grayscale of 100. In order to ensure that no air pixels were included in the packing surface, the threshold was chosen slightly higher, near the region where the left side of the broad peak of packing pixels begins to taper off. The normal distribution of packing pixels extrapolates to intersect the x-axis near a grayscale of 200.

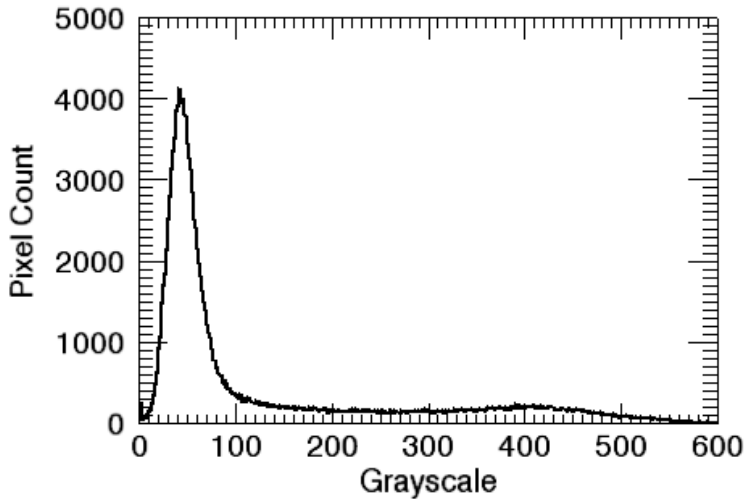

Figure 4-43. Histogram for CT image of dry structured packing, from which a threshold grayscale of 150 was chosen.

Once a threshold value was obtained, the surface could be created, viewed, and used for calculations. Amira contains a built-in module for the calculation of surface area

and volume occupied by a surface. If too high a threshold were chosen, portions of the packing would be excluded from the isosurface. Conversely, if too low a threshold was used, then pixels representing air would be included when creating the surface, introducing error. The surface area calculated from the isosurfaced CT images was compared to the vendor-specified surface area.

A similar procedure was applied to CT subtraction images to evaluate the interfacial area between air and water in the packed bed. A series of difference images was created by subtracting the slices of a dry model from flow model slices where the liquid rate was 15 GPM/ft^2 and the vapor F-factor was 1.3. The subtraction data was cropped close to the inside of the column wall, and the resulting phases for analysis were limited to water and air. The interfacial area derived from the CT subtraction isosurface was compared to model predictions for packing fractional area and experimental data for reactive surface area obtained in a packed bed.

The choice of a threshold for water proved more difficult than choosing the threshold for packing. A significant portion of the water images represented partial volume and partial time conditions, which resulted in a large number of pixels with low grayscale values. The threshold determination required a decision to be made regarding how close to the characteristic values of air one could go before blurring the line between partial volume or time water pixels and noisy air pixels. Variations in average air and water grayscales over the course of the scan were also important considerations. Again, a image histogram was consulted to determine the proper threshold grayscale. The histogram for a sample subtraction image is shown in Figure 4-44.

The distribution of grayscales is quite different for the subtraction images than the images of dry structured packing. The air peak has been shifted to the left, and a large number of pixels with a grayscale of zero are present. The subtraction process can act as

a noise filter, resulting in pixels with negative grayscales. Such pixels are mapped to a grayscale of zero when the subtraction image is created, thus artificially increasing the population. Clearly the pixels representing water and air are overlapping, and no clear peak is evident for water. The characteristic grayscale value typically used for analysis of water pixels is approximately 180. To eliminate artificial noise being introduced to the water isosurface, the threshold was chosen to be 50. This value was located near the far right edge of the air peak when extrapolated to the x-axis, and was low enough to include a good portion of the liquid phase. Choosing the threshold any higher would not capture all water pixels, but choosing any lower would introduce artificial surface from air and artifact pixels.

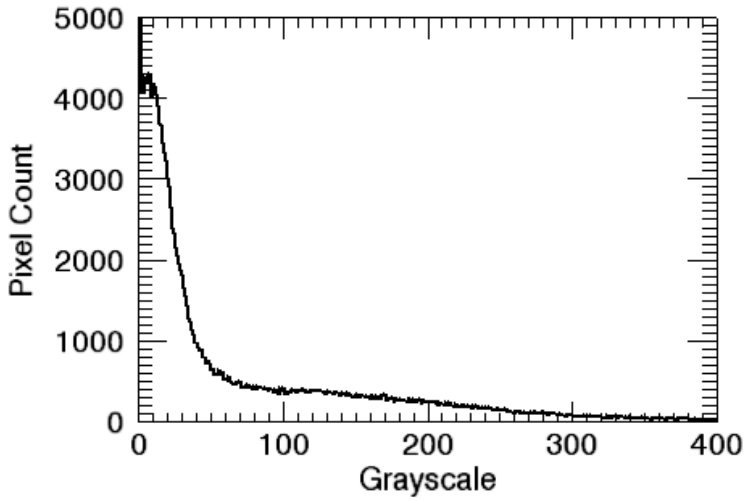

Figure 4-44. Histogram for CT image of liquid flow via subtraction, from which a threshold grayscale of 50 was chosen.

Figure 4-45 shows the dependence of surface area on threshold grayscale for both dry packing surface area and the surface area of the water shell extracted from CT images

obtained under flow. The surface area of structured packing does not depend on the threshold value to the extent that the water shell surface area does. As a lower threshold value is specified, the surface becomes larger, and computational time increases dramatically.

Based on observations of the image histograms and isosurface components at different thresholds, the values of 150 and 50 were chosen for packing and water, respectively. For water, it seems sensible to go to the lowest possible grayscale to include as many partial volume and partial time pixels as possible, with the limit approaching the characteristic grayscale of air in addition to flow artifacts. For packing, choosing a smaller grayscale will eventually only make the packing isosurface appear thicker and begin to include artifacts.

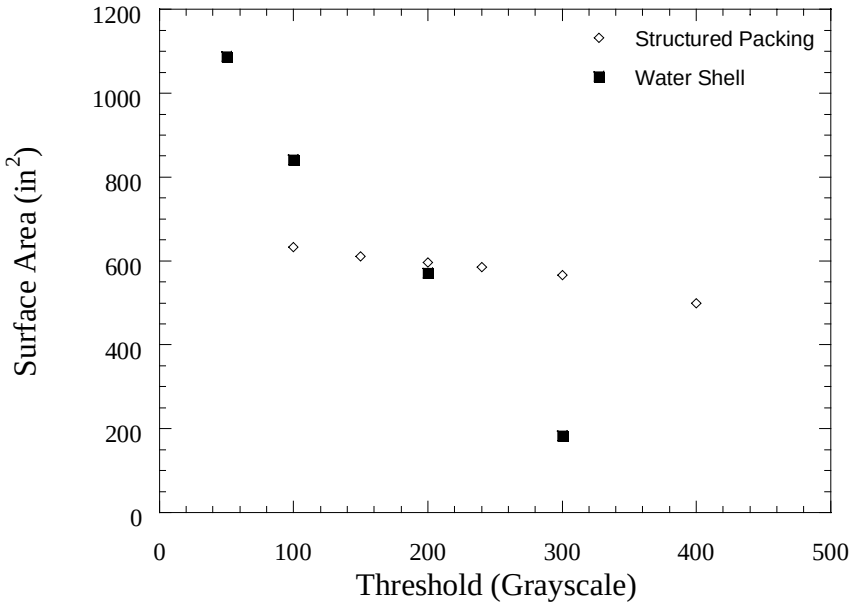

Figure 4-45. Dependence of surface area on threshold grayscale for structured packing and liquid shell.

Determination of the expected surface area for the structured packing involved more than using the vendor specified value. The surface area calculated from the isosurface would contain some area due to the wiper band. However, not all of the wiper band area would contribute to the surface due to loss during the cropping procedure. Sulzer Chemtech, supplier of the packing, does not include the wiper band area in the specified surface area. Also, area lost due to perforations is not accounted for in the vendor supplied surface area value of 250 m^2/m^3. A correction was applied to account for lost area, with the value chosen as the true value of the packing sheet surface area to be 85% of the vendor specified value. The additional area provided by the wiper band was calculated based on the geometry of the band, which was added to the vendor specified area twice to account for both sides of the band. The resulting expected area totaled to 612.5 in^2 for the 3.9-inch tall section being considered, which equates to a specific surface area of 238 m^2/m^3. The area measured from the isosurface created using a threshold value of 150 was 610.5 in^2, which is within 1% of the expected surface area. Obviously the agreement could change based on the choice of threshold, but the variation in area from thresholds from 100 to 240 was still within 5% of the expected value. Figure 4-46 shows the isosurface created with a threshold value of 150.

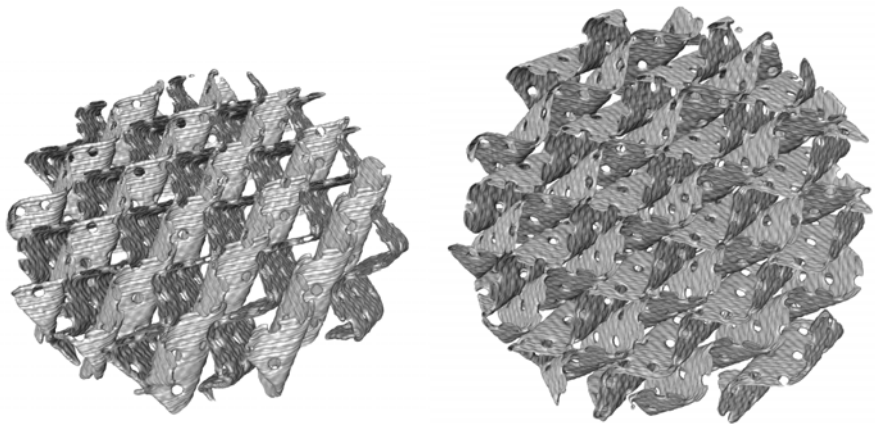

Figure 4-46. Views of an isosurfaced half element of Mellapak 250Y using a threshold grayscale of 150.

When the water isosurface was created using a threshold grayscale of 50, the resulting surface resembled the shape and structure of the packing element itself, indicating that the majority of the liquid flow through the bed is on the surface of the packing as a film. However, particularly near the bottom of the shell, accumulations of liquid were surfaced inside the flow channels. It is this liquid that represents the portions of increased holdup near the packing element joint that could not be resolved using the standard image stack approach. The total surface area for the water shell was calculated to be 1088 in^2.

In order to directly compare this value to experimental data for fractional area, it is necessary to apply certain assumptions. First, the surface area measured by isosurfacing the CT images that resulted from the subtraction of dry CT slices from flow CT slices is the entire surface area of the liquid shell. However, if film flow is assumed throughout the packed bed, then the interfacial area can be presumed equal to one half of the total liquid surface area measured. The thickness of the film is assumed to be small, meaning that area on the edges of the film is negligible compared to the free surface area.

Also, one side of the liquid film remains in contact with the metal packing surface and therefore does not exhibit an interface with the vapor phase. This accounts for the factor of one half. The second caveat is that, when comparing the area obtained from isosurfacing to experimental data collected for the absorption of carbon dioxide into a dilute aqueous solution of sodium hydroxide, some deviation should exist. The absorption technique measures the reactive area, which due to flow in the system, may not be the same as the interfacial area on the packing surface.

A composite image showing the liquid isosurface overlaid in blue on a 1-inch tall 3-D image stack reconstruction of dry packing is provided as Figure 4-47. The angled view down the flow channels confirms that some liquid accumulates between the packing sheets, either due to variation in flow pattern or from liquid holdup associated with the packing joint. The surface tension effects associated with water can be observed where the liquid meniscus is visible in the valley of several channels. The blue areas indicate regions where liquid existed for a long portion of the scan. Areas that do not show blue could have contained water, but likely for only a small portion of the scan time.

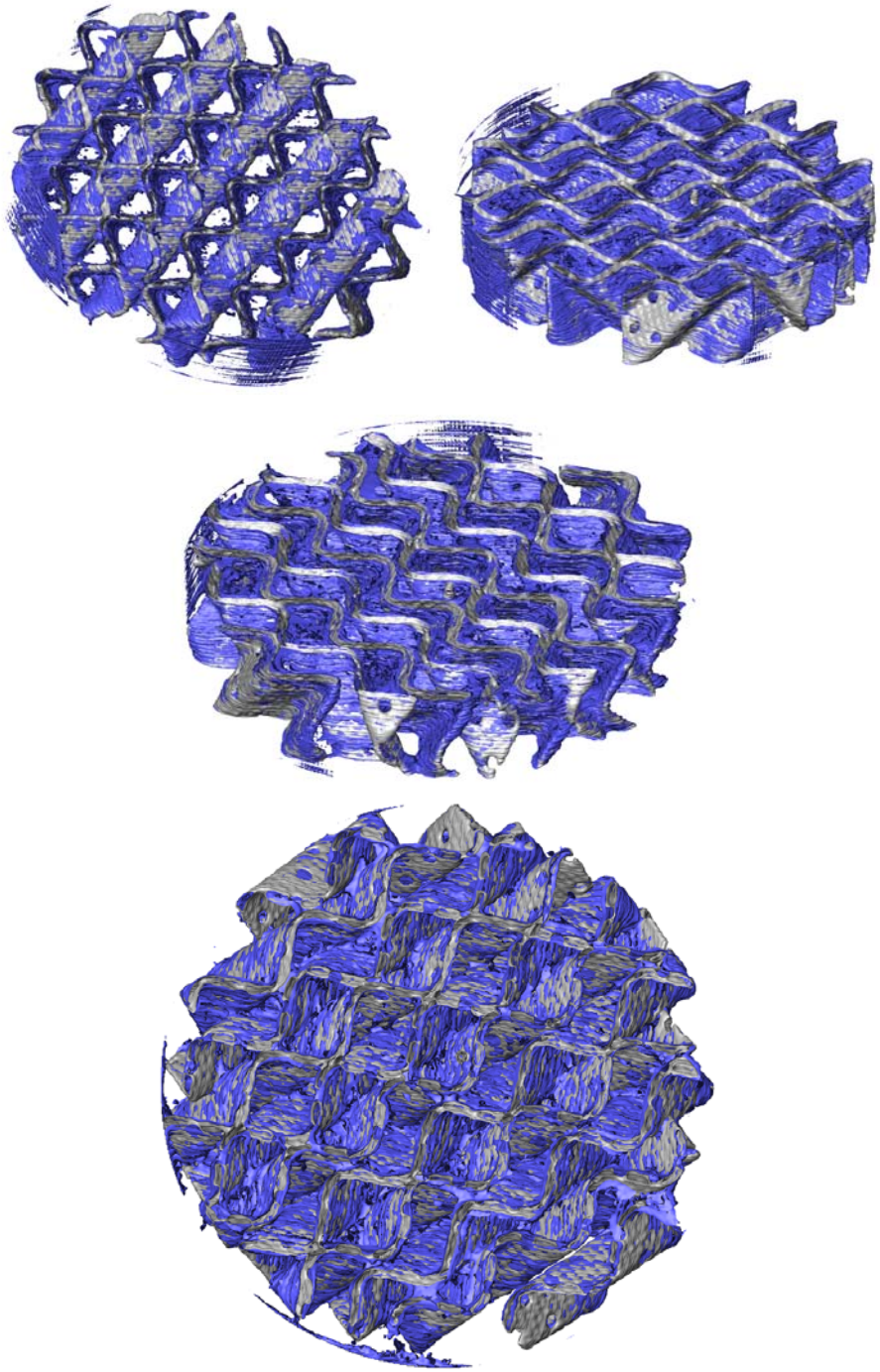

Figure 4-47. Liquid layer isosurface overlaid on dry packing image stack. Liquid rate is 15 GPM/ft^2 and vapor F-factor is 1.3.

Packing near the middle of the column appears to be wetted to a greater extent than packing near the column wall. In the top down view, the blue areas appear to exhibit a wavy texture similar to that seen in Figures 4-38 and 4-39, supporting the claim that the wavy texture is indicative of flow. Liquid branching near the contact points of the packing sheets is evident in the side views. The top down view also lacks perforations in the center of the column, yet they appear near the perimeter of the packing. This suggests that perforations could be intermittently covered by liquid flow as was previously suggested.

The measured area for the liquid shell was converted to fractional area by first dividing by two under the assumptions stated previously. The resulting value for interfacial area was divided by the packing surface area calculated from the isosurfaces of dry CT images. The isosurface data was plotted along with fractional area calculated from absorption experiment data and three predictive models for effective area. The isosurfaces predicted a fractional area of 0.89, which was within 2% of the experimental values obtained using the CO_2 absorption method. None of the models accurately fits the experimental data. The model of Billet & Schultes and the Rocha-Bravo-Fair correlation both severely underpredict fractional area. The results of the comparison are shown in Figure 4-48.

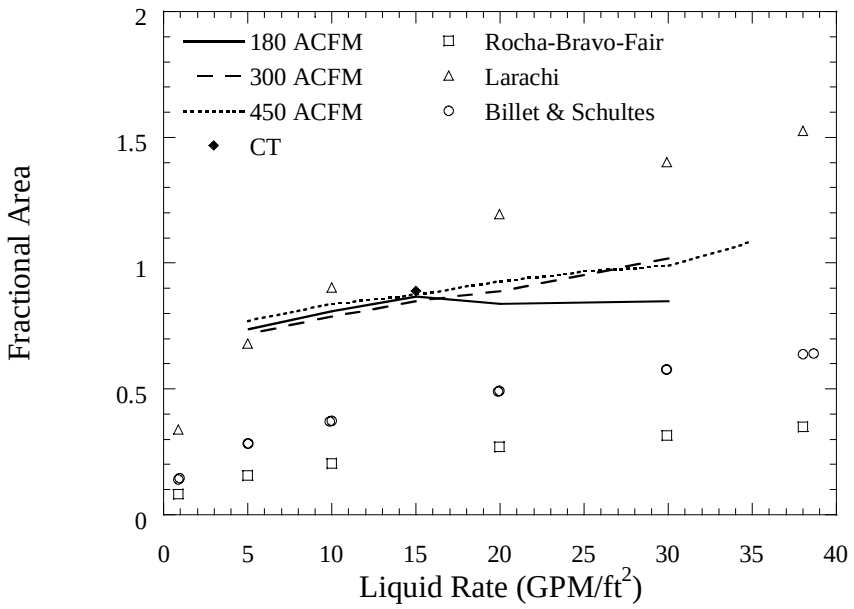

Figure 4-48. Comparison of experimental values and model predictions for fractional area in Mellapak 250Y.

4.6 Stationary Transmission Measurements

To evaluate the variation of flow within the column during a CT scan and quantify noise in the measurement system, a series of stationary transmission measurements were executed using the GE scanner. The intensity of X-rays passing through the column was measured across the detector bank over a 30-second period at three different elevations in the column. The object was not moved during the scans, which were performed for a variety of operating conditions. The data was recorded as an image, where each column represents a single detector, and each row one time step. Each pixel in the image is assigned a grayscale according to the X-ray intensity recorded by a given detector at a given time. The procedure is analogous to taking consecutive radiogram slices at a specified elevation. Data was sampled at 60 Hz, providing 1800

time steps in a 30-second scan. The time period used is approximately equal to the time required to obtain data for one CT slice, without the unwinding step.

The measurements were taken at elevations of 26.25, 19.00, and 12.25 inches, which correspond to the top portion of the top packing element (1), the joint between packing elements 2 and 3, and the bottom portion of the bottom element (4), respectively, as seen in Figure 4-22. Packing element 4 contained a wiper band in the region imaged at the lowest elevation. Measurements were taken for a dry case where no flow was applied to the column, and a flooded case where the column was full of water, in addition to three liquid flow rates and two vapor flow rates. The measurements for the flooded condition were only taken at the lowest elevation.

A sample of the image formed by transmission data is shown in Figure 4-49. Detectors 406-606 correspond to the X-ray paths through the column. The two bright columns in the middle of the image represent two of the column's four stainless steel support rods, measured by detectors 496-503 and 508-516. To the left of the column is the water outlet hose, and to the right is the air inlet hose. Columns that show no variation in grayscale from top to bottom indicate that nothing along that particular X-ray path changed during the course of the scan. Variation due to liquid flow is visible in the region of the image that represents the column interior.

Figure 4-50 shows the average attenuation measured at each detector over the scan period for three different cases at the lowest elevation. Dry, flooded, and flow cases are presented, along with the standard deviation for the flooded and flow conditions. Spikes in the attenuation and standard deviation are apparent due to the metal support rods on both sides of the column and near the center. The parabolic profile of the flooded case is indicative of the fact that X-rays passing through the middle of the column encounter more liquid than those that pass through the outer regions of the column, where

the chord length is shorter. For the dry and flow cases, the average attenuation follows much the same pattern across the detector array. However, the flow case values are of higher grayscale, which is expected as the presence of water in the column increases the average attenuation along ray paths through the column.

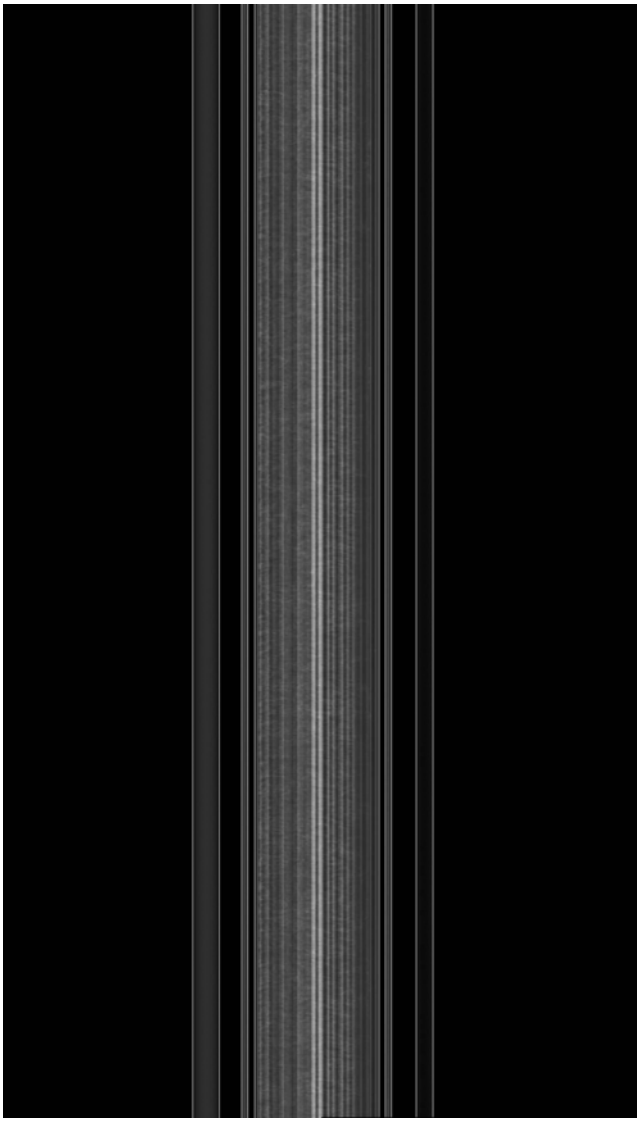

Figure 4-49. Sample image obtained during stationary transmission measurement.

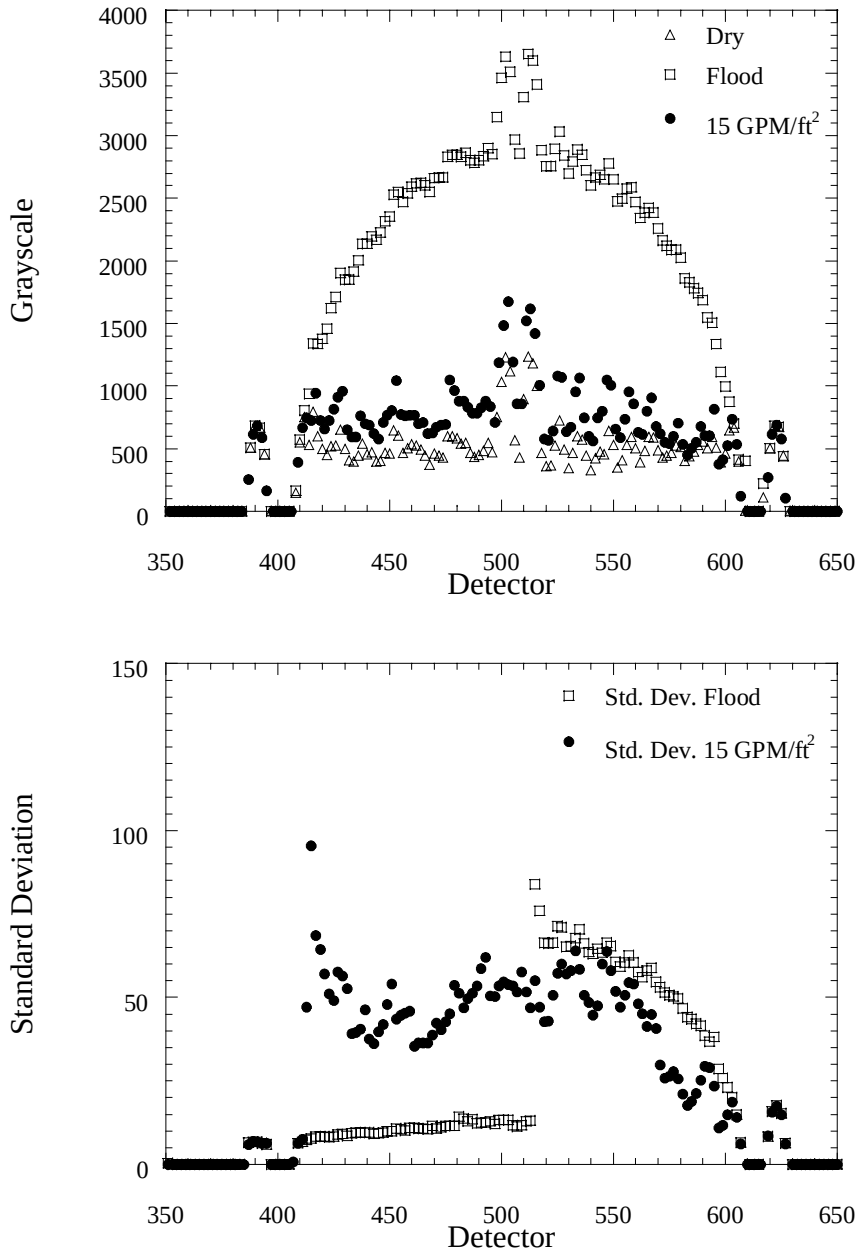

Figure 4-50. Average attenuation measured over a 30-second period and standard deviation for dry, flooded, and flow conditions at elevation 3. Liquid flow is 15 GPM/ft^2 and vapor F-factor is 1.5.

When analyzing the standard deviation for the flooded and flow cases, it is apparent that the flow case exhibited greater variation across the width of the column during the scan period. However, the right side of the column, depicted by detectors 510 to 600, shows variation for the flooded case, which was supposedly a static condition. By comparing the average attenuation data in the same region for the flooded case, it appears that the values are slightly lower than the comparable region on the left side of the column. When consulting the scan data for the maximum water condition at selected detectors for the right side of the column, the grayscales had dropped to zero at the last time step, likely due to a scanner error. The standard deviation of the flow measurements within the column region ranged from 2-9% of the average grayscale value.

The average transmission values can also be used to investigate the degree of distribution throughout the packed bed. By plotting the average grayscale at each detector for both a flow and dry case at each elevation, the difference between the two data sets can be attributed to liquid flow. For a case where the two lines overlap, it can be assumed a small amount, or zero, liquid flowed during the scan. Where there is a large difference between the flow and dry case, a large amount of liquid was present for a long period of the scan. Figure 4-51 shows this phenomenon for the case of a liquid flow of 15 GPM/ft^2 and a vapor F-factor of 1.3. For elevation 1, the liquid appears to be primarily in the middle of the column. Near the left side, there is little difference between the average grayscales of the dry and flow conditions. At the middle packing element joint shown by elevation 2, the distribution has improved. The increased liquid at elevation 2 may be attributed to holdup at the packing element joint. However, some regions still appear where little difference is seen between the dry and flow cases. Finally, at elevation 3, the liquid appears at all locations in the column, with the line representing the flow data consistently above the line for the dry case. The effect is most

noticeable in the middle of the column, where X-rays pass through more area available for liquid flow.

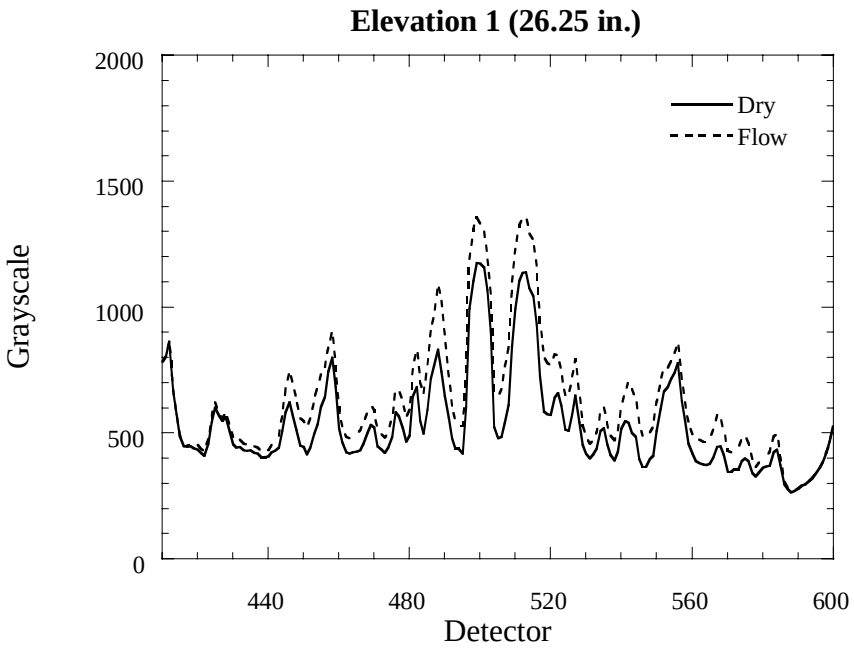

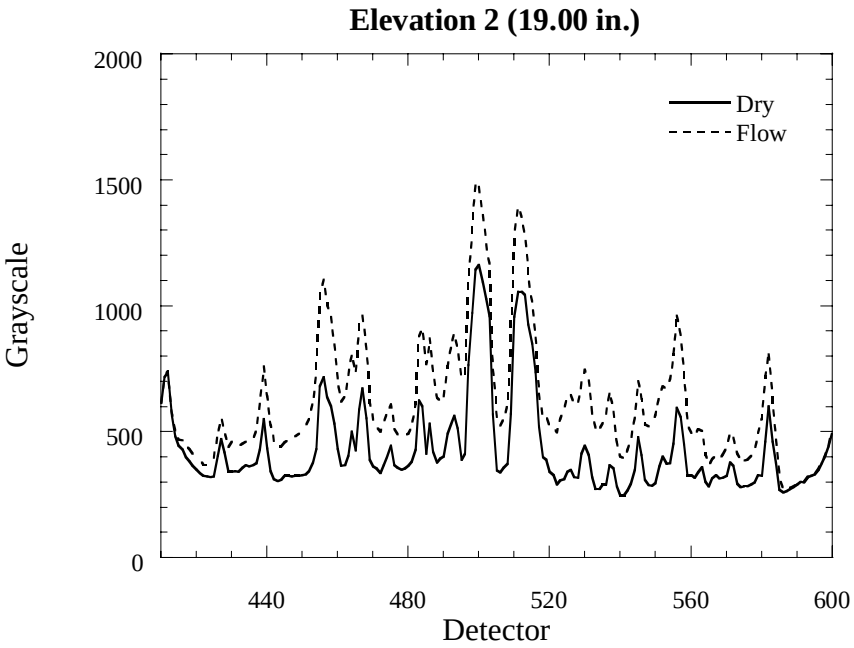

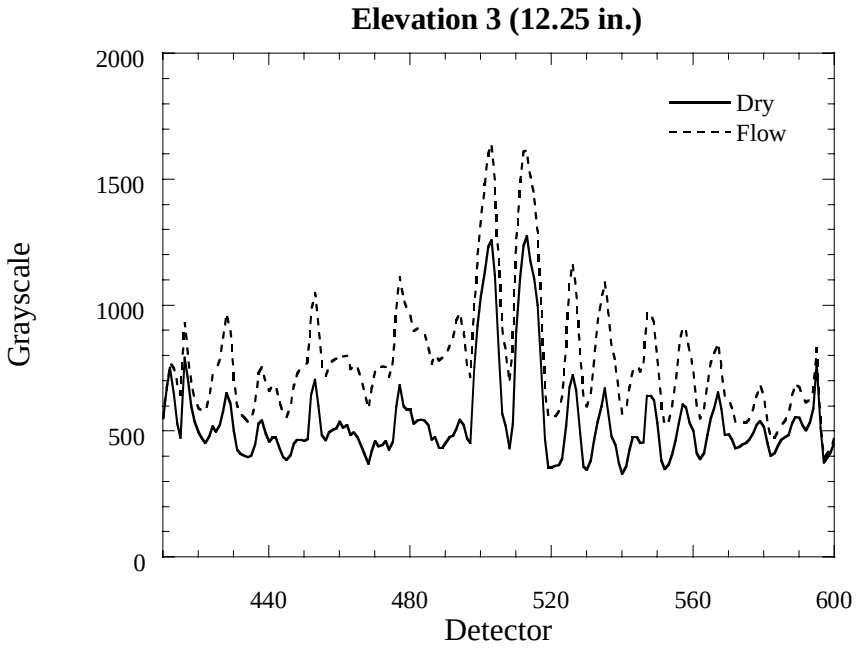

Figure 4-51. Average grayscale for detectors in column region, dry and flow, at each elevation. Liquid flow is 15 GPM/ft^2 and vapor F-factor is 1.3.

To evaluate measurement noise, the detectors in the region outside the column and hoses were considered for the dry and flooded cases. Using these data sets allows analysis of variation due to humidity changes that result from the saturated vapor flow leaving the column. The average grayscale in the air only regions on either side of the column was less than 2. Some spikes were observed in the average values and confirmed by looking at the transmission data image. The spikes were caused by a detector error at one of the 1800 time steps. However, for the flooded case, the average grayscale in the air region was 0, with a standard deviation of 0. Thus, when the scanner operates normally the measurement noise is practically non-existent. Yet, due to random anomalies in detector performance, measurement noise is still a consideration for the GE scanner, particularly for long-duration scans.

Several different regions of interest were identified for further analysis of the transmission data. Table 4-1 lists the various names given to the regions and the column of transmission data (detector) they refer to. Since the column does not move during data acquisition, the data for a given detector within the column region can be compared at different elevations. However, the vinyl tubing for the air and water lines will be in different positions at each elevation.

Table 4-1. Detector Definitions for Transmission Data

Name of Region	Detector	Description
Air 1	310	Air region left of column; includes water outlet hose at Elevation 3
Column 1	406	Left edge of column
Column 2	431	Left side of column
Column 3	456	Left center of column
Column 4	481	Left center of column
Column 5	506	Center of column, between support rods
Column 6	531	Right center of column
Column 7	556	Right center of column
Column 8	581	Right side of column
Column 9	606	Right edge of column
Air 2	690	Air region right of column; includes air inlet hose at Elevation 3

Figure 4-52 shows the grayscale representing attenuation for selected detectors during the course of data acquisition under conditions of no flow at elevation 1. Clearly there was a spike in grayscale at all detectors near t = 3.5 seconds. This is most likely a scanner or detector error. The grayscale of the Air 1 detector was constant at zero except during the error.

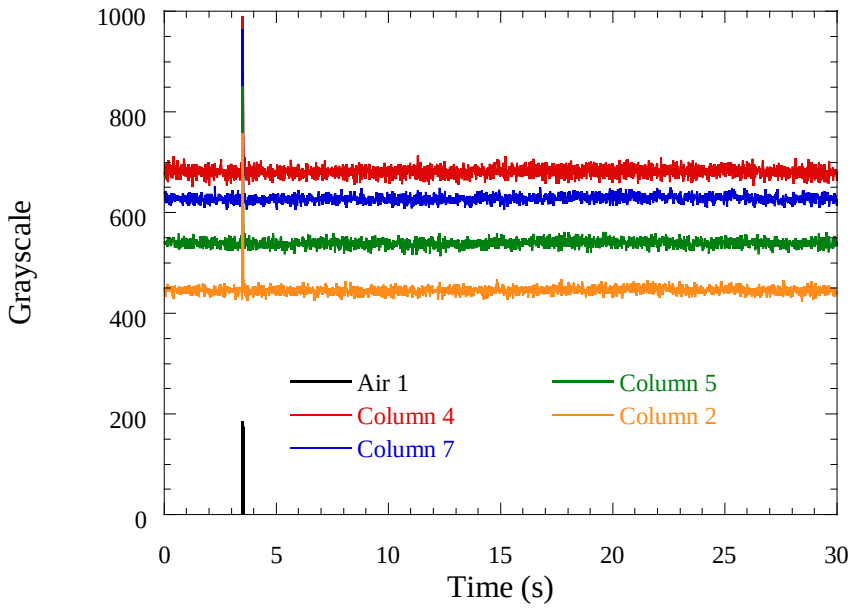

Figure 4-52. Stationary transmission data under no flow for selected detectors at elevation 1.

The transmission data, while high in frequency, is relatively tight around the average grayscale for a given detector. Since no flow is being applied to the column, the variation is strictly a measure of noise in the X-ray source strength or detectors. Although Column 5 represents the path through the widest portion of the column, it did not exhibit the highest attenuation. The amount of metal packing material encountered along an X-ray path is not that same at each detector; the particular path taken by an X-

ray to arrive at detector 506 may pass through a portion of the packing containing a large number of perforations.

To quantify the variation in attenuation due to flow, the grayscale values observed by a detector can be plotted versus time, as in Figure 4-53. The four detectors selected represent locations both near the column wall and along a diameter. No smoothing has been applied to the data. Columns 2, 5, and 7 exhibit high frequency fluctuation, but the amplitudes are small and the average value is relatively constant. For Column 8, which is near the wall, the fluctuation is still high in frequency, but is much smaller in amplitude. This can be attributed to the fact that little flow reaches the wall, and the X-ray path length through this portion of the column is short. Therefore, less overall liquid is being considered. As the number of packing sheets each X-ray passes through varies by detector, with each ray encountering multiple sheets, pinning down the exact location of flow variation is not possible.

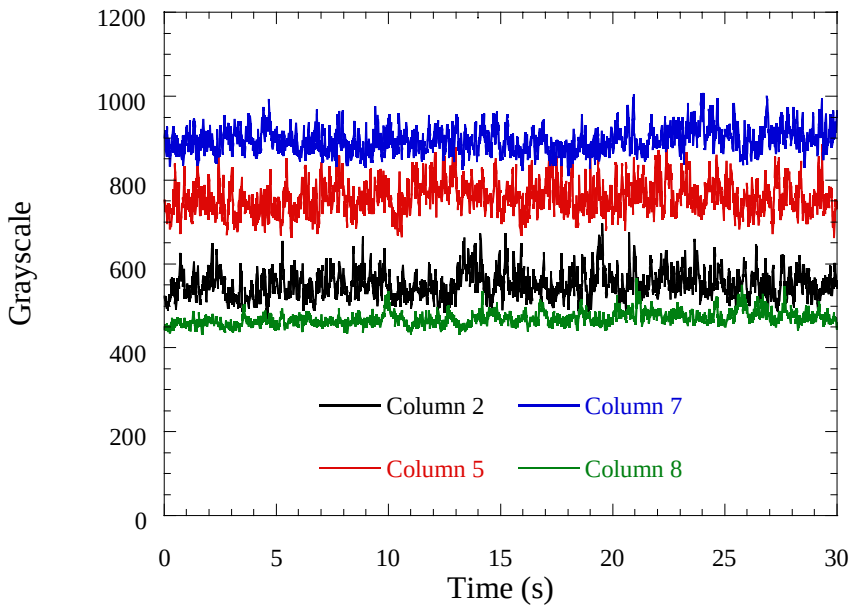

Figure 4-53. Variation in grayscale over time for selected detectors at elevation 3. Liquid flow is 10 GPM/ft^2 and vapor F-factor is 1.3.

The effect of elevation in the column on flow fluctuation is addressed in Figure 4-54. For a liquid flow of 10 GPM/ft^2 and a vapor F-factor of 1.3, the variation in grayscale at the location defined by Column 6 over the scan period is plotted at each elevation. At the highest elevation, the flow does not exhibit large fluctuations as evidenced by the small amplitude of the data set. At elevation 2, the grayscale variation exhibits greater amplitude, but the average value is generally constant. However, in the bottom packing element where elevation 3 data is taken, the grayscale is shown to vary more on both short time scales and overall. At this point in the column, the liquid has better distribution, providing a greater number of flow paths that may vary and contribute to the noisy behavior.

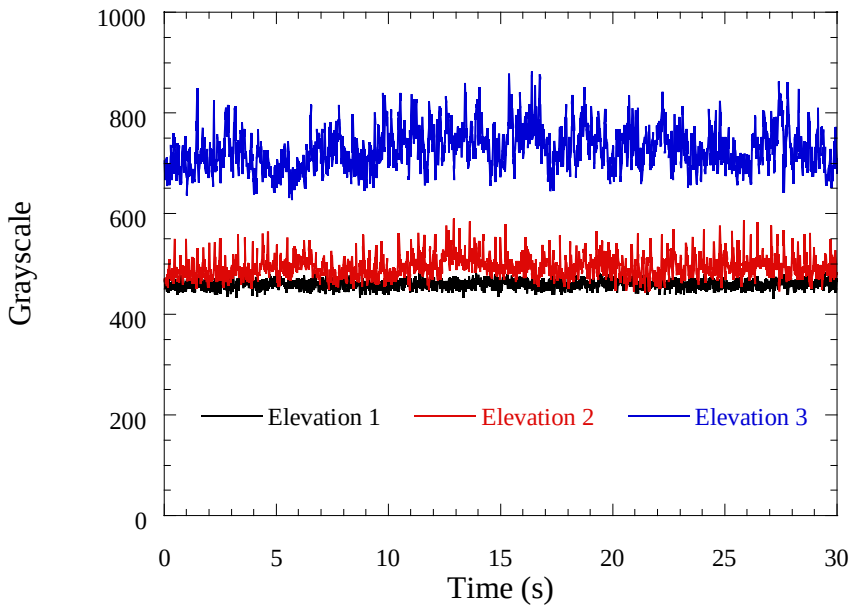

Figure 4-54. Variation in grayscale at each elevation for Column 6. Liquid flow is 10 GPM/ft^2 and vapor F-factor is 1.3.

Figure 4-55 shows the transmission data recorded by the detector defined as Column 4 for liquid flow rates of 5, 10, and 15 GPM/ft^2 at an F-factor of 1.3. All three elevations are shown to compare the flow behavior throughout the column. In the plot showing elevation 1, all three liquid rates exhibit similar noise characteristics and appear to have relatively similar average values of grayscale, signifying the flow behavior near the top of the column to be fairly consistent over the range of all flow rates. At elevation 2, the data continues to be consistent for all flow rates, with a few spikes in the data for 5 GPM/ft^2. The spikes are consistent with measurement noise defined earlier. The amplitude of the variation at elevation 2 is much less than at elevation 1. As elevation 2 is located at a packing joint where liquid is known to accumulate, it appears that the held-up liquid region does not fluctuate as much as the bulk flow, at least along the path line defined by Column 2.

The most interesting result for Figure 4-55 is for the transmission measurements at elevation 3. For the 10 and 15 GPM/ft^2 flow cases, the data exhibits high frequency variation, with higher amplitude than the data at elevations 1 or 2. However, the data for the 5 GPM/ft^2 case has much higher amplitude variation, and also an average grayscale significantly higher than the other flow rates. This is an indication that more liquid is present along the path line for the entire scan, which is not expected for the lowest flow rate considering the flow was shown to be well-distributed. The most likely explanation for the behavior of the 5 GPM/ft^2 case is that the low liquid rate combined with proximity to the vapor inlet results in increased loading or semi-flooding of the bottom packing element. The liquid has trouble exiting the packed bed and is blown back up into the packing channels. Strong vapor flow can also blow the liquid films off the surface of the packing. These behaviors were verified visually as the column was operated.

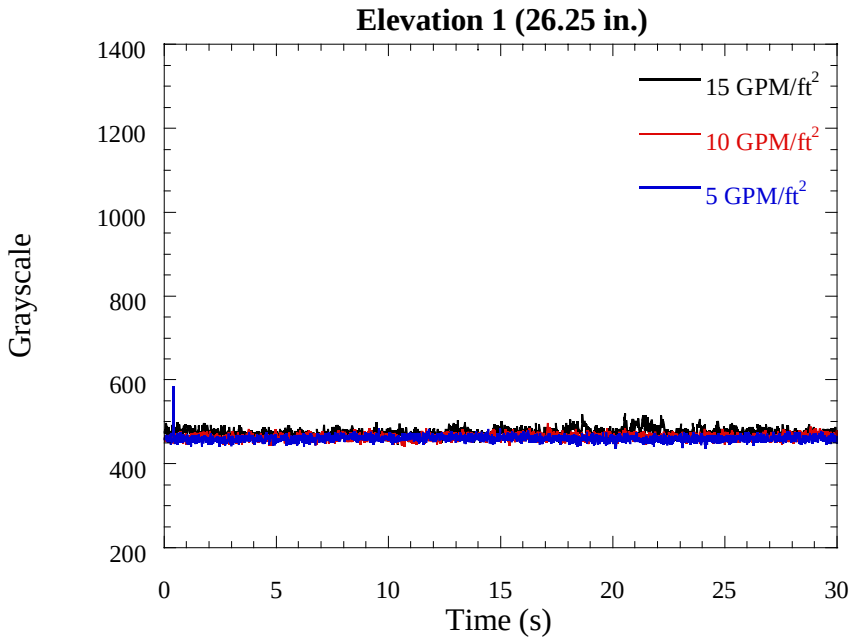
Elevation 1 (26.25 in.)
Grayscale
Time (s)
15 GPM/ft2
10 GPM/ft2
5 GPM/ft2
1400
1200
1000
800
600
400
200
0
5
10
15
20
25
30

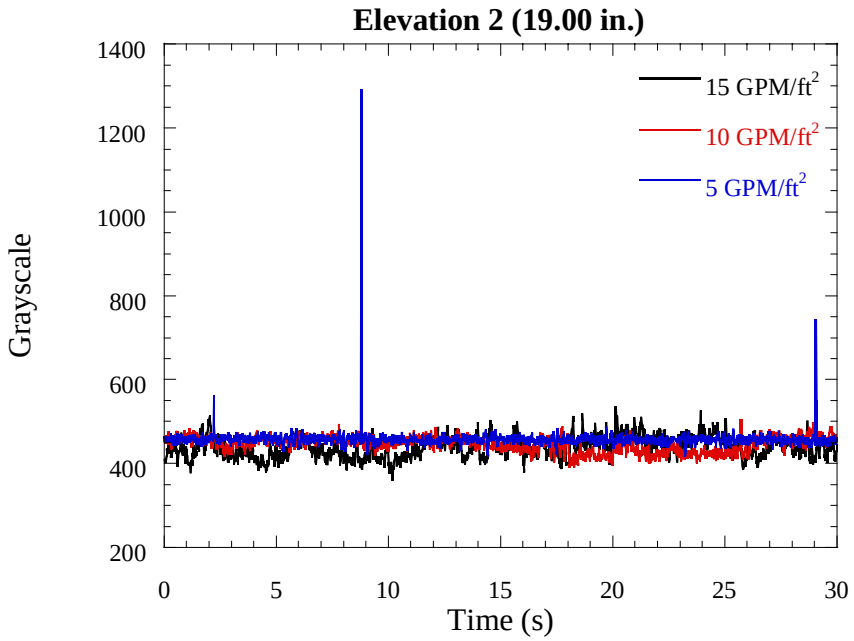
Elevation 2 (19.00 in.)
Grayscale
Time (s)
15 GPM/ft2
10 GPM/ft2
5 GPM/ft2
1400
1200
1000
800
600
400
200
0
5
10
15
20
25
30

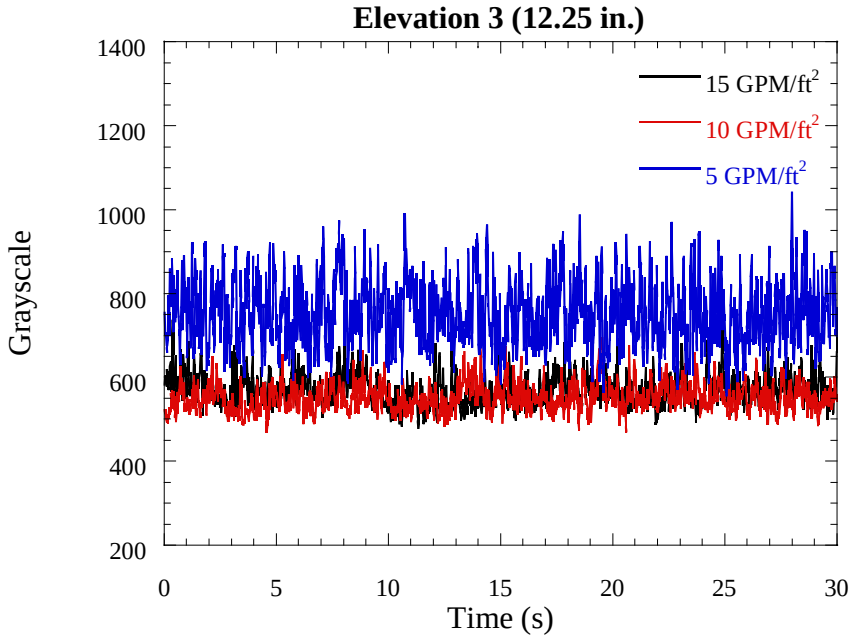

Figure 4-55. Flow rate variation at Column 2 for various elevations.

4.7 Summary

X-ray computed tomography was used to obtain images of an operating air-water contactor containing structured packing. The images were used to quantify hydraulic parameters including void fraction, liquid holdup, and interfacial area. Imaging techniques utilized included radiograms, single CT slices, stacks of adjacent CT slices for three-dimensional modeling, isosurfacing, and the collection of stationary transmission measurements.

Two separate X-ray scanners were used during the course of the experiments. The improved contrast and shortened scan time achieved by moving to a true third-generation machine greatly improved the experimental throughput and data quality. The

acquisition of volumetric data represented a step forward in imaging technology applied to a packed column.

The liquid holdup was found to vary greatly throughout the packed section, with local maximums occurring in the region 0.25 to 0.4 inches above the interface between two packing elements. The holdup in this region could be as much as 2 to 5 times the holdup observed in the bulk of the packing element. The values of holdup obtained by CT compared favorably to traditional experimental methods when averaged over the entire column, yet no existing predictive model was successful in predicting holdup behavior.

The surface area of structured packing and the interfacial area between liquid and vapor were evaluated using X-ray CT. Surface area measurements were within 1% of the value expected when adjusting the vendor specified value to account for perforations and wiper bands. The interfacial area was determined by applying assumptions regarding film flow on the corrugated packing sheets. The fractional area derived from the measured surface and interfacial areas agreed within 2% of experimental data obtained using a chemical absorption technique.

CHAPTER 5: CONCLUSIONS AND RECOMMENDATIONS

The studies presented measured the hydraulic performance of an operating air-water contactor containing structured packing using X-ray imaging techniques. Two X-ray CT scanners of different geometry were used to evaluate the image quality improvement when a true third-generation machine was used to image liquid flow in a packed bed. Objectives that were met by this work included measuring the void fraction and liquid holdup on a local level within the packed section, determining the gas-liquid contact area from a series of CT slices, and evaluating the flow variation within the column and measurement noise. These goals were met by analyzing reconstructed CT images rather than X-ray transmission data. The reduction or elimination of image artifacts related to flow and data acquisition procedures was accomplished.

Collecting a snapshot of the internal phase distribution of a vapor-liquid contactor is the ultimate and ideal goal of performing imaging studies of such devices. A series of three-dimensional images taken over time would provide a great deal of information about the time variance of flow. Parameters necessary to accurately predict the hydraulic and mass-transfer performance of vapor-liquid contactors, such as liquid holdup at any location in the packed bed, the interfacial area between vapor and liquid, the quality of liquid distribution, and the fractional coverage of the packing area, could be extracted from such images and applied to the development and validation of advanced column performance models. Identification of an optimal operating point would be possible if such data were available over the entire operating range. This approach also has the potential to describe how physical properties of the system as well as the operating pattern contribute to the overall behavior. Contactors could be designed more efficiently,

particularly in terms of column internals, if a more basic and fundamental understanding of the factors affecting operation is acquired. Such an approach would constitute a significant improvement over the current semi-empirical approaches that are used to design and predict the performance of vapor-liquid contacting devices.

In light of the results achieved in this study and other works that have applied non-invasive testing methods to process engineering problems, it is expected that such technologies will become more widely used in the future as a tool to complement advanced modeling and computer simulations. Process tomography continues to improve and show promise of becoming the non-traditional experimental technique of choice when it comes to collecting the data necessary to validate improved modeling efforts. Non-intrusive measurement of a variety of process parameters at a local scale is possible. The current technology is on the verge of making volumetric data acquisition in a short time period possible using flat-panel X-ray detectors paired with cone-beam X-ray sources. Succeeding at accurately measuring 3-D data will make X-ray CT an extremely robust option for process measurement when combined with the existing ability to obtain 2-D cross sectional images at a desired location.

5.1 Conclusions

The experiments performed in this study successfully measured the local void fraction, liquid holdup, and liquid distribution characteristics using image analysis of 2-D CT images and 3-D models created from image stacks. X-ray CT is a valid method for measuring these quantities from an operating vapor-liquid contactor. The interfacial area exhibited by water and air at a vapor F-factor of 1.3 and a liquid flow rate of 15 GPM/ft^2 was calculated by fitting a surface to a 3-D model constructed from liquid-only

subtraction images. The parameters investigated affect both hydraulic and mass-transfer characteristics observed in vapor-liquid contacting applications such as distillation.

Two X-ray scanners were employed to obtain the CT data. The 3DID scanner first used required subpositions during data acquisition. The GE scanner utilized a continuous detector array, eliminating the need for subpositions in the data collection process. The presence of image artifacts was greatly reduced in the images acquired using the GE scanner, confirming the hypothesis of Schmit [56]. It is critical for future imaging studies to, at a minimum, utilize a true third-generation scanner with a continuous detector array in order to produce data with minimal artifacts that can be analyzed quantitatively with confidence.

Void fraction and liquid holdup were calculated from CT images of Mellapak 250Y. The void fraction was shown to vary with elevation due to the wiper bands and perforations on packing sheets. The value calculated from CT experiments was within 1% of the vendor-supplied value. Liquid holdup was also shown to vary with elevation. The values calculated from CT image subtractions were within 20% of the holdup measured using traditional experimental techniques. Error in the holdup calculation can be attributed to the tedious nature of identifying regions of liquid in the images, along with partial-volume and time-dependent characteristics of liquid regions. A clear relationship was observed between the void fraction profile and the liquid holdup profile in the bulk of a packing element. This phenomenon should be exploited when future designs for packing are developed.

Increased holdup was observed in the region slightly above the interface between adjacent packing elements. The liquid accumulation caused holdup to be two to five times higher than the holdup in the element bulk for a region 0.25 to 0.4 inches above the interface. The joint region is clearly the bottleneck point for columns containing

structured packing. Due to the imprecise nature of installing structured packing, void regions between adjacent elements are commonplace. Discontinuities in packing surface result in liquid maldistribution. Adjusting the design of packing elements to provide a more secure fit at the interface can improve the performance of both standard and high capacity packings, which can be verified using X-ray CT. Large diameter columns employ bricks of packing that are designed to fit through manways before being installed together in layers. It is suspected that liquid holdup variations similar to those observed between packing layers will be observed at the interface between adjacent bricks. Thus, improved connectivity of packing portions, both at the layer interface and within a layer can potentially improve column performance.

Stacks of CT images provided a 3-D representation of dry packing, irrigated packing, and a liquid-only "shell." The liquid distribution was qualitatively described using the 3-D reconstructions. The 2-D images used to create the models permitted void fraction and liquid holdup profiles to be plotted for a continuous section of the packed bed. The averages of both measurements were compared to vendor supplied values and traditional experiments with good agreement. Radial variation of liquid holdup was not observed qualitatively when CT images at different elevations in the column were considered. The design of structured packing produces superior radial distribution compared to random packing without the need for mid-bed redistributors provided the initial liquid distribution is good. However, the axial holdup varied greatly, especially in the joint region. Liquid holdup exhibited a sinusoidal pattern in the bulk of a packing element.

While current models include parameters describing the packing, they treat the bed as one large element. Until performance models account for the axial variation of holdup by including a correction term for the number of joints in the packed bed, the

liquid holdup will not be accurately predicted. Using X-ray CT to measure the improvement provided by high capacity structured packings will confirm whether a joint correction term is required for modeling performance of all structured packings, or only a select few based on their design at the interface. Additionally, the holdup profile at the interface suggests that the design at the top of an element is not as important as the design at the bottom. A hybrid design that combines high capacity joints at the top of an element with traditional interface treatments at the bottom could provide a cost-effective measure of improving performance. Again, process tomography can supply answers to such questions.

Three-dimensional reconstructions were used to fit surfaces to dry packing and the liquid flow pattern observed in the column. Surface area was calculated from the isosurfaces, with the surface area of dry packing falling within 1 to 5 percent of the expected value, depending on the threshold grayscale used. The interfacial area between water and air was calculated using a threshold technique and compared to experimental measurements of reactive area in a carbon dioxide absorption system, as well as existing correlations for effective fractional area. The interfacial area from CT images was divided by two under the assumption of film flow. The resulting value provided a fractional area within 2% of the value obtained on the SRP air-water column during absorption experiments. The choice of threshold grayscale requires histogram analysis of the characteristic grayscale values for the phases present in the images to avoid becoming too arbitrary.

The threshold technique to measure interfacial area is not perfect. More detailed image processing analysis will more clearly define the location and thickness of liquid films in a piecewise fashion to ensure continuity. Calculating the edge response function of liquid films on the packing surface and then stacking the results from multiple slices

uniquely describes each region of the packing. This will help decouple the air and liquid phases. Ultimately, a quicker picture with greater resolution is required to define liquid film thicknesses and evaluate moving rivulets with precision.

Measurement noise and flow variation were evaluated using time-dependent measurements of X-ray transmission while the column remained stationary. Signal variation along several X-ray paths indicated that the flow variation was high in frequency but low in amplitude, with the exception of the bottom packing element at certain flow rates, where increased variation was observed. Measurement noise in the air region was virtually non-existent. Scanner drift was observed during a 10-hour acquisition of data for a 3-D model, with the overall percentage change over time being small compared to the available range of grayscales. Extra air calibrations could be performed intermittently during long scans to address the issue. The spatial resolution that makes X-ray CT desirable when investigating performance throughout the object's cross-section makes it a poor tool for evaluating the short-term variation of flow, as the precise location of variations can not be pinpointed using stationary transmission measurements alone.

5.2 Recommendations for Future Study

5.2.1 Improvements to Equipment

X-ray imaging techniques continue to show promise in measuring local- and bulk-scale hydraulic parameters that play an important role in predicting the performance of vapor-liquid contactors. The GE scanner provided superior images compared to those obtained using the 3DID scanner. Future imaging studies should be performed using a scanner of at least a third-generation geometry to avoid image artifacts detrimental to

quantitative analysis. The following recommendations should be considered if further imaging studies are carried out, or if construction of a custom CT scanner becomes an option.

While 2-D CT images are valuable for determining the local void fraction at a given location in the packed bed, using stacks of 2-D slices to create 3-D models has several limitations, the greatest of which is the required scan time. To achieve quality spatial resolution, the slice thickness is reduced, which in turn increases the number of slices required to model a given section of the object. The use of volumetric CT, where a flat-panel area detector records data for a large region of the object with just one revolution, is certainly preferred. Scan times could be reduced from hours to seconds. The resulting time averaged flow becomes much closer to the instantaneous snapshot that is desired. Some issues with volumetric CT are still being addressed. The image reconstruction algorithms required for cone-beam X-ray sources are more complex than those used with fan-beam sources in 2-D CT. The understanding of scaling in the reconstructed images also needs to be improved if extraction of quantitative measurements from the data is intended. However, for these experiments to become reality, it is necessary to improve the robustness of current flat-panel detectors, as there are issues with detector lifetime when high-energy X-ray sources such as those used in this work are used.

Reducing the scan time through the use of an alternate scanner or through modification of the existing GE scanner is highly encouraged. The current procedure, which requires rotation followed by counter-rotation, can be improved. If the scanner data acquisition code can be modified to allow collection of data during the counter-rotation, the effective total scan time can be cut in half. Increasing the rotation speed during data acquisition is not recommended as it has potential to impact the internal

flows. Without question, using a scanner that rotates the source and detectors around the object as opposed to rotating the object itself would ensure that flows were not being affected by the scanning procedure.

An alternative to improving the rotate and counter-rotate acquisition procedure would be to eliminate the need to counter-rotate altogether. Adjustments to the design of the hoses carrying feed to and effluent from the column could eliminate the potential of hoses tangling. Regardless of the hose management design of the top of the column, it is recommended that the lines carrying the water out of the bottom of the column and feeding the air into the column be converted from vinyl tubing to some type of rigid material, preferably stainless steel, at least in the region from the fittings on the column base to the top of the packed section. Movement of the hoses while the column rotates creates image artifacts that will appear throughout the reconstructed image, including the column interior, complicating analysis. Installing a more permanent piping system also ensures that regions known to contain only air or water will be present in the same location of every CT image. This will prove valuable for determining the characteristic grayscale values of those materials at any given slice, and thus time, during the scan. In addition, relocating the airflow control needle valve outside the scanning bay would increase experimental throughput, eliminating the need to pause experiments and enter the scanning bay to change the air rate.

As seen from the stationary transmission measurements, the interaction between vapor and liquid in the bottom packing element differs from patterns observed in the rest of the column. As it exists, the vapor inlet and distributor are located too close to the bottom of the packed section. Increasing the distance between the vapor distributor and the packing would reduce the potential for flooding in the bottom element and ensure that the vapor flow is allowed to fully distribute itself. In addition to relocating the vapor

inlet, enlarging the sump at the bottom of the column would reduce the variability of liquid flow in the closed loop. Reducing the interaction between incoming vapor and the liquid level that is maintained in the sump should also be considered during a redesign.

5.2.2 Suggestions for Future Experiments

Much experimental downtime limited the studies performed in this work to a single chemical system and limited varieties of structured packing. To fully establish the applicability of X-ray CT to the imaging of multiphase flow in a packed column, additional studies should be performed that determine the effect of system physical properties and packing design on operation. Specifically, a liquid phase that exhibits a more hydrocarbon-like surface tension should be imaged. Images can be produced that show the effect of surface tension on the degree of wetting and the flow pattern, particularly in the valleys of the corrugated sheet flow channels. Furthermore, calculation of the interfacial and fractional areas will prove noteworthy. Using X-ray CT to correlate measured interfacial areas with liquid physical properties such as surface tension and density could potentially be applied to extend the applicability of pilot-scale measurements of active area that use absorption techniques relying on an aqueous liquid phase.

The ideal fluid would exhibit surface tension, viscosity, and density similar to hydrocarbons, but also would be non-flammable and possess a low vapor pressure. Such materials exist, namely the Novec series of engineered fluids produced by 3M, with the HFE-7500 heat transfer fluid showing much potential. The existing recycle configuration of the flow system permits easy adaptation to a new fluid, although loss of liquid through evaporation and entrainment over time should be considered, particularly for a non-aqueous liquid phase.

Past studies have doped water with a supplemental material intended to increase the X-ray attenuation to improve the contrast between phases in images. The linear attenuation coefficient of a material decreases exponentially with increasing X-ray energy. Thus at the high X-ray source energies used with the GE scanner, the benefit of a more attenuating fluid would be minimal at best, particularly in light of the very thin liquid films on the packing surface that only occupy a small fraction of a pixel.

In terms of column internals, packings that have been modified to increase the hydraulic capacity utilize a modified structure at the top and bottom of the element. Examples include Sulzer Mellapak Plus and Flexipac HC by Koch-Glitsch. The designs are intended to reduce the accumulation of liquid at and above the packing element interface. Using X-ray CT to map the liquid holdup profile across the joint region can provide a quantitative measure of the enhancement provided by such packings when compared to the data contained in this work for Mellapak 250Y. Operating the column at higher vapor rates approaching the flood point and evaluating the liquid flow pattern, distribution, and holdup can supply additional data for comparison.

The subject of packing design calls to light the robustness of the X-ray imaging technique used in this work. The process of developing and testing improved column internals has previously been time consuming and expensive, requiring fabrication of prototypes and extensive benchmark testing. The availability of a computerized tool for design and simulation would greatly reduce the cost of product development, allowing new designs to be quickly constructed using engineering software and tested within an accurate simulation environment. Favorable results can provide the green light for prototype construction and evaluation using physical experiments. X-ray CT is a valuable tool for obtaining the local- and bulk-scale validation data required to make these advanced simulations possible.

However, complicated simulations are computationally intensive, sometimes requiring weeks to solve the systems of equations governing micro-scale behavior in large-scale physical process. Constructing prototypes for testing can sometimes be the faster route, and again X-ray CT can be used to evaluate the performance of advanced column internals nondestructively. The imaging techniques can provide greater insight into local scale behavior than traditional experiments to fully characterize such devices. The technique possesses the ability to provide non-traditional experimental data that drives advanced model development and highlights areas for improved equipment design. With the added benefit of serving as a validation tool at the other end of the process, process tomography will continue to be an attractive and versatile option.

Exploring the capabilities of other X-ray imaging technologies such as particle tracking using a real-time flat panel X-ray detector can potentially provide information about the velocity of phases within the column during operation. This logically extends the current knowledge base of the liquid location to additional properties that are important to include in modeling and validation. Maintaining a partnership with General Electric will continue to provide opportunities to apply a variety of state-of-the-art imaging technologies to vapor-liquid contactors.

5.3 Summary

X-ray computed tomography has been shown to be an invaluable tool for evaluating the hydraulic performance of an operating vapor-liquid contactor containing structured packing. Additional studies have extended the application of process tomography to a variety of process engineering scenarios. However, very few imaging systems have been constructed with the sole purpose of investigating column internals.

The opportunity exists to make significant advancements in several areas of packed column research.

The current state of imaging technology represents a dramatic improvement over the capabilities of systems used even five to ten years ago. Similar improvements in equipment and image processing techniques are expected in the near future. Advancing imaging technology is necessary for the quantification of important parameters affecting packed column performance. However, this work showed current equipment to possess the ability to measure void fraction and liquid holdup on local and bulk scales. A measure of gas-liquid contact area was also obtained using rough three-dimensional image analysis techniques. A more accurate measure of interfacial area is possible with volumetric CT, but improvements in technology are necessary, specifically the lifetime of area detectors when paired with high-powered sources, before this can become a reality.

However, a great number of questions about contactor performance can be answered using existing technology. Quantification of the improvement provided by high capacity structured packings is clearly possible using the liquid holdup analysis techniques presented in this study. The performance of multiple packing types can be benchmarked. Liquid physical properties can be altered to investigate related variations in liquid distribution and flow pattern. The effect of packing sheet perforations, rotation angle, surface texturing, element height, diameter, and initial liquid distribution on packing performance can all be quantified. These are just a few examples of the variety of research that can be carried out using CT imaging as it currently exists, all of which provide valuable data for advanced model development.

By focusing on experiments that can be carried out with existing imaging technology, new questions will arise that can be answered using the next generation of imaging equipment. The development of a custom X-ray scanner designed specifically to

evaluate packed column performance would most certainly be feasible and extremely valuable when high-energy, high-resolution volumetric CT becomes a viable option.

APPENDIX A: CALCULATION METHOD FOR EXPERIMENTAL INTERFACIAL AREA

The following information regarding the calculation of interfacial area from CO_2 absorption has been adapted from Briley [9].

Step 1: Solve for the NTU

$$NTU_{OG} = \ln\left(\frac{Y_{CO_2,in}}{Y_{CO_2,out}}\right)$$

Where NTU_{OG} is the number of transfer units in the gas phase, $Y_{CO_2,in}$ is the ambient CO_2 concentration (ppm) in the inlet stream, and $Y_{CO_2,out}$ is the CO_2 concentration (ppm) in the scrubbed outlet stream.

Step 2: Solve for the HTU

$$HTU_{OG} = \frac{Z_p}{NTU_{OG}}$$

Where HTU_{OG} is the height of a transfer unit (ft) and Z_p is the height of the contacting bed.

Step 3: Solve for $K_{OG}a$

$$\overline{K_{OG}a} = \frac{U_S}{HTU_{OG}} = \frac{U_S}{\left(Z_p \middle/ NTU_{OG}\right)}$$

Where U_S is the superficial vapor velocity (ft/s) and $K_{OG}a$ is the mass transfer coefficient/area combined term (s^{-1}).

Step 4: Calculate the Ionic Strength

$$I = \frac{1}{2}\sum z_i^2 C_i$$

Where z_i is the number of positive or negative charges on an ion having molarity C_i (gmol/L). The number of positive or negative charges in this case is determined by the ions in the solution, Na^+ and OH^-.

Taken from Sherwood et al. [67].

Step 5: Calculate the Henry's Law Constant

$$\log_{10}\left(\frac{H}{H_w}\right) = -\sum h_i I_i$$

Where I is the ionic strength from Step 4, $h = h_+ + h_- + h_g$, and H_w is the Henry's law coefficient for water. Values for h_+, h_-, and h_g can be found in Pohorecki and Moniuk [46].

$$\log_{10}(H_w) = 9.1229 - 5.9044\times10^{-2}T + 7.8857\times10^{-5}T^2$$

Expression for Henry's law constant of water where T is absolute temperature (K).

Step 6: Determine the Diffusivity

$$D_w = -8.1764 + \frac{712.5}{T} - \frac{2.591\times10^5}{T^2}$$

Where D_w is the diffusivity of CO_2 in water at absolute temperature T (K).

$$D_{CO_2} = D_w \frac{\mu_{OH^-}}{\mu_{H_2O}}$$

Where D_{CO_2} is the diffusivity of CO_2 in solution at the absolute temperature used to determine D_w, and μ_{OH^-} and μ_{H_2O} are the viscosities of the solution and water, respectively.

Taken from Pohorecki and Moniuk [46].

Step 7: Calculate the Rate Constant

$$\log_{10}\left(k^{\infty}_{OH^-}\right) = 11.895 - \frac{2382}{T}$$

Where $k^{\infty}_{OH^-}$ is the second order rate constant for the reaction of CO_2 with hydroxyl ion in aqueous solution at infinite dilution [L/(gmol-s)] and T is the absolute temperature (K).

$$\log_{10}\left(\frac{k_{OH^-}}{k^{\infty}_{OH^-}}\right) = 0.221I - 0.016I^2$$

Where k_{OH^-} is the second order rate constant for the reaction of CO_2 with hydroxyl ion in aqueous solution [L/(gmol-s)]. I is the ionic strength calculated in Step 4.

Taken from Pohorecki and Moniuk [46].

Step 8: Calculate the Effective Area

$$K_{OG}a = \frac{a\sqrt{k_{OH^-} D_{CO_2} C_{OH^-}}}{H}$$

Where a is the effective packing surface area, k_{OH^-} is the rate constant obtained in Step 7, D_{CO_2} is the diffusivity of CO_2 from Step 6, H is the Henry's law coefficient from Step 5, and $K_{OG}a$ is the combined mass transfer coefficient/area term from Step 3.

C_{OH^-} is the concentration of hydroxyl ion remaining in solution after accounting for the amount consumed in the reaction.

APPENDIX B: SUPPLEMENTAL X-RAY CT IMAGING STUDIES

Several additional imaging experiments were carried out in order to fully take advantage of tomographic scanning resources. In select cases, test systems were constructed and supplied to scanning facilities. Due to scanning equipment downtime or other mitigating factors, both the 3DID and GE scanners were also used to conduct studies that deviated from the original scan plans. Random packing and catalytic distillation packing were both imaged with success. The results of these studies, although purely qualitative in this context, are presented here to illustrate the capabilities of X-ray CT imaging technology as applied to a variety of scenarios associated with packed column operation.

B.1 X-ray CT Scans of Random Packing

B.1.1 HYTEC, Inc.

Located in Los Alamos, New Mexico, HYTEC Incorporated designs, manufactures, and operates high-tech equipment for scientific measurement. The company operates as a spin-off from Los Alamos National Laboratory, with many of the employees serving as researchers at LANL. The company provided X-ray computed tomography scanning using a FlashCT scanner. A Comet 160 kV X-ray tube was used as a source. It was paired with Varian 2520 amorphous silicon flat panel detector. The system is housed in a small stand-alone chamber capable of imaging a part up to 16 inches in diameter. The number of views was 510. All data was acquired in a five-minute period. However, reconstruction took approximately 1.25 hours.

A test system was constructed to evaluate the FlashCT system for packed column imaging. A 6-inch acrylic column was fastened to a 1-inch thick acrylic square base. The column was approximately 8 inches tall. A smaller 1.5-inch diameter acrylic tube was fastened to the base, inside the 6-inch column. The small tube was located off-center. The 6-inch column was filled with 5/8-inch polypropylene ballast rings, except inside the small tube. The small tube was filled with water during the scans.

A report was delivered that contained a digital radiograph, sinogram, and CT slices of the object. The radiograph and sinogram showed features such as the column wall and water-filled inner tube with acceptable quality. The CT slices showed the packing, but not in great detail. The most interesting results from the HYTEC study were for three-dimensional rendering. A small portion of the column was rendered using 3-D opacity, 3-D isosurface, and 3-D volume renderings. The packing appeared jagged, particularly in the isosurface and volume renderings. Artifacts were also present in the data. Although the scan time was superior to previous X-ray studies, the poor resolution and source energy limited application of the FlashCT system to further studies.

B.1.2 3DID

Using the 3DID scanner described in Chapter 3, a test system containing a variety of random packings was studied. The goal of the exercise was to obtain quality 3-D data for random packing to potentially create a point-cloud file that could be imported into CFD software for meshing and simulation of flow. The test system consisted of a 6-inch diameter acrylic column approximately 3 feet tall. Four layers of random packing were installed in the column, with each layer having an approximate thickness of 8 inches. A series of CT slices were taken, with the slices later stacked in the Amira 3-D visualization

software. The spacing between slices was 0.15 mm, and the detector aperture was 0.3 mm.

Two sets of modeling data were obtained, each representing 3 inches of packed bed height. The first set of data for 5/8-inch metal ballast rings is shown in Figure B-1. The resolution of the images is not as good as the 3-D structured packing images from the GE scanner. The packing appears sharp, however, and surfaces are clean and continuous. Subtle bends in the internal structure of the packing are realized. A faint grid-like pattern can be observed in the images, particular in the top-down view. This is a result of the subpositions used during data acquisition. Since the data is taken out of order, variations in the surrounding environment and in the equipment itself will be amplified.

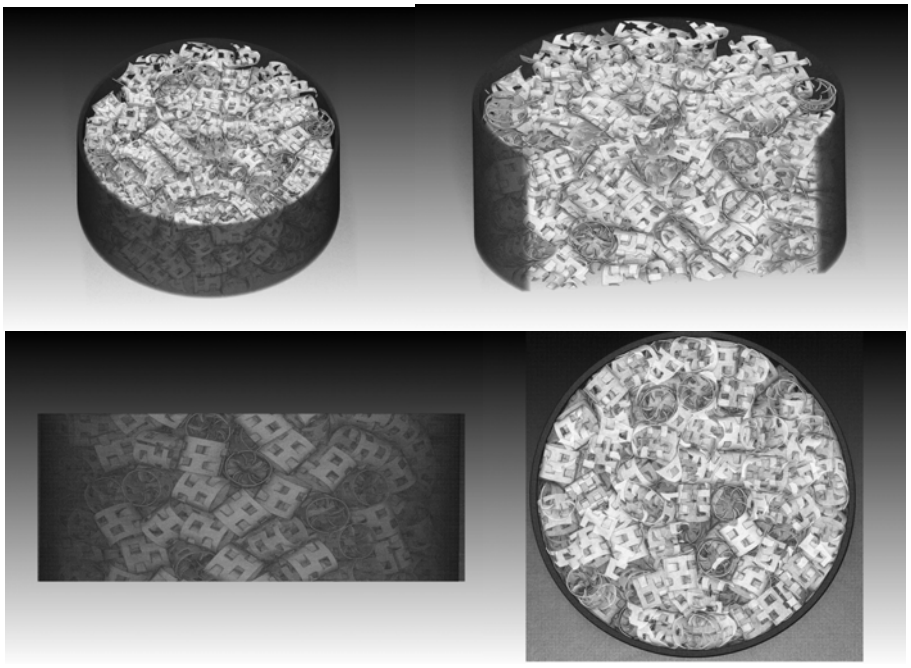

Figure B-1. 3-D reconstruction of 5/8-inch metal ballast rings using 3DID scanner.

A similar set of scans was performed for nominal 1.5-inch plastic Cascade mini rings. The volumetric reconstructions from stacked CT slices are shown in Figure B-2. The preference for the low-aspect ratio CMR to orient with the cylindrical axis vertical is observed, which is in contrast to the ballast rings, which primarily orient with the cylindrical axis aligned with the horizontal. The packing size contributes to increased void space near the column wall. The packing again appears sharp and clear. The grid-like pattern observed in reconstructions of the metal ballast ring images is not as pronounced for the plastic packing. This suggests that beam hardening could have contributed to the effect.

Figure B-2. 3-D reconstructions from CT slices of 1.5-inch plastic CMR using 3DID scanner.

B.1.3 CFAN

Responsible for producing composite materials for the aviation industry, CFAN is located in San Marcos, Texas. The company's primary deliverable is the wide-chord fan blade for the GE 90 aircraft engine used on the Boeing 777. As a joint venture between General Electric and SNECMA, CFAN is able to leverage the imaging expertise that GE possesses. High-quality tomographic imaging of the fan blades throughout the

manufacturing process is critical for quality control. Thus, CFAN has a GE Industrial X-ray CT scanner on site. The system is very similar to the scanner located at the Quality Technology Center in Cincinnati.

Due to the proximity of CFAN to Austin, a test scan was scheduled to explore the imaging capabilities of the GE ICT X-ray scanner and the applicability to imaging a packed column. The test system constructed for the HYTEC studies was sent to CFAN for imaging. The system was imaged dry, and with water added to the large column containing packing, rather than the smaller inner column as done at HYTEC. The source energy used was 6 MeV, and 1500 views were obtained. A test report was obtained that included CT slices and radiographs of the test object. Samples of the dry images are shown in Figure B-3.

Beam hardening effects are not visible in the images. The packing is resolved with great clarity. The contrast between air, metal, and plastic is good, thus the phases are easy to differentiate. The images obtained at CFAN showed great promise that a GE scanner could provide high quality images of a packed bed, and the decision was made to pursue GE as a scanning provider.

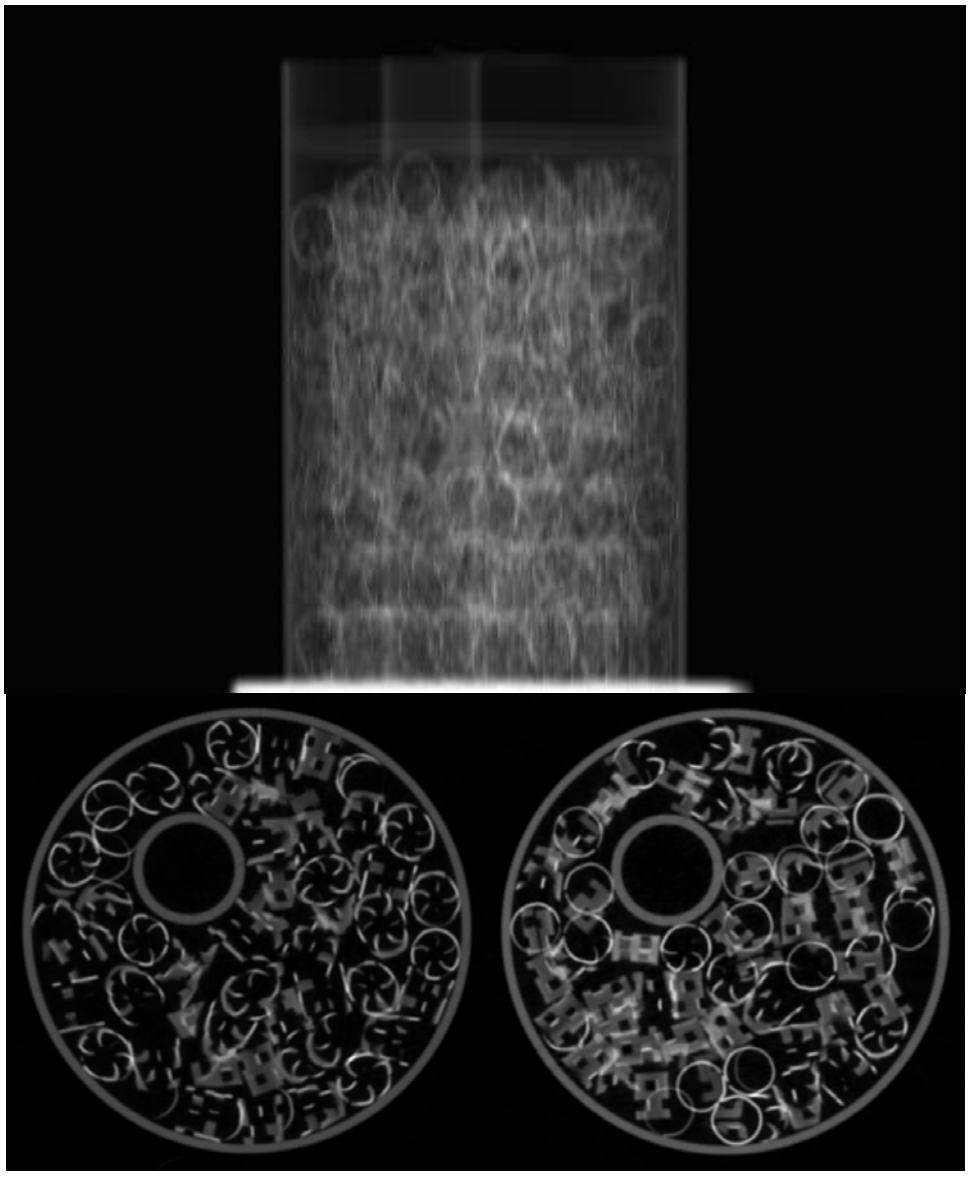

Figure B-3. Radiograph and CT slices of 5/8-inch metal ballast ring test system imaged at CFAN using GE-type scanner.

B.1.4 General Electric

During the experiments conducted using the Industrial CT scanner at GE's Quality Technology Facility, random packing was added to the top of the structured packing, below the liquid distributor. The 3-inch layer of 5/8-inch metal ballast rings

were installed to improve distribution to the top of the structured packing by breaking up the liquid jets exiting the four drip tubes of the distributor. Several CT slices were taken of the random packing under a variety of flow conditions as time allowed. Figure B-4 shows a sample dry CT image.

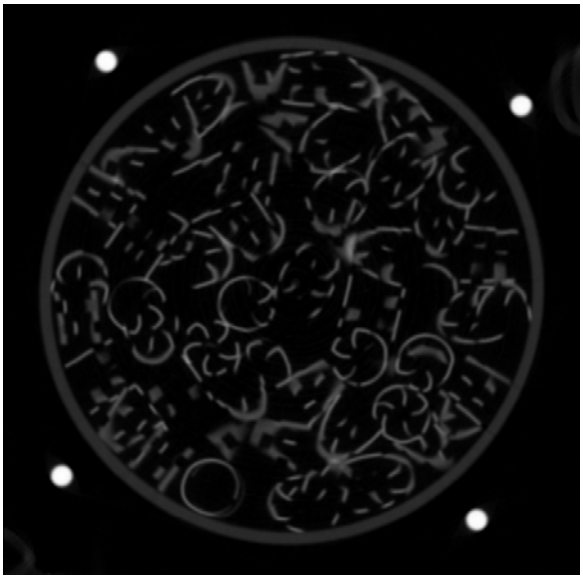

Figure B-4. Dry CT image of 5/8-inch metal ballast rings taken with GE scanner.

Only small portions of the packing pieces are visible due to the small slice thickness. The packing seems to fit well at the column wall, which was not true of the larger plastic CMR imaged with the 3DID scanner. Small beam hardening artifacts can be detected in the column wall.

When a flow image is considered, as in Figure B-5, subtle differences can be detected where the liquid is flowing through the packing. Since the liquid is not well distributed at this position in the column, large accumulations tend to be present near the

four drip points. Some of the packing in the bottom left corner of the image also appears to have shifted.

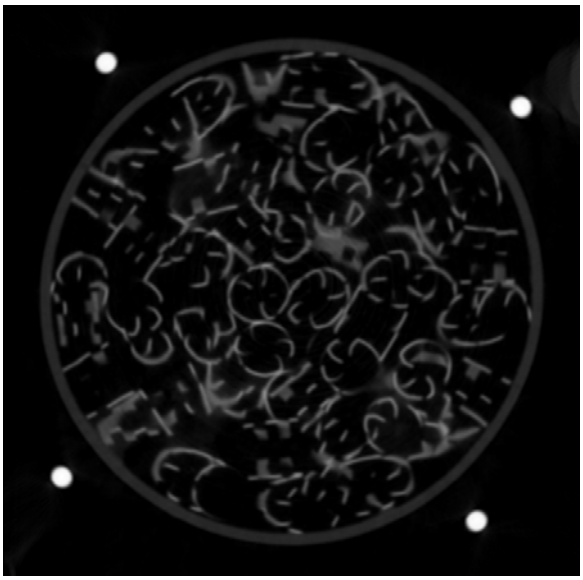

Figure B-5. Flow CT image of 5/8-inch metal ballast rings taken with GE scanner.

Several X-ray CT scanners were used to image various types of random packing. The GE scanner produced the best images. In the CFAN and GE CT images, beam hardening was minimal, contrast was high, and resolution was good. Further studies using X-ray CT to investigate random packing have a high chance of successfully identifying the local liquid location. However, additional studies of 3-D reconstructions should be undertaken to fully explore the capability of X-ray CT to resolve liquid films on random packing. Random packing is likely to shift between the dry and flow scans. It is important for the bed to be fully settled so that shifting will not affect subtraction techniques. However, applying a liquid load to settle the bed introduces liquid that can remain as static holdup in the dry slices, also affecting analysis by image subtraction.

B.2 X-ray CT Scans of Catalytic Distillation Packing

A commercially available catalytic distillation packing was imaged by X-ray computed tomography using the GE scanner. The scanner was operated in 6 MeV mode. Water and air were used as the liquid and vapor phase, respectively. The proprietary packing design employs catalyst beads mounted in a matrix. The packing was installed in the air-water column. One half-element of Mellapak 250Y structured packing was installed on top of the catalytic packing. A 3-inch layer of 5/8-inch metal ballast rings was installed on top of the Mellapak to improve the liquid distribution to the bed. Due to the confidentiality agreement in place with the vendor, no specifics can be provided on design, sizing, equipment setup, or flow rates. However, a general discussion of the features observed in several of the CT images will be presented. The X-ray CT technique showed remarkable sensitivity to the subtle physical changes of water adsorption on catalyst particles. It also provided clear visualization of the flow characteristics observed in catalytic distillation packing.

Similar to the procedure carried out for structured packing, a series of dry CT slices was first obtained for a portion of the packed section. Figure B-6 represents a cutaway view of a dry CT slice. Visible in the image are the spherical catalyst particles and the metal support structure. The black regions in the image represent air in the void spaces, both between structures and between the catalyst particles. It should be noted that some of the catalyst particles appear lighter than others. Subsequent images suggested that droplets of water may have fallen through those regions of the packing and wetted the catalyst.

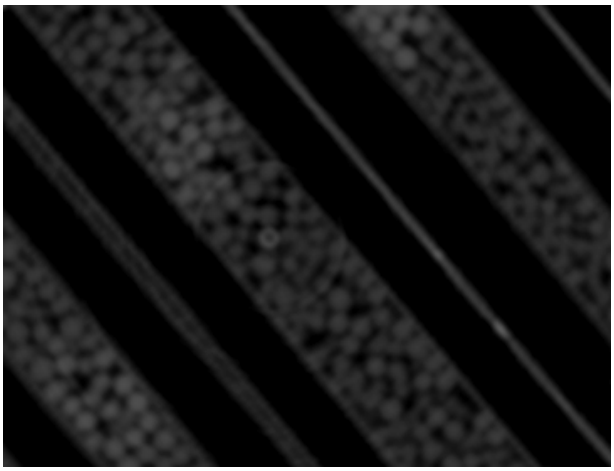

Figure B-6. Dry CT slice of catalytic distillation packing.

In order to provide a full set of imaging data for further analysis, CT images of the packing were obtained after the bed was completely wetted. Liquid and vapor flow was applied to the column for a period of time. The liquid flow was then stopped, and the packing was allowed to drain while vapor flow was maintained. The resulting images will be referred to as the static case. Figure B-7 shows an example of a static CT slice.

The static image verifies the partial wetting phenomenon that was proposed in the dry CT image. The majority of the catalyst particles appear brighter in the static image, indicating adsorption of liquid. This process changed the characteristic linear attenuation coefficient associated with the particles. The distribution of particle grayscales is more uniform, indicating the particles have roughly similar levels of hydration. Residual liquid can also be observed on portions of the metal structure. The void space between the particles and structure remained black.

By subtracting the dry slices from the static slices, the degree of water adsorption can be visualized. Figure B-8 represents a cutaway view of such an image. Areas that appear gray show the location of adsorbed water. Black regions did not differ between

the dry and static cases, indicating no adsorption. The bright white, crescent-shaped region in the upper portion of the image represents a large difference between the dry and static case, most likely the result of a catalyst particle shifting. To extract quantitative information using image subtraction, it is important to ensure that the bed contents do not move from one scan to another. Undrained water can also be observed in some locations.

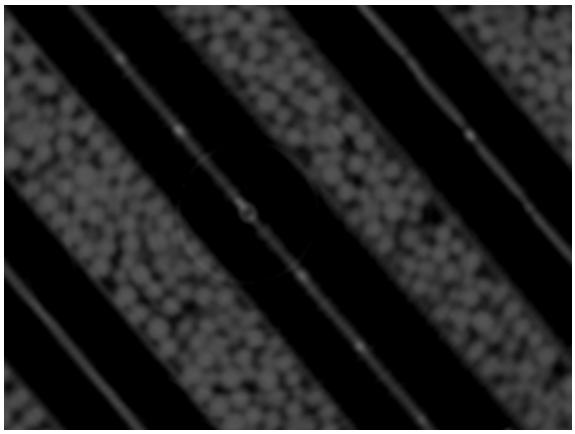

Figure B-7. Static CT slice of catalytic distillation packing.

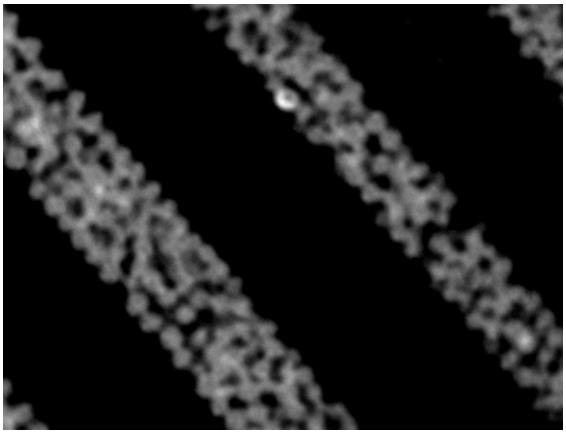

Figure B-8. Image representing the subtraction of a dry slice from a static slice.

The packing was also imaged while the column was operated over a variety of liquid and vapor flow rates. A sample of a CT image taken under flow conditions is shown in Figure B-9. The catalyst particles are still resolved although liquid is present in the majority of the void space between the particles, as evidenced by the larger grayscale value in those regions compared to the images with no flow. However, a few dark regions are still present around the particles, indicating an absence of liquid. Faint regions of water resembling rivulets are observable on the surface of the metal structure.

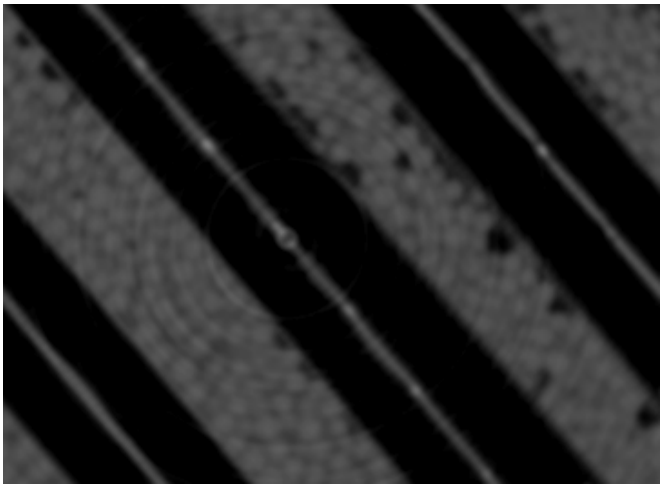

Figure B-9. CT image of catalytic distillation packing under flow.

Using the principles of image subtraction that were applied to structured packing in previous experiments, a representation of the location of liquid within the packing during operation can be obtained. Depending on the information that is desired, either a dry slice or a static slice is subtracted from a flow slice. Subtracting a dry slice will show all regions of water, including water adsorbed to the catalyst particles. If the subtraction is performed using a static slice in place of a dry slice, an image similar to Figure B-10 will be obtained. This image shows the location of liquid within the packing but not

within the particles, assuming they have been wetted to the same degree as in the static slice. The area usually occupied by particles appears black, indicating that all information cancelled out during the subtraction. This technique is valuable for determining the liquid flow path through the packing. Regions of water on the metal structure are also apparent.

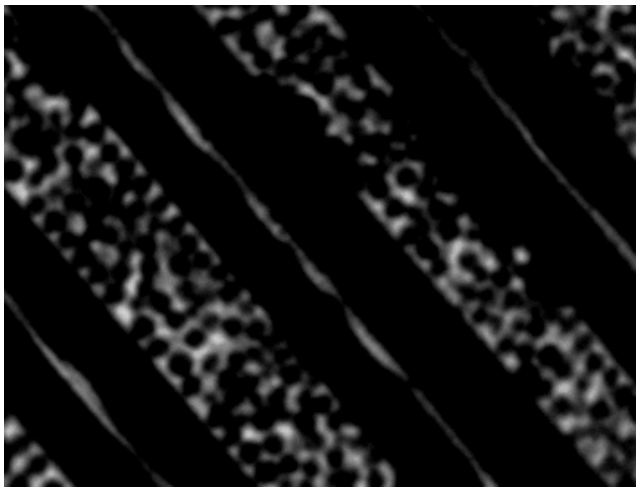

Figure B-10. CT image of catalytic distillation packing produced by subtracting a static slice from a flow slice.

Finally, by combining the subtracted flow image with the flow image in a multi-layer image, the location of liquid in the packing can be highlighted, as in Figure B-11. Regions of liquid are highlighted in blue. The largest accumulation of liquid appears as the brightest blue color, between the catalyst particles.

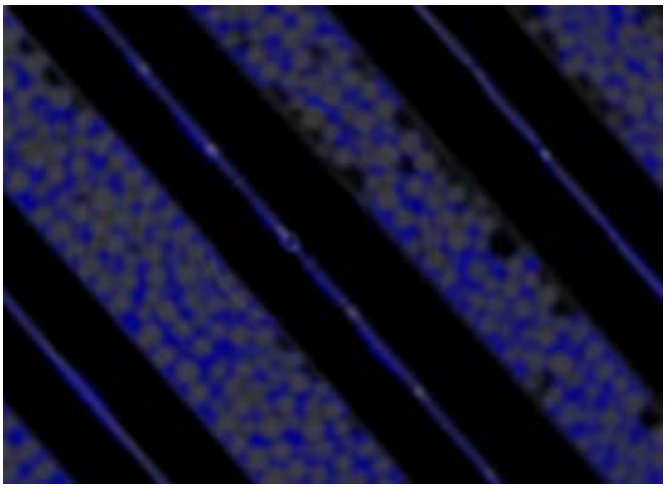

Figure B-11. Flow image of catalytic distillation packing with liquid regions highlighted in blue.

BIBLIOGRAPHY

[1] ASTM E1441-97: Standard Guide for Computed Tomography (CT) Imaging. American Society for Testing and Materials, 1997.

[2] Energy and Environmental Profile of the U.S. Petroleum Refining Industry. United States Department of Energy, Office of Industrial Technologies, 1998.

[3] Al-Dahhan, M.H., Kemoun, A., and Cartolano, A.R., Phase Distribution in an Upflow Monolith Reactor Using Computed Tomography. *AIChE Journal*, 2006, 52(2), 745-753.

[4] Ataki, A. and Bart, H.J., The Use of the VOF-Model to Study the Wetting of Solid Surfaces. *Chemical Engineering & Technology*, 2004, 27(10), 1109-1114.

[5] Banholzer, W.F., Spiro, C.L., Kosky, P.G., and Maylotte, D.H., Direct Imaging of Time-Averaged Flow Patterns in a Fluidized Reactor Using X-Ray Computed-Tomography. *Industrial & Engineering Chemistry Research*, 1987, 26(4), 763-767.

[6] Bartholomew, R.N. and Casagrande, R.M., Measuring Solids Concentration in Fluidized Systems by Gamma-Ray Absorption. *Industrial & Engineering Chemistry Research*, 1957, 49, 428-431.

[7] Billet, R. and Schultes, M., Prediction of Mass Transfer Columns With Dumped and Arranged Packings. *Chemical Engineering Research & Design*, 1999, 77, 498-504.

[8] Bowman, J.D., Use Column Scanning for Predictive Maintenance. *Chemical Engineering Progress*, 1991, 87(2), 25-31.

[9] Briley, J.K., *Evaluation of Predictive Models for Packed Column Effective Interfacial Area*. Senior Research Project (unpublished), The University of Texas at Austin, 2004.

[10] Cartmel, D.B., *Investigation of Local Scale Phenomena in Vapor Liquid Contactors Using X-ray Tomography*. M.S.E. Thesis, The University of Texas at Austin, 1999.

[11] Chaouki, J., Larachi, F., and Dudukovic, M.P., Noninvasive Tomographic and Velocimetric Monitoring of Multiphase Flows. *Industrial & Engineering Chemistry Research*, 1997, 36(11), 4476-4503.

[12] Chen, J.W., et al., Gas Holdup Distributions in Large-Diameter Bubble Columns Measured by Computed Tomography. *Flow Measurement and Instrumentation*, 1998, 9(2), 91-101.

[13] Crine, M., Marchot, P., and L'Homme, G., Statistical Hydrodynamics in Trickle Flow Columns. *AIChE Journal*, 1992, 38(1), 136-147.

[14] Deshusses, M.A., Cox, H.H.J., and Miller, D.W. The Use of CAT Scanning to Characterize Bioreactors for Waste Air Treatment. Presented at the Air & Waste Management Association's 91st Annual Meeting & Exhibition; San Diego, CA; 1998.

[15] Djebbar, Y. and Narbaitz, R.M., Neural Network Prediction of Air Stripping K_La. *Journal of Environmental Engineering*, 2002, 128, 451-460.

[16] Edwards, W.M., Section 14. Mass Transfer and Gas Absorption, in *Perry's Chemical Engineers' Handbook*, J.O. Maloney, Editor. 1984, McGraw-Hill Book Company: New York, 14-14.

[17] Fair, J.R., Seibert, A.F., Behrens, M., Saraber, P.P., and Olujic, Z., Structured Packing Performance - Experimental Evaluation of Two Predictive Models. *Industrial & Engineering Chemistry Research*, 2000, 39, 1788-1796.

[18] Grassler, T. and Wirth, K.E., X-ray Computer Tomography - Potential and Limitation for the Measurement of Local Solids Distribution in Circulating Fluidized Beds. *Chemical Engineering Journal*, 2000, 77(1-2), 65-72.

[19] Gu, F., Liu, C.J., Yuan, X.G., and Yu, G.C., CFD Simulation of Liquid Film Flow on Inclined Plates. *Chemical Engineering & Technology*, 2004, 27(10), 1099-1104.

[20] Herman, G.T., *Image Reconstruction from Projections: The Fundamentals of Computerized Tomography*. Academic Press: New York, 1980.

[21] Hines, A.L. and Maddox, R.N., *Mass Transfer: Fundamentals and Applications*. Prentice Hall, Inc.: Englewood Cliffs, New Jersey, 1985.

[22] Hubers, J.L., Striegel, A.C., Heindel, T.J., Gray, J.N., and Jensen, T.C., X-ray Computed Tomography in Large Bubble Columns. *Chemical Engineering Science*, 2005, 60(22), 6124-6133.

[23] Humphrey, J.L. and Keller, G.E., *Separation Process Technology*. McGraw-Hill: New York, 1997.

[24] Iliuta, I., Petre, C.F., and Larachi, F., Hydrodynamic Continuum Model for Two-Phase Flow Structured-Packing-Containing Columns. *Chemical Engineering Science*, 2004, 59(4), 879-888.

[25] Jain, A.K., *Fundamentals of Digital Image Processing*. Prentice Hall, Inc.: Englewood Cliffs, New Jersey, 1989.

[26] Kai, T., et al., Application of Fast X-ray CT Scanner to Visualization of Bubbles in Fluidized Bed. *Journal of Chemical Engineering of Japan*, 2000, 33(6), 906-909.

[27] Kai, T., Misawa, M., Takahashi, T., Tiseanu, I., and Ichikawa, N., Observation of 3-D Structure of Bubbles in a Fluidized Catalyst Bed. *Canadian Journal of Chemical Engineering*, 2005, 83(1), 113-118.

[28] Kantzas, A., Computation of Holdups in Fluidized and Trickle Beds by Computer-Assisted Tomography. *AIChE Journal*, 1994, 40(7), 1254-1261.

[29] Kantzas, A. and Kalogerakis, N., Monitoring the Fluidization Characteristics of Polyolefin Resins Using X-ray Computer Assisted Tomography Scanning. *Chemical Engineering Science*, 1996, 51(10), 1979-1990.

[30] Kantzas, A., Wright, I., and Kalogerakis, N., Quantification of Channeling in Polyethylene Resin Fluid Beds Using X-ray Computer Assisted Tomography (CAT). *Chemical Engineering Science*, 1997, 52(13), 2023-2035.

[31] Kemoun, A., Ong, B.C., Gupta, P., Al-Dahhan, M.H., and Dudukovic, M.P., Gas Holdup in Bubble Columns at Elevated Pressure via Computed Tomography. *International Journal of Multiphase Flow*, 2001, 27(5), 929-946.

[32] Kumar, S.B., Moslemian, D., and Dudukovic, M.P., A Gamma-Ray Tomographic Scanner for Imaging Voidage Distribution in 2-Phase Flow Systems. *Flow Measurement and Instrumentation*, 1995, 6(1), 61-73.

[33] Kumar, S.B. and Dudukovic, M.P., Computer Assisted Gamma and X-Ray Tomography: Applications to Multiphase Flow Systems, in *Non-Invasive*

Monitoring of Multiphase Flows, J. Chaouki, F. Larachi, and M.P. Dudukovic, Editors. 1997, Elsevier: Amsterdam, The Netherlands, 47-104.

[34] Kumar, S.B., Moslemian, D., and Dudukovic, M.P., Gas-Holdup Measurements in Bubble Columns Using Computed Tomography. *AIChE Journal*, 1997, 43(6), 1414-1425.

[35] Leahy, R.M. and Clackdoyle, R., Computed Tomography, in *Handbook of Image & Video Processing*, A. Bovik, Editor. 2000, Academic Press: San Diego, CA, 771-787.

[36] Lockett, M.J., Easily Predict Structured-Packing HETP. *Chemical Engineering Progress*, 1998, 94, 60-66.

[37] Lutran, P.G., Ng, K.M., and Delikat, E.P., Liquid Distribution in Trickle Beds. An Experiment Using Computer-Assisted Tomography. *Industrial & Engineering Chemistry Research*, 1991, 30, 1270-1280.

[38] Marchot, P., Toye, D., Crine, M., Pelsser, A.M., and L'Homme, G., Investigation of Liquid Maldistribution in Packed Columns by X-ray Tomography. *Chemical Engineering Research & Design*, 1999, 77(A6), 511-518.

[39] Marchot, P., Crine, M., L'Homme, G., and Toye, D., 3-D Imaging of Dynamic Retention in a Structured Bed by X-ray Tomography. *Recents Progres en Genie des Procedes*, 2001, 15(78), 75-81.

[40] Marchot, P., et al., Liquid Distribution Images on Structured Packing by X-ray Computed Tomography. *AIChE Journal*, 2001, 47(6), 1471-1476.

[41] National Research Council Panel on Separation Technology for Industrial Reuse and Recycling, *Separation Technologies for the Industries of the Future*. National Academy Press: Washington, D.C., 1998.

[42] Olujic, Z., Development of a Complete Simulation Model for Predicting the Hydraulic and Separation Performance of Distillation Columns Equipped with Structured Packings. *Chemical & Biochemical Engineering Quarterly*, 1997, 11, 31-46.

[43] Olujic, Z., Crine, M., Toye, D., and Marchot, P. X-Ray Computed Tomography: A Key to Revealing the Secrets of Small Scale Liquid Maldistribution in Packed Beds. Presented at the American Institute of Chemical Engineers Spring National Meeting; Houston, TX; 2001.

[44] Onda, K., Takeuchi, H., and Okumoto, Y., Mass Transfer Coefficients Between Gas and Liquid Phases in Packed Columns. *Journal of Chemical Engineering of Japan*, 1967, 1, 56-62.

[45] Pilling, M. Sulzer Chemtech, Personal Communication, August 2003.

[46] Pohorecki, R. and Moniuk, W., Kinetics of Reaction Between Carbon Dioxide and Hydroxyl Ions in Aqueous Electrolyte Solutions. *Chemical Engineering Science*, 1988, 43(7), 1677-1684.

[47] Pollock, G.S. and Eldridge, R.B., Neural Network Modeling of Structured Packing Height Equivalent to a Theoretical Plate. *Industrial & Engineering Chemistry Research*, 2000, 39, 1520-1525.

[48] Reinecke, N., Petritsch, G., Schmitz, D., and Mewes, D., Tomographic Measurement Techniques - Visualization of Multiphase Flows. *Chemical Engineering & Technology*, 1998, 21(1), 7-18.

[49] Rocha, J.A., Bravo, J.L., and Fair, J.R., Distillation Columns Containing Structured Packings: A Comprehensive Model for Their Performance. 1. Hydraulic Models. *Industrial & Engineering Chemistry Research*, 1993, 32(4), 641-651.

[50] Rocha, J.A., Bravo, J.L., and Fair, J.R., Distillation Columns Containing Structured Packings: A Comprehensive Model for Their Performance. 2. Mass-Transfer Model. *Industrial & Engineering Chemistry Research*, 1996, 35(5), 1660-1667.

[51] Rosenfeld, A. and Kak, A.C., *Digital Picture Processing*. Academic Press: San Diego, CA, 1982.

[52] Roy, S., Chen, J.W., Kumar, S.B., Al-Dahhan, M.H., and Dudukovic, M.P., Tomographic and Particle Tracking Studies in a Liquid-Solid Riser. *Industrial & Engineering Chemistry Research*, 1997, 36(11), 4666-4669.

[53] Roy, S., et al., Countercurrent Flow Distribution in Structured Packing via Computed Tomography. *Chemical Engineering and Processing*, 2005, 44(1), 59-69.

[54] Roy, S., Kemoun, A., Al-Dahhan, M.H., and Dudukovic, M.P., Experimental Investigation of the Hydrodynamics in a Liquid-Solid Riser. *AIChE Journal*, 2005, 51(3), 802-835.

[55] Schmit, C.E., Cartmel, D., and Eldridge, R.B., Process Tomography: An Option for the Enhancement of Packed Vapor-Liquid Contactor Model Development. *Industrial & Engineering Chemistry Research*, 2000, 39, 1546-1553.

[56] Schmit, C.E., *Evaluation of X-ray Imaging to Investigate Hydraulic Performance of Vapor-Liquid Contactors*. Ph.D. Thesis, The University of Texas at Austin, 2001.

[57] Schmit, C.E., Cartmel, D.B., and Eldridge, R.B., The Experimental Application of X-ray Tomography to a Vapor-Liquid Contactor. *Chemical Engineering Science*, 2001, 56, 3431-3441.

[58] Schmit, C.E. and Eldridge, R.B., Investigation of X-ray Imaging of Vapor-liquid Contactors. 1. Studies Involving Stationary Objects and a Simple Flow System. *Chemical Engineering Science*, 2004, 59(6), 1255-1266.

[59] Schmit, C.E., Perkins, J., and Eldridge, R.B., Investigation of X-ray Imaging of Vapor-liquid Contactors. 2. Experiments and Simulations of Flows in an Air-water Contactor. *Chemical Engineering Science*, 2004, 59(6), 1267-1283.

[60] Schmitz, D., Reinecke, N., Petritsch, G., and Mewes, D. High Resolution X-ray Tomography for Stationary Multiphase Flows. Presented at the OECD/CSNI Specialist Meeting on Advanced Instrumentation and Measurement Technologies; Santa Barbara, CA; 1997.

[61] Schmitz, D., Reinecke, N., Petritsch, G., and Mewes, D. X-Ray Computed Tomography for Stationary Multiphase Flow in Random and Structured Packings. Presented at Frontiers in Industrial Process Tomography II; Delft, The Netherlands; 1997.

[62] Schmitz, D., Petritsch, G., Mewes, D., and Moser, F. Tomographic Measurement of the Liquid Hold-up in a Structured Packing. Presented at ASME Heat Transfer Division meeting; 371-378; 1998.

[63] Seader, J.D. and Henley, E.J., *Separation Process Principles*. John Wiley & Sons, Inc.: New York, 1998.

[64] Seibert, A.F., Wilson, I., Lewis, C., and Rochelle, G. Effective Gas/Liquid Contact Area of Packing for CO2 Absorption/Stripping. Presented at the 7th International Conference on Greenhouse Gas Control Technologies; 1925-1928; Vancouver, Canada; 2004.

[65] Severance, W.A.N., Distillation - Advances in Radiation Scanning of Distillation-Columns. *Chemical Engineering Progress*, 1981, 77(9), 38-41.

[66] Severance, W.A.N., Differential Radiation Scanning Improves the Visibility of Liquid Distribution. *Chemical Engineering Progress*, 1985, 81(4), 48-51.

[67] Sherwood, T.K., Pigford, R.L., and Wilke, C.R., *Mass Transfer*. McGraw-Hill: New York, 1975.

[68] Shi, M.G. and Mersmann, A., Effective Interfacial Area in Packed Columns. *German Chemical Engineering*, 1985, 8, 87-96.

[69] Spiegel, L. and Meier, W., Distillation Columns with Structured Packings in the Next Decade. *Chemical Engineering Research & Design*, 2003, 81(A1), 39-47.

[70] Stichlmair, J., Bravo, J.L., and Fair, J.R., General Model for Prediction of Pressure Drop and Capacity of Countercurrent Gas/Liquid Packed Columns. *Gas Separation & Purification*, 1989, 3, 19-28.

[71] Suess, P. and Spiegel, L., Hold-up of Mellapak Structured Packings. *Chemical Engineering and Processing*, 1992, 31(2), 119-124.

[72] Szulczewska, B., Zbicinski, I., and Gorak, A., Liquid Flow on Structured Packing: CFD Simulation and Experimental Study. *Chemical Engineering & Technology*, 2003, 26(5), 580-584.

[73] Toye, D., Marchot, P., Crine, M., and L'Homme, G., The Use of Large Scale Computer Assisted Tomography for the Study of Hydrodynamics in Trickling Filters. *Chemical Engineering Science*, 1994, 49(24B), 5271-5280.

[74] Toye, D., Marchot, P., Crine, M., and L'Homme, G., Modeling of Multiphase Flow in Packed Beds by Computer-assisted X-ray Tomography. *Measurement Science & Technology*, 1996, 7(3), 436-443.

[75] Toye, D., Crine, M., Marchot, P., and L'Homme, G. Modeling of the Liquid Distribution in a Packed Column Based Upon X-Ray Tomography Images. Presented at Frontiers in Industrial Process Tomography II; 337-342; Delft, The Netherlands; 1997.

[76] Toye, D., Marchot, P., Crine, M., Pelsser, A.M., and L'Homme, G., Local Measurements of Void Fraction and Liquid Holdup in Packed Columns Using X-ray Computed Tomography. *Chemical Engineering and Processing*, 1998, 37(6), 511-520.

[77] Toye, D., Crine, M., and Marchot, P., Imaging of Liquid Distribution in Reactive Distillation Packings with a new High-energy X-ray Tomograph. *Measurement Science & Technology*, 2005, 16(11), 2213-2220.

[78] Wagner, I., Stichlmair, J., and Fair, J.R., Mass Transfer in Beds of Modern, High-Efficiency Random Packings. *Industrial & Engineering Chemistry Research*, 1997, 36, 227-237.

[79] Wang, G.Q., Yuan, X.G., and Yu, K.T., Review of Mass-Transfer Correlations for Packed Columns. *Industrial & Engineering Chemistry Research*, 2005, 44, 8715-8729.

[80] Wang, Z.C., Afacan, A., Nandakumar, K., and Chuang, K.T., Porosity Distribution in Random Packed Columns by Gamma Ray Tomography. *Chemical Engineering and Processing*, 2001, 40(3), 209-219.

[81] Whaley, A.K., Bode, C.A., Ghosh, J., and Eldridge, R.B., HETP and Pressure Drop Prediction for Structured Packing Distillation Columns Using a Neural Network Model. *Industrial & Engineering Chemistry Research*, 1999, 38, 1736-1739.

[82] Xu, S.X. and Kennedy, G. Gamma-Ray Computer-Aided Tomography of Industrial Packed Columns. Presented at the American Institute of Chemical Engineers Spring National Meeting; Houston, TX; 1999.

[83] Xu, S.X. and Pless, L. Scan/Simulation Integrated Diagnostics For Distillation Improvement. Presented at the American Institute of Chemical Engineers Spring National Meeting; Atlanta, GA; 2005.

[84] Yin, F.H., Sun, C.G., Afacan, A., Nandakumar, K., and Chuang, K.T., CFD Modeling of Mass-Transfer Processes in Randomly Packed Distillation Columns. *Industrial & Engineering Chemistry Research*, 2000, 39(5), 1369-1380.

[85] Yin, F.H., Afacan, A., Nandakumar, K., and Chuang, K.T., Liquid Holdup Distribution in Packed Columns: Gamma Ray Tomography and CFD Simulation. *Chemical Engineering and Processing*, 2002, 41(5), 473-483.

[86] Zarabi, T. and Kantzas, A., Predictions on Bubble and Solids Movement in Laboratory Polyethylene Fluid Beds as Visualized by X-ray Computer Assisted Tomography (CAT) Scanning. *Canadian Journal of Chemical Engineering*, 1998, 76(5), 853-865.

VITA

Christian Wayne Green was born on December 22, 1979 in Washington, DC, the first of two sons born to Carl W. and Joanne M. Green. He graduated from Pinecrest High School in Southern Pines, North Carolina in May 1997. Christian attended North Carolina State University in Raleigh, North Carolina from 1997 – 2001. He was awarded a Bachelor of Science degree in Chemical Engineering and graduated Magna Cum Laude in May 2001. In the summer of 2001, Christian held an internship at the Naval Research Laboratory in Washington, DC prior to entering the Graduate School of The University of Texas at Austin in August of that year. During the summer of 2002, Christian worked for The Dow Chemical Company's Process Separations group in Freeport, Texas. Upon graduation, he plans to begin work with ConocoPhillips in Bartlesville, Oklahoma.

Permanent Address: 115 Ridgewood Road, Pinehurst, NC 28374

This dissertation was typed by the author.